Aus der Klinik für Strahlentherapie und Radioonkologie
der Medizinischen Fakultät Mannheim
(Direktor: Prof. Dr. med. Frederik Wenz)

TOWARDS CLINICAL IMPLEMENTATION OF ULTRAFAST COMBINED KV-MV CONE-BEAM CT FOR IGRT OF LUNG TUMORS WITHIN BREATH-HOLD: EVALUATION OF DOSIMETRY AND REGISTRATION ACCURACY BASED ON PHANTOM STUDIES

Inauguraldissertation zur Erlangung des
Doctor scientiarum humanarum
(Dr. sc. hum.)

der Medizinischen Fakultät Mannheim

der Ruprecht-Karls-Universität

zu

Heidelberg

vorgelegt von

Anna Maria Arns

aus

Siegen

2016

Dekan: Prof. Dr. med. Sergij Goerdt

Referent: Prof. Dr. med. Frederik Wenz

Summary

Combined ultrafast 90°+90° kV-MV cone-beam computed tomography (CBCT) within breath-hold of 15s is a promising approach to accelerate imaging for patients with lung tumors treated with deep inspiration breath-hold (DIBH). To judge clinical feasibility of kV-MV CBCT, two main properties have to be fulfilled: (1) image quality has to be sufficient for registration within 1 mm accuracy, and (2) dose exposure has to be small compared to the prescribed dose.
The aim of this thesis was to develop concepts to test these properties of kV-MV CBCT based on a comparison study to clinically established CBCT methods. In particular, the main aspects were accomplished as follows:
Dosimetric properties: For a reliable measurement of the absorbed dose in the imaging process, accurate dose calibration was performed for kV and MV energy. Extensive research was done to determine beam quality for both energy ranges. For direct comparison of MV and kV dose output, the relative biological effectiveness was considered. To simulate the patient situation, measurements in various representative locations of an inhomogeneous thorax phantom were performed. Furthermore, the CT dose index (CTDI) was determined for future quality assurance purposes. A measured dose of 20.5 mGE in the target region was comparable to the widely-used clinical imaging technique, whereas kV-MV spared healthy tissue and reduced dose to 6.6 mGE (30%). These results show that from the dosimetric point of view, kV-MV CBCT is suitable for hypofractionated DIBH.
Registration accuracy: A detailed phantom registration study was performed with different tumor-mimicking tumor-shapes in an inhomogeneous thorax phantom. 10 random pre-selected isocenter shifts were applied using optical tracking with high accuracy of 0.05 mm. Registration was performed with three methods: (1) manual, (2) automatic software provided by manufacturer, and (3) self-developed automatic registration framework. An objective evaluation was achieved with the self-developed registration method by automatic determination of identical region of interest around the tumor-shapes for all imaging techniques. Registration accuracy was in average maintained below 1 mm, with maximum outliers still below 1.5 mm.
In summary, the comparison studies conceptualized and accomplished in this thesis demonstrated that kV-MV CBCT is feasible for imminent clinical implementation.

Preamble

Ultrafast combined kilovoltage-megavoltage cone-beam CT (kV-MV CBCT) was developed in our institution by a small research group. The proof-of-principle was published by Blessing et al. [18]. My contribution as a co-author was the stabilization of automated stripe-artifact detection, based on a part of my Diploma thesis [9]. The first steps towards synchronized kV-MV CBCT were published by Wertz et al. [99]. The final automated implementation was accomplished as part of the PhD thesis of a colleague within our research group [16]. An end-to-end test of fully automated kV-MV CBCT was presented orally on ESTRO annual meeting [15], a publication about the final automated workflow was recently submitted to a peer-reviewed journal [17]. In both conference abstract and publication, my contribution as second author was to engage in optimization of linac parameters for stable MV dose output achievement.

Presentations of interim results of this thesis were given on several conferences. The interim dosimetrical and geometrical aspects of novel kV-MV CBCT (section 2.3) on an inhomogeneous thorax phantom were presented as a poster at the ASTRO annual meeting [5] and as an oral presentation at the DGMP annual meeting [8], including measurements of CT dose index. A poster about interim registration accuracy results was presented at ASTRO annual meeting [6]. The dosimetry and registration accuracy measurements were further improved, measurement calibration and performance accuracy was refined, and evaluation methods were developed and executed. The study on registration accuracy (section 2.5) was recently accepted for publication[1] [7]; the study of kV-MV CBCT dosimetry (section 2.3) will soon be submitted for publication. The contents (some wording, figures, tables) of the study on registration accuracy in this thesis are adopted from the submitted article [7].

[1]The final publication is available at Springer via http://dx.doi.org/ [10.1007/s00066-016-0947-2].

Contents

List of Figures

List of Tables

Glossary

3D-CRT	Three-dimensional conformal radiotherapy
4D-CBCT	Four-dimensional cone-beam Computed Tomography, sorting the projections by breathing signal
AAPM	American Association of Physicists in Medicine
ab	Alignment box
ADCL	Accredited Dosimetry Calibration Laboratory
AP	Anterior-posterior direction
CBCT	Cone-beam Computed Tomography
CC	Cranio-caudal direction
CT	Computed Tomography
CTDI	Computed Tomography dose index
CUDA	Compute Unified Device Architecture, enables a program to run on a graphics processing unit (program acceleration)
DIBH	Deep-inspiration breath-hold
DIBH-FFF-SABR	Deep-inspiration breath-hold flattening-filter-free stereotactic ablative radiotherapy
EBRT	External beam radiotherapy
FBP, FDK	Filtered Backprojection, Feldkamp-Davis-Kress algorithm (reconstruction technique for CT, CBCT)
FFF	Flattening-filter-free
FOV	Field-of-view
GE	Gray-equivalent, considering the relative biological effectiveness in absolute dose specification
GPU	Graphics Processing Unit

Gy	Gray
HI	Homogeneity index
HVL	Half-value-layer
IAEA	International Atomic Energy Agency
ICRP	International Commission of Radiological Protection
ICRU	International Commission on Radiation Units and Measurements
IGRT, IG	Image-guided radiotherapy
ImageJ	Image processing program
IMRT	Intensity-modulated radiotherapy
Isocenter	Center of rotation for gantry, couch, collimator
ITV	Internal target volume
iViewGT	Megavoltage imaging system from Elekta, AB
KERMA	Kinetic energy released per unit mass
kV	Kilovoltage
kV_{180} CBCT	Cone-beam Computed Tomography preset defined with 100 kV beam energy and 180° gantry rotation
kV-$Chest_1$ CBCT	Clinical cone-beam Computed Tomography preset, available in kilovoltage imaging system XVI v4.2.2 from Elekta AB
kV-$Chest_2$ CBCT	Clinical cone-beam Computed Tomography preset, available in kilovoltage imaging system XVI v5.0.2 from Elekta AB
kV-MV CBCT	Kilovoltage-megavoltage cone-beam Computed Tomography
kVp	Kilovoltage-peak energy
LET	Linear energy transfer
Linac	Linear accelerator
$LINAC_1$	Definition of clinically commissioned Elekta Synergy linear accelerator, equipped with a foldout MV detector (iViewGT v3.4) and perpendicularly mounted kV-CBCT (XVI v4.2.2)
$LINAC_2$	Definition of clinically commissioned Elekta VersaHD linear accelerator, equipped with a foldout MV detector (iViewGT v3.4) and perpendicularly mounted kV-CBCT (XVI v5.0.2)

mA	Milli-Ampere (tube current unit)
mAs	Milli-Ampere-second (tube current time product unit)
Matlab	Matrix laboratory (numerical computing software)
MLC	Multi-leaf-collimator
MLS-ART	Multi-level scheme algebraic reconstruction technique
MRI	Magnetic Resonance Imaging
MU	Monitor Unit
MV	Megavoltage
MV_{180} CBCT	Cone-beam Computed Tomography preset defined with 6 MV beam energy and 180° gantry rotation
NSCLC	Non-small cell lung cancer
NTCP	Normal tissue complication propability
OAR	Organs at risk
OBI	On-board Imager (kilovoltage imaging system from Varian Medical Systems)
pCT	planning Computed Tomography
PDD	Percent depth dose distribution
PET/CT	Positron Emission Tomography combined with Computed Tomography
PTV	Planning target volume
QA	Quality assurance
QVL	Quarter-value-layer
RBE	Relative biological effectiveness
RL	Right-left direction
rpm	Rounds per minute
RT	Radiotherapy
SABR	Stereotactic ablative radiotherapy
SSD	Source to surface distance
TCP	Tumor control probability
TPS	Treatment planning system
VMAT	Volumetric modulated arc therapy
XVI	X-ray volume imaging (kilovoltage imaging system from Elekta AB)

1 Introduction

Lung cancer remains the leading cancer-induced cause of death worldwide for both male and female [41, 90]. In 2015, the estimated lung cancer morbidity rate was 13% of all cancer diagnoses (N $\approx$ 1.8 million), resulting in lung cancer being the second most likely new cancer site. Every third cancer-induced death is caused by lung cancer. Non-small cell lung cancer (NSCLC) covers 80% of the new annual lung cancer diagnoses, and 20% of these have early-stage disease and thus the best chance for cancer cure [90]. If applicable, lung cancer treatment is carried out by surgery. In case the tumor is inoperable or other reasons eliminate a surgical procedure, radiotherapy (RT) is an appropriate alternative. Mortality rates however remain very high with conventional fractionated external beam radiotherapy (EBRT) [27].

With the advent of image-guided intensity-modulated radiotherapy (ig-IMRT) and further breakthroughs in RT technology, the over the last decades clinically well-established stereotactic ablative radiotherapy (SABR) of brain metastases was expanded to extracranial tumor lesions, such as lung metastases or NSCLC [23, 43, 96]. Indispensable advances in RT technology for extracranial hypofractionated SABR were:

- *Tumor definition:* broad selection of diagnostic imaging techniques, such as computed tomography (CT), magnetic resonance imaging (MRI) and positron emission tomography (PET/CT)
- *Radiotherapy treatment planning:* IMRT with dynamic multi-leaf collimator (MLC) from different gantry angles or volumetric modulated arc therapy (VMAT), determined by high-quality calculation algorithms, leading to steep dose gradients between tumor and healthy tissue (e.g. inverse planning based on Monte Carlo algorithms [11])

- *Image guidance:* reproducible patient positioning with accurate motion management during imaging and treatment plan delivery
- *Treatment delivery:* precise maintenance and quality assurance (QA) of linear accelerator (linac) and imaging system

Besides being time-efficient and technologically on the highest level, SABR achieves excellent radiobiological outcomes: tremendous local tumor control probability (TCP) and substantially lower normal tissue complication probability (NTCP), leading to an increased therapeutic window [43, 96]. Hypofractionated high-dose ig-SABR (image-guided SABR) treatment outcomes are more promising than normofractionated 3D-conformal RT (3D-CRT) and show good results with less toxicity to normal tissue (less pneumonitis of lung) while applying ablative doses to the tumor [27, 29].

Recently, SABR treatment times were reduced significantly to the technically fastest limits at present by introducing the flattening-filter-free (FFF) irradiation technique, which can reach high dose-rates. Thus, treatment times changed over time from $60-90\,\text{min}$ for the initial SABR-technique with stereotactic body fixation [43], to $20-30\,\text{min}$ with ig-IMRT [13, 25] and finally $3-5\,\text{min}$ beam-on times with FFF for fractional doses of $5-20\,\text{Gy}$ [22, 25, 42, 82, 92].

Essential pre-requisite for successful high-dose lung SABR is appropriate and reliable image guidance (IG) as well as meticulous breathing-induced motion management. The most common IG technique used in clinical routine for pre-treatment target localizations is a kilovoltage (kV) CBCT perpendicularly mounted to the linac [24, 60]. In rare cases Megavoltage cone-beam CT (MV-CBCT) [79, 85] is applied instead, however, MV-CBCT is not popular due to reduced soft-tissue contrast.

Seppenwoolde et al. [88] described in detail the remarkable respiratory motion trajectories of lung tumors. The largest motion amplitude of in average $(12\pm2)\,\text{mm}$ was observed in craniocaudal (CC) direction for tumors in the lower lobe, not attached to any rigid structures. Motion in right-left (RL) and anterioposterior (AP) directions were smaller with in average $(2\pm1)\,\text{mm}$. Breathing patterns differed from patient to patient, and also inter- and intrafractionally for one patient considering magnitude and breathing period [29, 61, 88, 91].

For compensation of breathing motion in lung SABR, the AAPM TG report 76 [61] summarizes a variety of methods for motion management. The most prominent ones

are gating [46, 76], tracking [30, 93], formation of an internal target volume (ITV) based on a 4D CBCT [47, 70, 95] or breath-hold strategies such as deep inspiration breath-hold (DIBH) [13, 23, 67, 77, 102].

Gating and real-time tracking methods adjust the treatment beam delivery to the breathing cycle of the patient, either by only delivering dose when the tumor is in the gated window [46, 76], or by following the tumor with a robotic arm (e.g. CyberKnife) [30, 93]. Both methods increase treatment times as well as imaging dose exposure due to constant tracking of the tumor. The motion of organs at risk (OAR) however is not considered. The application is complicated and needs extensive individual modelling to consider tumor deformation and potential tracking delay.

The 4D treatment based on the ITV concept not only increases imaging and treatment time, but also enlarges the planning target volume (PTV). The ITV covers the whole breathing cycle from end-exhale to end-inhale phase, resulting in a large target volume and thus more irradiation of surrounding healthy tissue [47, 70, 95]. The ICRU report 62 provides further details on target definitions and margins [1]. The large amount of data and the complex workflow may limit the clinical usage.

Breath-hold strategies and especially DIBH have several dosimetric and methodical advantages. Breath-hold gating simplifies RT performance most by tumor immobilization and smallest PTV. The static tumor position is highly reproducible [67] and thus treatment planning and delivery need no further data evaluation and motion considerations. The tumor being a conformal "fixed target" facilitates treatment planning and improves sparing of OAR [22, 74]. Especially for the case of deep inspiration breath-hold (DIBH), both cardiac and lung toxicity can be reduced because the diaphragm pulls the heart away from the breast, and the lung (as one of the most radiation-sensitive organs) is enlarged to $70-80\%$ vital capacity, leading to only a small part of the lung being within beams-eye view [61]. Since no further imaging during treatment is required, imaging dose is smallest for DIBH strategy.

In our institution (University Medical Center Mannheim, UMM, Mannheim, Germany), hypofractionated ig-SABR is usually combined with computer-assisted breath-hold gating (DIBH). Conservative hypofractionation of $5 \times 12\,\mathrm{Gy}$ (peripheral) or $12 \times 5\,\mathrm{Gy}$ (central) applied dose to the tumor is usually applied to small lung lesions of diameters $< 5\,\mathrm{cm}$. Narrow residual PTV margins of $5\,\mathrm{mm}$ in radial, and $10\,\mathrm{mm}$ in longitudinal direction are common. Inverse treatment planning and dose calculation

based on Monte Carlo algorithms can achieve steep dose gradients between lung lesions and surrounding organs at risk [20, 91]. Individual breath-hold time-frames of our patients are $10-20$ s. Treatment beams are delivered with FFF-technique, leading to very fast plan delivery of approximately $2-4$ min, excluding the approximately $3-8$ interruptions for free breathing [25, 92].

Hence, fast and reliable hypofractionated image-guided breath-hold SABR of lung lesions with FFF technique is successfully implemented into clincal routine. The only remaining weak point in the daily treatment chain is the slow pre-treatment imaging under repeated breath-hold, which still offers room for improvement and leads to the scope of this thesis. The combination of CBCT image-guided patient positioning, hypofractionated lung SABR treatment and computer-assisted breath-hold gating resulted in excellent treatment outcomes [20, 67]. With FFF-treatment beam delivery technique, utmost acceleration of treatment was achieved. Current imaging techniques, however, still lack of acceleration improvement, leading to imaging taking as long as the treatment delivery itself.
Initially, continuous CBCT image acquisition was performed in repeated breath-hold, generating a volume reconstructed from 65% breath-hold phases and acceptable image quality with small motion artifacts. Acquisition times of $40-120$ s are beyond the ability of most patients to hold their breath [21].
A new version of CBCT-software improves image quality by allowing the CBCT system to interrupt image acquisition in phases of spontaneous breathing. These multiple breathing interruptions however lead to an even longer imaging time (up to $3-4$ min) [19, 92]. A non-clinical kV-CBCT preset with minimum requirements such as gantry rotation of 180° (+ cone-angle) in accelerated rotation speed would still need 30 s for image acquisition and thus requires most likely more than one breathing interruption. To prevent image quality degradation through residual motion artifacts caused by repeated breath-hold imaging and to further improve patient comfort, CBCT image acquisition within one single breath-hold phase (typically between $10-20$ s) would be ideal.

In our department, dynamic imaging of low-dose combined kV-MV CBCT was recently developed [18, 99]. This single breath-hold ultrafast kV-MV CBCT imaging (~ 15 s), target re-positioning (~ 2 min) and DIBH FFF-SABR ($\sim 2-4$ min) would reduce the total treatment to ≤ 15 min. Ultrafast kV-MV CBCT development was

recently completed by our small team of researchers and is now ready to be introduced in clinical routine. A paper on the finalized implementation of kV-MV was recently submitted for puplication [17].

Towards legal approval as in-house medical product and towards clinical implementation and a first patient-trial, our novel kV-MV CBCT imaging method had to be evaluated and compared with conventional, clinically established techniques based on phantom studies.

In this thesis, characterization, concept development, accomplishment and evaluation by means of specific "acceptance tests" of our novel kV-MV CBCT imaging technique was performed regarding (1) applied imaging dose, (2) image quality and (3) image registration for patient positioning accuracy.

2 Materials and Methods

For legal approval of novel kV-MV CBCT and to pave the way for implementation into clinical routine, several aspects of acceptance tests had to be performed and compared with conventional, clinically established techniques. The concept development, accomplishment and evaluation of these comparison tests based on phantom studies were the aim of this thesis.
In section 2.1, a detailed survey of kV-MV CBCT development is presented, from initial idea to final automized workflow ready for evaluation of clinical applicability and competitiveness with other CBCT imaging techniques. These clinical and non-clinical CBCT imaging techniques are introduced in section 2.2. Novel kV-MV CBCT was compared with these in all applied acceptance tests. Thereafter, the measurement concepts, the performance and the evaluation methods of the three acceptance tests are described: (1) dosimetry (2.3), (2) image quality (2.4) and (3) registration accuracy (2.5).

All measurements were performed in static phantom position. KV-MV is delivered within one breath-hold, therefore no residual tumor motion is expected. The other imaging techniques exceeding single breath-hold time were also measured in static position, to compare kV-MV with the best-achievable image quality and to not unnecessarily complicate the measurement execution.

Primarily, the measurements in this thesis were conducted on a clinically commissioned treatment Elekta Synergy linac (Integrity 1.2) equipped with a foldout MV detector iView GT v3.4 as well as a perpendicularly mounted kV-CBCT XVI v4.2.2 (all Elekta AB, Stockholm Sweden). This main linac is in the following called "LINAC_1". Only in the dosimetry study (2.3), a newer version of kV-CBCT was additionally compared with. This latest available CBCT software version XVI v5.0.2 was installed on a clinical Elekta VersaHD linac, in the following called "LINAC_2".

2.1 Novel ultrafast combined kV-MV CBCT: survey from initial idea to final workflow

The initial idea to combine kV and MV beam CBCT was presented by Yin et al. [104]. However, they only realized a step-and-shoot method. With our novel method of ultrafast combined low-dose kV-MV CBCT [18], the gantry dynamically rotated only 90° and thus significantly reduced image acquisition time to approximately 15 s. The development of kV-MV CBCT was accomplished on LINAC_1. Image acquisition was performed simultaneously, creating 90° kV and 90° MV projections. Thus, a full 180° volume data set was acquired and reconstructed by filtered backprojection. Our additional in-house developed hardware system managed kV and MV detector panel readout signals [99] and hence synchronized kV and MV image acquisition. The kV-MV CBCT imaging strategy was automated to be performed in real-time [15, 16].

In the following subsections, a short survey of the development of ultra-fast combined kV-MV CBCT imaging is provided, from the initial idea to proof of principle to final automated version.

2.1.1 Initial idea: step-and-shoot combined kV-MV CBCT by Yin et al.

The initial idea to combine the kV CBCT imaging system together with the MV treatment beam and the corresponding portal imaging detector was presented by Yin et al. in 2005 [104]. Their motivation to aggregate both imaging modalities were (1) image acquisition time reduction by 50%, (2) inclusion of treatment beam information in the patient position verification otherwise performed exclusively by kV-CBCT, (3) streak artifact reduction based on metal parts in the patients' body by MV contribution.

The study was performed on a clinical Varian Clinac 21EX linear accelerator with MV portal imager and kV On-Board-Imager (OBI) orthogonally mounted to the linac gantry (all Varian Medical Systems CA, USA). The main achievements of this study to develop an aggregated dual-energy kV-MV imaging method were:

- KV and MV projection acquisition at identical beam orientations in step-and-shoot mode with 2° steps over a 100° gantry arc (in total 48 kV and 48 MV projections).
- Separated volume reconstruction with MLS-ART reconstruction algorithm [45].
- Combination of both kV and MV contribution by projection-based data conversion, i.e. projections provided by overlapping area of cone-angle of 10° were used to estimate conversion function.

Phantom measurement results were presented. However, the initial idea of dual energy CBCT to save time during image acquisition could not be realized. The limitations for clinical implementation of this study were:

- Image acquisition was performed offline, kV and MV projections were acquired sequentially in a step-and-shoot mode, increasing imaging time to a clinically non-applicable time extent.
- MV dose output was 2 MU per projection, i.e. 96 MU over the full 100° arc; kV dose output was 100 kVp and 0.5 mAs per projection.
- The reconstruction algorithm MLS-ART [45] was slow compared to clinically used Filtered Backprojection [40].
- MV contribution reduced soft-tissue contrast.

This study thus provided a proof-of-principle [104] and offered strong potential for development of an on-line, continuous and fast kV-MV dual-energy CBCT imaging method to be implemented into clinical routine.

2.1.2 Unsynchronized kV-MV CBCT: proof of principle

Our research group started the development of a clinically applicable combined kV-MV CBCT imaging technique based on continuous gantry rotation and low MV-dose output on LINAC_1 in 2008 [18]. Simultaneous acquisition of both kV and MV projections during continuous gantry rotation was realized in accelerated mode, requiring only 15 s for a 90° scan. To achieve low MV dose output, linac parameters such as gun current and tuner rest had to be adapted. The linac parameters were manually entered in the linac control software; by trial and error, a

suitable parameter setting was established. The lowest MV dose output still providing sufficient image quality was 8.25 MU for 40 MV projections, i.e. 0.21 MU/projection. A dose estimation resulted in 82.5 mGy for the 90° scan [18]. The kV contribution was set up by adapting a clinically established preset to our requirements (smallest possible dose output, 90° gantry rotation). The dose output of the kV contribution was thus comparatively small with an estimated dose of 6 mGy for 60 kV projections [18].

The biggest challenges however were the data handling of the MV contribution. Since the MV treatment beam and the portal imaging detector were not designed for continuous readout, projection angle information was missing and stripe artifacts occurred in the MV projection data. The stripe artifacts were introduced due to the missing synchronization between MV detector readout and linac pulse irradiation, i.e. during the readout time frame of the MV detector, the linac was pulsing multiple times, leading to intensity fluctuations in each MV projection. A software workaround was developed to correct for these stripe artifacts in a post-processing step of MV data [18]. Unfortunately, the stripe artifact occurrence did not follow any systematic scheme, thus, the software workaround based on simple gradient threshold method was error-prone. The projection angle information was determined by attaching a high-contrast ball-shaped marker next to the phantom and tracking the current angle in the sinusoidal curve of the gantry rotation. The projection angle determination was performed with an in-house developed marker tracking software [18]. However, successful tracking was depending on the image quality of the MV projection data. An expected spatial isocenter shift for different gantry angles due to continuous gantry rotation and resulting mechanical forces acting on sources and detectors was also corrected in a post-processing step of MV projection data.

To individually reconstruct both 90° kV and 90° MV projection data, a reconstruction algorithm based on filtered backprojection [40] was implemented in-house on a graphics processing unit using CUDA technology [18]. A reconstruction of 100 projections (according to 90° kV-MV CBCT) into 3D volume data took 6 s. After successful reconstruction, both volumes were combined by voxel-to-voxel addition, resulting in a final combined kV-MV CBCT volume.

This proof-of-principle study of combined kV-MV CBCT was published in 2010 by Blessing et al. [18]. Phantom measurements showed sufficient image quality and the results convinced the linac manufacturer of the potential of ultrafast kV-MV

CBCT imaging within one breath-hold phase of 15 s. The manufacturer agreed to collaborate with our research group and provide us with essential details about linac control software, to replace the workarounds with an improved and reliable strategy.

2.1.3 Synchronized kV-MV CBCT

To overcome the problem of stripe artifacts in the MV projections, the linac pulsing and the MV detector readout had to be synchronized. Therefore, a hardware was developed which controlled the number of linac pulses per frame and defined the point when to start MV detector readout. This dedicated synchronization hardware was developed by a colleague in our research group, in close cooperation with the linac manufacturer. The FGPA-based hardware allowed communication between both independent kV and MV imaging subsystems. The kV panel trigger pulses were used to synchronize the MV panel trigger. Furthermore, the linac pulsing was controlled by the hardware, enabling low MV dose output. The system was described in Wertz et al. [99].

The kV subsystem remained unchanged, the kV pulse rate of 180 ms was used as a clock for the hardware, i.e. each MV projection corresponded to a 90° shifted kV projection. With the synchronization hardware, stripe artifact occurrence could be eliminated. The linac parameters reducing the linac output to low MV-dose matching with the triggered linac pulses provided by the hardware were entered manually in the linac control software. Manual interaction was however not only error-prone, but also required too much time. To successfully accomplish kV-MV CBCT imaging, all required steps from initiating the kV and the MV beam to starting simultaneous image acquisition had to be performed within a few seconds. Otherwise, several interlocks, such as disabled simultaneous imaging of kV and MV mode, would be re-activated. With the synchronization hardware, a low-dose linac output of 5 MU was achieved, resulting in an estimated MV dose exposure of approximately 60 mGy to the patient. The applied dose from the kV-contribution was expected to be negligibly small, i.e. approximately 3 mGy.

To correct for residual motion of the sources and detectors due to mechanical forces occurring through continuous gantry rotation, the projection data had to be corrected for spatial isocenter shifts. The CBCT software (XVI) already considered flexmap

correction internally. For MV projection data, however, our research group had to develop the flexmap data. The generation of the flexmap correction table was performed in a similar procedure as for kV CBCT.

In Wertz et al. [99], the synchronized combined kV-MV CBCT imaging technique was published. Phantom measurements were performed to evaluate kV-MV CBCT for clinical feasibility. The results were compared with a non-clinical 360° kV-only CBCT preset. It was determined that kV-MV CBCT provided sufficient image quality for high-gradient areas such as in the lung. However, in this synchronized combined kV-MV approach, a lot of manual interaction was still required, e.g. setting of linac parameters, derivation of MV angles from kV database and introduction of flexmap. Furthermore, full end-to-end workflow was not yet realized, the data post-processing had to be performed offline, and registration was not yet possible. Towards clinical implementation, the final kV-MV CBCT workflow had to be automated, with least possible manual interaction, user-friendly application and assured safe clinical operation.

2.1.4 Final automated kV-MV-CBCT workflow

Novel combined kV-MV CBCT was set up as a simultaneous 90° kV and 90° MV scan [18]. An overlap of additional +10° cone-angle had to be enclosed to enable full reconstruction based on filtered backprojection (FDK approach) [40].
The kV contribution was set up with 100 kVp, 0.1 mAs per frame, an S20 collimator with field size 27.67 cm × 27.67 cm in isocenter, and 100° (90° + cone-angle) gantry rotation. The gantry speed was in accelerated mode (1 rpm), resulting in an image rotation time of 15 s. The acquired kV projections were post-processed within the clinical XVI system (100 projections).
Since the MV linac and detector were not designed for continuous readout (the vendor did not intend to provide MV-CBCT), tremendous effort had to be spent on achieving continuous, low-dose MV imaging [18, 99]. To avoid artifacts introduced by the pulsing of the linac during panel readout, a dedicated FPGA-based hardware was developed by a colleague in our research group. This hardware used the kV detector pulses to trigger the MV-detector and to control the MV gating pulses. The hardware guaranteed, that no linac pulse occurred during MV readout [99]. Since the

readout rate of the MV detector is five times slower than the kV detector readout, only every fifth kV-pulse could be used to trigger the MV detector readout, resulting in five times less MV than kV projections. The MV contribution preset was set up as follows: MV low-dose output of 4 MU was distributed equally to the 19 acquired MV projections per 90° rotation. The field size was 25 cm × 25 cm in isocenter. Details about the technical setup are listed in Table 2.1.

For the automated workflow, an application program was developed in a seperate PhD study by a colleague in our research group [16], including all required steps in generating a kV-MV CBCT volume. An article on the end-to-end test of finalized kV-MV CBCT was recently submitted to a peer-reviewed journal.
Using a dedicated communication port (COM), the linac parameters were adjusted to achieve low MV dose output (4 MU distributed over 90°) and current gantry angle position was read out continuously. MV projections were acquired and post-processed according to standard procedures (such as gain, offset, bad pixel and flexmap calibration). KV and MV volumes were reconstructed separately, using our GPU accelerated reconstruction. The MV contribution was converted to kV-equivalent scales by reconstruction-based histogram matching and both kV and MV volumes were combined. Finally, the kV-MV 3D volume replaced the initial kV-volume in the XVI registration tool for further routine processing [15, 16].

2.2 Imaging modalities for the comparison studies

In this thesis, the novel ultra-fast imaging technique of combined kV-MV CBCT was compared to several clinical and non-clinical alternative CBCT imaging techniques, to evaluate clinical applicability and to point out expected benefits compared to common clinically established techniques. The clinical and non-clinical CBCT imaging techniques compared in this thesis are described in the following subsections. Technical details are listed in Table 2.1.

Clinical kV-Chest$_1$ CBCT

On LINAC$_1$, the conventional kV-Chest$_1$ CBCT preset was routinely used clinically for lung SABR. The CBCT software version XVI v4.2.2 enabled kV radiation with a

footswitch and 3D volume image acquisition in continuous mode only. The setup of kV-Chest$_1$ CBCT preset was 120 kVp, 1 mAs per frame, an M20 collimator with field size 42.64 cm × 27.67 cm in isocenter, no additional filter ("F0"), and 360° gantry rotation with rotation speed of $^1/_2$ rpm (Table 2.1). Image acquisition time was thus 2 min.

Clinical kV-Chest$_2$ CBCT

For the dosimetry test (2.3), the clinical preset kV-Chest$_2$ of the latest available CBCT software version was measured and evaluated for up-to-date comparison with kV-MV. The software version XVI v5.0.2 was installed on LINAC$_2$. The kV-Chest$_2$ preset differed slightly from the kV-Chest$_1$ preset of previous XVI version 4.2.2. A bow-tie filter ("F1") was applied and the nominal tube current (mA) and pulse duration of exposure (ms) were reduced, as was thus the nominal dose. The x-ray tube potential of 120 kVp remained unchanged, as well as the collimator field size, the detector position, rotation angle and speed. Acquisition time remained the same (2 min), however, beam interruptions were possible in case of DIBH treatment, extending imaging time to $3-4$ min (Table 2.1).
Comparison of kV-MV CBCT with kV-Chest$_2$ CBCT regarding image quality and registration accuracy was not necessary, since image quality and registration accuracy followed the same standard requirements as in previous versions. From XVI version 4.2 to 5.0, changes in reconstruction algorithm allowed reduction in mAs without increasing noise [38]. The volume image acquisition could be interrupted, e.g. in case of DIBH treatment. Image quality could be greatly improved for lung tumors scanned in repeated breath-hold (DIBH), since residual motion artifacts were eliminated [21]. However, imaging time also increased considerably to $3-4$ min [19, 92].

kV$_{180}$ CBCT

For correct reconstruction, filtered backprojection methods require a minimum scan angle of 180° (plus 10° cone-angle in this study) with centered detector panel [40, 87]. To compare with this minimum requirement setup of kV-CBCT, an additional non-clinical kV$_{180}$ CBCT preset was generated and applied on LINAC$_1$. Tube settings

were the same as in the kV contribution of novel kV-MV CBCT (100 kVp, 1 mAs per frame). Rotation speed of 1 rpm was generated and applied, leading to a reduced imaging time of 30 s. Considering breath-hold treatment, this fastest achievable mono-energetic imaging method only requires one interruption for free breathing, reducing imaging time to approximately 40 s (Table 2.1).

$\mathbf{MV_{180}}$ CBCT

The development of the kV-MV synchronization hardware also allowed for creating an MV_{180} CBCT preset on $LINAC_1$, using the same low-dose MV beam characteristics (8 MU equally distributed over a 180° arc plus 10° cone-angle). Due to the triggered linac pulse and the inability of the MV panel to constantly read out, the projections could only be acquired every 5°, resulting in a dataset of 36 projections. The gantry speed was 1 rpm and the image acquisition time for breath-hold treatment with one necessary free breathing phase was $(30 + 10)$ s (Table 2.1).

Preset	kV-Chest$_1$ CBCT	kV-Chest$_2$ CBCT	kV$_{180}$ CBCT	MV$_{180}$ CBCT	kV-MV CBCT
Output characteristics	120 kVp 1 mAs (25 mA, 40 ms) per frame	120 kVp 0.4 mAs (20 mA, 20 ms) per frame	100 kVp 0.1 mAs (10 mA, 10 ms) per frame	6 MV linac (8 MU)	**kV:** 100 kVp 0.1 mAs (10 mA, 10 ms) per frame **MV:** 6 MV linac (4 MU)
Acquisition length	360°	360°	180° + cone-angle (−90° to +100°)	180° + cone-angle (−20° to +170°)	90° + cone-angle (0° to +100°)
Panel position	off-centered (M)	off-centered (M)	centered (S)	centered (S)	centered (S)
Filter, Collimator (field size)	F0 (empty) M20 (27.67 cm × 42.64 cm)	F1 (bow-tie) M20 (27.67 cm × 42.64 cm)	F0 (empty) S20 (27.67 cm × 27.67 cm)	F0 (empty) S20 (27.67 cm × 27.67 cm)	**kV:** F0 (empty) S20 (27.67 cm × 27.67 cm) **MV:** 25 cm × 25 cm
Number of frames	650	660	190	36	**kV:** 100 **MV:** 19
Imaging speed	1/2 rpm	1/2 rpm	1 rpm	1 rpm	1 rpm
Acquisition time	2 min	*minimum* 2 min	*minimum* 30 s	*minimum* 30 s	15 s
Nominal dose	16 mGy	5 mGy	0.4 mGy	8 MU	**kV:** 0.2 mGy **MV:** 4 MU

Table 2.1: Technical settings for different imaging presets, including kV-MV CBCT

2.3 Dosimetric properties of kV-MV CBCT

In this section, imaging dose exposure to the patient was investigated and compared to clinically established (kV-Chest$_1$ and kV-Chest$_2$ CBCT) as well as fastest-achievable monoenergetic non-clinical imaging techniques (kV$_{180}$ and MV$_{180}$ CBCT). A standard dose value for kV-MV CBCT preset was defined for future quality assurance (QA). The phantom dose measurements were performed on two clinical linacs (LINAC$_1$ and LINAC$_2$).

All absorbed dose measurements were corrected following either the AAPM TG protocol 61 [72] for kV-energy range, or the IAEA TPS 398 [56] for MV-range. For both energy ranges, measurements were performed with two differently-calibrated air-filled point-dose flexible cylindrical ionization chambers (Type 31013, 0.3 cm^3 sensitive volumes) and a UNIDOS E Universal dosemeter (all PTW Freiburg GmbH, Freiburg, Germany). The first ionization chamber was calibrated in air kerma[1] for kV-range (50 kVp – 150 kVp), the second ionization chamber was calibrated on absorbed-dose-to-water for 60-Cobalt (MV-range) [86]. The determination of beam qualities and calibration factors for the dose measurements in both kV- and MV-energy ranges are described in sections 2.3.1 and 2.3.2. To directly compare kV and MV dose, the differences in relative biological effectiveness had to be taken into account. A conversion factor for MV-dose to kV-equivalent relative biological dose is presented and discussed in section 2.3.3. Section 2.3.4 describes the phantom setup for (1) the patient simulation for exposed dose in an inhomogeneous thorax phantom and (2) the determination of standard QA dose value, the CT dose index (CTDI).

2.3.1 kV beam quality and dose calculation

Following the task group (TG) protocol 61 from the American Association of Physicists in Medicine (AAPM) [72], kV beam qualities for the applied beam setups were characterized by measuring the half-value-layers (HVL) of Aluminium and calibration factors were determined accordingly.

[1] kerma = kinetic energy released per unit mass

kV beam quality - determination of HVL

The specification of beam quality for low-energy x-ray beams is typically given by the peak voltage (kVp) and the half-value-layer (HVL). The HVL of an x-ray beam is defined as the thickness of an absorber material that reduces the initial dose output to one half (see equation 2.2) [49, 62].

The setup for HVL measurements is leaned on the AAPM TG61 report [72]. A self-made collimator with field size $(5.5 \times 5.5)\text{cm}^2$ in the isocenter was used to achieve narrow-beam geometry. Through narrow-beam geometry, the exposure reading should predominantly collect the transmitted photons; scattered radiation from interaction with the absorber material is minimized by this setup [62, 97]. In our setup, the x-ray source was positioned at 0° and the detector was moved out of the field-of-view (FOV). A measurement stand on top of the treatment couch aligned both the ionization chamber and the varying Aluminium absorbers with the center of the FOV (see Figure 2.1a). To ensure full coverage of the sensitive volume and to avoid anode heel effect, a planar image was acquired with XVI. After setup verification the flat panel detector was retracted for protection. The source to surface distance (SSD) was 100 cm for the ionization chamber, the Aluminium absorbers were positioned at SSD 50 cm. The thickness of the attenuator varied from $0.01 - 10.31$ mm (Figure 2.1b), the purity of Aluminium was 99.9%.

The HVL was measured for three CBCT presets, kV-Chest$_1$, kV-Chest$_2$ and the kV contribution of kV-MV CBCT with the same kVp and mAs settings as kV$_{180}$ CBCT. To achieve static irradiation from a fixed gantry angle the presets were modified accordingly. Since the HVL measurements were relative measurements, the number of acquired frames were non-relevant. 100 frames were acquired for kV-Chest$_1$ and kV-Chest$_2$. Since the kV contribution of kV-MV had less dose output (smaller kVp, smaller mAs), the number of frames were increased to 300. All preset collimators were replaced with the narrow-beam collimator.

To determine the HVL for each beam setting, first, the initial dose output I_0 with zero absorber (free in air) had to be measured. In this experiment, I_0 was measured four times and the average value was considered as 100% relative dose output. Thereafter, the thickness of the Aluminium absorbers was increased in different step sizes, and dose output was measured. To increase the accuracy of the measurement in the

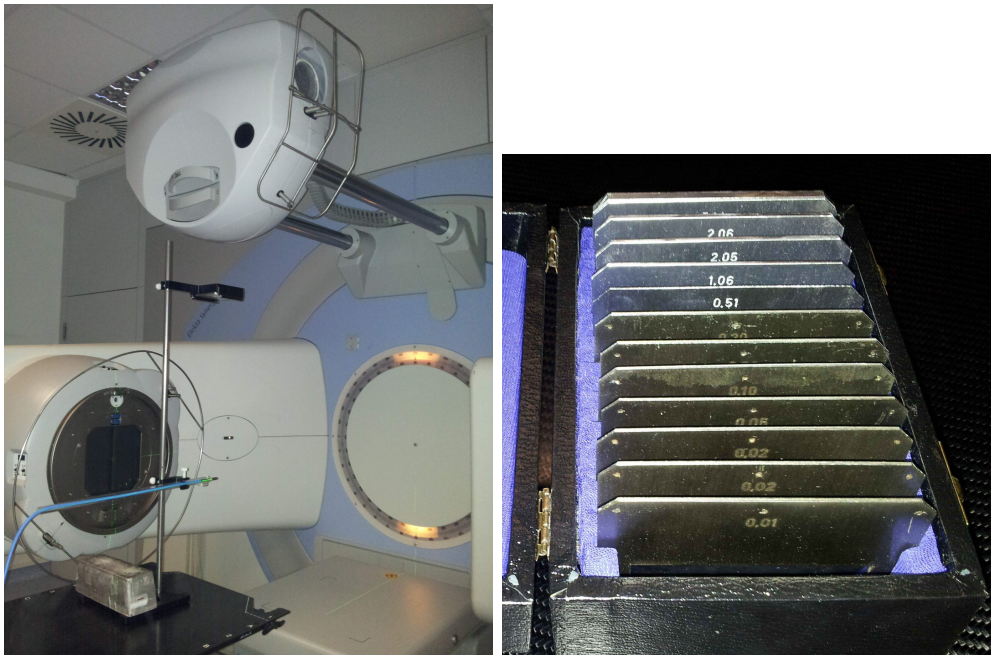

(a) **(b)**

Figure 2.1: kV beam quality: (a) measurement setup for HVL determination, (b) Aluminium absorbers (thickness $0.01-5.14\,\text{mm}$).

$I_0/2$ region the step size was reduced to 0.01 mm which was the smallest available Aluminium plate in this study.

Different approaches to determine HVL

To find the best mathematical description of the measured HVL data, different fit functions were tested and compared:

Monoenergetic approach following Lambert-Beer-Law [49, 62]: In literature, the HVL is usually calculated under ideal conditions of a monoenergetic x-ray beam and narrow-beam geometry, following the Lambert-Beer-Law:

$$I(x) = I_0 e^{-\mu x} \tag{2.1}$$

$$HVL_{LB} = \frac{\ln 2}{\mu} = \frac{0.693}{\mu} \quad \text{for } I(HVL_{LB}) = \frac{I_0}{2}\,, \tag{2.2}$$

with I_0 the dose output (intensity of the beam) with no additional absorber material in the beam ($x = 0\,\text{mm}$), x the thickness of the additional absorber material and μ the linear attenuation coefficient. The linear attenuation coefficient μ depends on the energy of the x-rays and the atomic number of the absorber material.

However, x-rays produced by an x-ray generator are polyenergetic. The x-ray energy spectrum consists of a continuous energy distribution of bremsstrahlung photons and discrete lines of characteristic radiation depending on target material, kVp and beam filtration. Inherent beam filtration such as Aluminium filters in case of diagnostic and superficial energy range ($50 - 200\,\text{keV}$) is used for beam hardening. Low energy photons are absorbed by matter such as the patient's body and thus do not reach the imaging detector. They do not contribute to image quality but only increase the radiation dose applied to the patient. Inherent filtration is added to selectively remove low-energy photons, harden the beam and reduce imaging dose to the patient [49, 62]. In our experiment, the inherent filtration of the x-ray tube (at 100 kVp) in XVI v4.2.2 is 6.3 mm Aluminium equivalent [35], and 6.8 mm Aluminium plus 2 mm Aluminium bow-tie filter thickness in the central beam for XVI v5.0.2 [37].

Quasi-monoenergetic approach: Two-Point-Interpolation method by Hill et al. [50]: In many publications, the polyenergetic characteristics were simplified and an effective monoenergetic energy with effective attenuation coefficient μ_{eff} was assumed. If a log scale was used for the HVL measurement values, a linear decrease was expected and HVL could be calculated with "two-point linear interpolation" [50, 68, 98]:

$$I(x) = I_0 e^{-\mu_{eff} x} = I_0 e^{-\int_0^{E_{max}} \mu(E) dE x} \tag{2.3}$$

$$\begin{aligned} HVL_{LI} &= x_1 + (x_2 - x_1)\left(\frac{ln\left(\frac{I_0}{2}\right) - lnI(x_1)}{lnI(x_2) - lnI(x_1)}\right) \\ &= \frac{x_1 \ln\left(\frac{2I(x_2)}{I_0}\right) - x_2 \ln\left(\frac{2I(x_1)}{I_0}\right)}{\ln\left(\frac{I(x_2)}{I(x_1)}\right)} \qquad \text{with:} \qquad x_1 < HVL < x_2 \end{aligned} \tag{2.4}$$

This approach however does not reflect reality. If an x-ray beam passes through

material (e.g. absorber material), low energy photons are absorbed to a greater extend and the beam becomes harder; the attenuation coefficient μ_{eff} is reduced. This effect can be described with a beam-hardening coefficient η. With increasing absorber thickness x, the rate of change in μ decreases, the slope of the logarithmic HVL measurement curve decreases and is thus not linear anymore [62]. A useful measure of the polyenergetic nature of x-ray beams is the homogeneity index $HI = \frac{HVL}{QVL}$, calculating the ratio between the attenuator thickness for 50% I_0 (HVL) and the thickness for 25% I_0 (quarter-value-layer QVL). Unfortunately, the homogeneity index was not determined in our experiment because we did not have enough Aluminium absorber plates to reach 25% of the initial dose exposure.

In literature several proposals to analyze the transmission characteristics in terms of varying attenuation coefficient μ and beam-hardening coefficient η can be found.

Polyenergetic approach by Bjärngard/Shackford [14]: In 1994, Bjärngard and Shackford analyzed the beam hardening effect in high-energy x-ray beams of 6MV and 25MV. With increasing absorber thickness x, the beam became harder and the attenuation coefficient μ decreased. The beam energy spectrum turned narrow and the beam-hardening coefficient was reduced. They described the transmission of the x-ray beam by an exponential function with a second-order polynominal in thickness x. This equation for changing attenuation coefficient μ was determined experimentally. The HVL could be calculated by solving:

$$I(x) = I_0 e^{-\mu x(1-\eta x)} = I_0 e^{-\mu x+\mu\eta x^2} \tag{2.5}$$

$$HVL_{BS} = \frac{\mu - \sqrt{\mu^2 - 4\mu\eta \ln(2)}}{2\mu\eta} \tag{2.6}$$

Polyenergetic approach by Yu et al. [106]: The study from Yu et al. was based on the study of Bjärngard/Shackford [14], but they stated that the change rate of attenuation coefficient μ also varies with absorber thickness. The incident beam quality before beam-hardening was μ_0. They concluded with equation 2.7 the larger the absorber thickness, the slower the attenuation coefficient changes. Equation 2.8 could be used to calculate the HVL.

$$I(x) = I_0 e^{\frac{-\mu_0 x}{1+\eta x}} \tag{2.7}$$

$$HVL_{YU} = \frac{ln(2)}{\mu_0 - \eta \ln(2)} \tag{2.8}$$

Polyenergetic approach #1 by Kleinschmidt [65]: In 1999, Kleinschmidt published a comparison study between Bjärngard/Shackford [14] and Yu et al. [106] and two alternatives suggested by him. He evaluated the different approaches for several high-energy beams of $4-20$MeV. His first alternative approach was a slight change of the equation of Yu et al., taking the square of their denominator. The HVL could be calculated by solving the quadratic equation:

$$I(x) = I_0 e^{\frac{-\mu_0 x}{(1+\eta x)^2}} \tag{2.9}$$

$$HVL_{KS1} = \frac{-(\mu_0 - \eta \ln(2)) + \sqrt{(\mu_0 - \eta \ln(2))^2 - 4\eta^2 (ln(2))^2}}{-2\eta^2 \ln(2)} \tag{2.10}$$

Polyenergetic approach #2 by Kleinschmidt [65]: Kleinschmidt stated, that the previous equations (Bjärngard/Shackford and Yu et al.) were appropriate fits for limited depths, however could lead to negative linear attenuation coefficients if the absorber thickness was large enough. Since this is physically impossible, his second alternative approach specified more conditions such as a minimum attenuation coefficient $\mu_{E_{max}}$ and a third order polynomial of attenuator thickness dependency (equation 2.11). To determine the HVLs of our study from this equation, Matlab (MathWorks Inc, Natick, MA, USA) was used.

$$I(x) = I_0 e^{-\left(\mu_{E_{max}} + \frac{\mu_0}{1+\eta_1 x+\eta_2 x^2}\right)x} = I_0 e^{-\mu_{E_{max}} x} e^{\frac{-\mu_0 x}{1+\eta_1 x+\eta_2 x^2}} \tag{2.11}$$

$$HVL_{KS2} = \text{determined with Matlab (3rd oder polynomial)}$$

kV dose correction factors

After calculating the HVL for each kV-imaging preset, the appropriate correction factors were determined from the look-up-tables in AAPM TG61, following the dosimetry formalism for tube voltages between 100 and 300 kV [72]:

$$\begin{aligned} D_w &= M N_k P_{Q,cham} P_{sheath} \left[\left(\frac{\mu_{en}}{\rho} \right)_{air}^{water} \right]_{water} \\ \text{with} \quad M &= (M_{raw} - M_0) P_{TP} P_{ion} P_{pol} P_{elec} \end{aligned} \tag{2.12}$$

The in-phantom formalism converted the air-kerma calibrated ionization chamber measurement M [C] to absorbed-dose-to-water D_w [Gy]. The energy-specific air kerma calibration factor N_k [Gy/C] was provided on the ionization chamber calibration sheet provided by the accredited dosimetry calibration laboratory (PTW, Freiburg, Germany), and was preset in the dosemeter. The background dosemeter reading M_0 was internally subtracted from the raw measurement data.
Prior to the dose measurements for our study, the ionization chamber had to be corrected for daily atmospheric conditions, i.e. correction for air pressure P and temperature T:

$$P_{TP} = \frac{P_0(273.2+T)}{P(273.2+T_0)}$$

with reference conditions $P_0 = 1013.25\,\text{hPa}$ and $T_0 = 20°\text{C}$. This correction compensated for possible increase of ionization from the reference measurement in the ionization chamber, leading to higher measurement reading.
The correction factors for ion recombination P_{ion} and electrode polarity effects P_{pol} in the ionization chamber, and the correction factor P_{elec} for the dosemeter were either considered by the calibration laboratory, or were negligibly small [56, 66, 72].

The following correction factors were directly dependent on the beam quality (HVL) of the x-ray tube and were extracted from the look-up-tables in AAPM TG61 [72]:

- $P_{Q,cham}$: overall chamber response correction factor, correcting for the changes in beam quality between measurement and calibration conditions, for the

chamber stem, and chamber displacements in the phantom.

- P_{sheath}: waterproofing sheath correction factor, in case the ionization chamber is not waterproof and requires a waterproof case.
- $\left[\left(\frac{\mu_{en}}{\rho}\right)_{air}^{water}\right]_{water}$: average mass energy-absorption coefficient ratio in water from as conversion factor from air kerma to dose-to-water.

2.3.2 MV beam quality and dose calculation

The determination of MV energy beam quality differed from the kV beam quality procedure, because the MV beam was already hardened by heavy inherent filtration of target and flattening filter. HVL measurements would not lead to significant measurement alterations, therefore, the MV beam quality was specified by the peak energy [62].

The most convenient method to determine the energy of the MV beam was to measure the percent depth dose distribution (PDD) and put it in relation to reference data, i.e. 60-Cobalt energy [49, 62].

MV beam quality - determination of quality index Q

Following the technical report series (TPS) 398 of the International Atomic Energy Agency (IAEA) [56] and the AAPM TG protocol 51 [3], the percentage depth dose curve was measured in a water tank and the beam quality index Q of our clinical 6MV linac beam was determined (LINAC_1).
The reference setup was source-to-surface distance $SDD = 100\,\text{cm}$, the field size was $10 \times 10\,\text{cm}^2$ in isocenter, and the PDD was acquired for a depth of $0 - 30\,\text{cm}$ in a water tank (IBA blue phantom, IBA Dosimetry, Schwarzenbruck, Germany) with a scanning volume ($\text{L} \times \text{W} \times \text{H}$) of $48 \times 48 \times 41\,\text{cm}^3$ (see Figure 2.2). The ionization chamber was positioned with central axis of the beam at the center of the cavity volume.

Figure 2.2: Measurement setup of the water tank to determine the beam quality for 6 MV linac (LINAC_1).

MV dose correction factors

After acquisition of the percentage depth dose curve, percentage dose values of depths 20 cm (M_{20}) and 10 cm (M_{10}) were selected. The beam quality index was defined as:

$$Q = 1.2661 \frac{M_{20}}{M_{10}} - 0.0595 \tag{2.13}$$

The absorbed dose-to-water calculation for high energy beams (MV-range) followed the formalism:

$$\begin{aligned} D_w &= M N_{D,w} k_Q \\ \text{with} \quad M &= (M_{raw} - M_0) P_{TP} P_{ion} P_{pol} P_{elec} \end{aligned} \tag{2.14}$$

Before the first measurement, the background dosemeter reading M_0 was corrected as well as the daily atmospheric conditions P_{TP}. As an alternative to a pressure and temperature correction P_{TP}, one can perform a correction with the check source method for the MV energy range. A reference check source reading of a radioactive material (^{90}Sr) was recorded on the ionization chamber calibration sheet from the accredited dosimetry calibration laboratory (ADCL). The reference value of a given

date for reference conditions, k_p, was set relative to the current check source decay k_m:

$$P_{TP} = \frac{k_p}{k_m} \tag{2.15}$$

This correction factor, as well as the other factors P_{ion}, P_{pol} and P_{elec} were considered internally in the dosemeter (see correction factor description in section 2.3.1).

The absorbed dose-to-water calibration factor for the ionization chamber, $N_{D,w}$, was listed on the calibration sheet from the ADCL and was determined under reference conditions for a ^{60}Co beam.

The beam quality-dependent correction factor was the quality conversion factor k_Q, which converts the calibration factor of reference energy (^{60}Co) to the energy of beam quality Q [49, 62]. A look-up-table is provided in IAEA TRS 398, listing k_Q factors for various ionization chamber types at different beam quality factors Q [56].

2.3.3 RBE - MV to kV dose conversion

The ICRP-60 and ICRP-103 reports [57, 58] suggest to keep a uniform value of $w_R = 1$ for the radiation weighting factor[2] of all low-LET[3]-radiations such as x-rays, electrons and gamma rays of all energies. However, several studies [51, 53, 83] discovered an increase in biological effectiveness with decreasing photon energy. These studies are either based on the epidemic data of the Hiroshima and Nagasaki atomic bombs or on *in vitro* radio-biological measures, and show significant differences in biological effectiveness for different energies.

The relative biological effectiveness (RBE) is defined as:

$$RBE = \frac{\text{Dose from standard radiation to produce a given biological effect}}{\text{Dose from test radiation to produce the same biological effect}} \tag{2.16}$$

[2] The equivalent dose $H_T = {}_R\sum w_R D$ is defined as the product of the (measured) absorbed dose D and the radiation weighting factor w_R.

[3] $LET = \frac{dE}{dl}$: linear energy transfer, defined as the average energy loss dE by a particle of specific energy in a distance dl [84].

Standard radiation is commonly ^{60}Co γ-rays ($E = 1.17\,\text{MeV}$ and $E = 1.33\,\text{MeV}$) [84]. Specified biological effects range from cell killing to tissue damage, mutations and other biological endpoints. Estimates of RBE range from $1-8$ for different biological endpoints [51, 53, 83].

In IGRT, special consideration has to be taken into the increased risk of secondary cancer after irradiation [44, 48, 64]. In the review of Nikjoo et al. [83], some studies are presented in which the RBE between low- and high-energy photons was compared. For the biological endpoint of neoplastic cell transformation, determined RBE values range from $2-4$. Hill et al. [51] and Borek et al. [26] determined an RBE=2 for low vs. high photon energies.

In this dosimetry study, a conservative RBE ratio of $2:1$ for kV vs. MV biological effectiveness was chosen with regard to secondary cancer risk. Since the most common clinical imaging technique is in kV-range, the MV-dose was converted to kV-equivalent dose by reducing the MV dose by one half. In the case of RBE-consideration, the dose unit was changed from Gray [Gy] to Gray-equivalent [GE].

2.3.4 Phantom setup

Dose measurement comparisons between kV-MV CBCT and other CBCT presets were performed on two phantoms. To simulate patient imaging dose exposure, the dose output in several regions of an inhomogeneous thorax phantom was measured and evaluated. In a second measurement study, the kV-MV CBCT dose index was determined and compared to other imaging techniques.

The dose measurements were performed for all presets, kV-Chest$_1$, kV-Chest$_2$, kV$_{180}$, MV$_{180}$ and kV-MV CBCT. For kV-MV however, the dose measurements were performed separately because of the different dose responses of kV- and MV-output. Since the beam qualities of kV and MV differed, two differently calibrated ionization chambers (as mentioned in section 2.3) had to be used, one for kV- and one for MV-dose. This splitting of kV and MV dose components allowed separate evaluation of the dose contributions. Relative biological effectiveness could be considered to convert MV dose to kV-equivalent dose, making dose exposure results comparable to other kV-only CBCTs. The splitting of the kV-MV image acquisition was straight forward, similar to the kV$_{180}$ and MV$_{180}$ presets, just with only 100° rotation. In

this study, no proper image acquisition was necessary, only the dose exposure was recorded. To apply low-MV mode, the normal kV-MV mode was applied, except for not starting the kV-exposure. The kV-software however had to be running, because of the kV panel signal to trigger the low-dose MV linac output.

Inhomogeneous thorax phantom - patient simulation

The inhomogeneous thorax phantom (model 002LFC, CIRS, Norfolk, VA, USA) consists of different materials according to the human thorax, i.e. mimicking two lungs and a spinal cord. The diameter of the phantom was however smaller than a body of a human adult (L × W × H: 43.2 cm × 38.1 cm × 22.9 cm).

In our measurement setup, a target volume was defined in the lower left lung of the phantom. This tumor was to be located in the isocenter (see Figure 2.3). Further dose measurements were performed in the following representative beam positions of the phantom:

1. tumor in lower left lung
2. left lung
3. right lung
4. upper periphery
5. spinal cord
6. body center

In order to spare the contralateral lung in analogy to a patient imaging procedure, the kV-MV, kV_{180} and MV_{180} CBCT presets were designed to rotate only on the side of the tumor location.

The MV contribution in the kV-MV CBCT scan was additionally simulated with the Oncentra treatment planning system (Elekta Oncentra Masterplan OTP, Elekta AB, Stockholm, Sweden) for 4 MU per 100° arc.

CTDI Phantom

Following the quality assurance (QA) protocol of AAPM TG report 179 [12] and AAPM TG report 75 [80], a standard dose value for regular QA was defined for novel

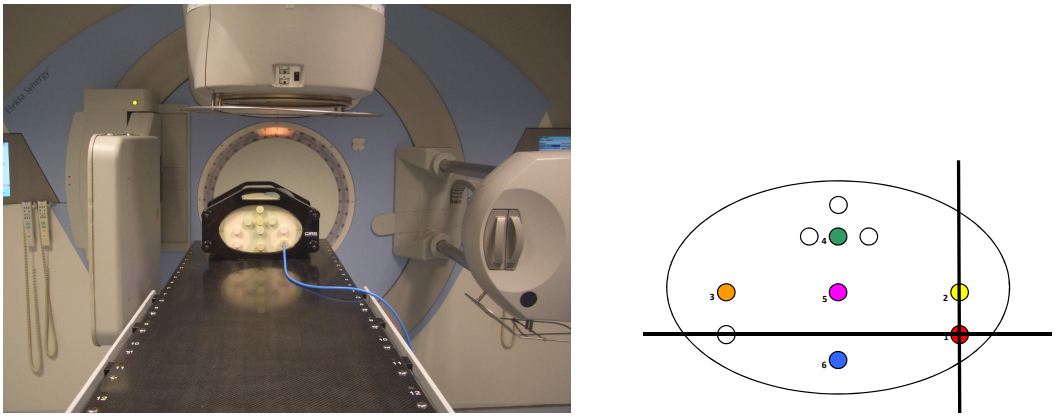

(a) **(b)**

Figure 2.3: Setup of the inhomogeneous thorax phantom, (a) phantom position at LINAC_1 (b) layout of measurement positions.

kV-MV CBCT.

In the last century, the CT dose index (CTDI), initially developed in 1981 as convenient dose measure for diagnostic CT [89], was adapted for cone beam CT dosimetry [39, 54, 94], although a much higher scatter contribution is present in CBCT due to the broad geometry. Initially, the CTDI was measured with a 10 cm long ionization chamber, to collect the dose length product along the longitudinal axis of a diagnostic slice-CT. A cone-beam, however, acquires a 3D volume within a single rotation. Since common field of views of the CBCT are larger than 10 cm, dose equilibrium within the long ionization chamber cannot be guaranteed anymore, the dose exposure could be underestimated. Therefore, Dixon et al. [34] suggested to use a small point-dose ionization chamber to measure in the central beam of the CBCT. Many CTDI determination and dose comparison studies between the different CBCT presets of the two main linac manufacturers Elekta and Varian were published in the last years [4, 28, 54, 63, 94].

The CTDI measurements were performed in the CT body phantom (T40016, PTW, Freiburg, Germany), made of polymethyl-mathacrylate (PMMA) with a density of $\rho = 1.19\,\text{g/cm}^3$. The diameter was 32 cm, the axial length 15.2 cm. As shown in Figure 2.4, the phantom featured five cavities to sequentially insert the ionization chamber: one center and four peripheral positions (at gantry angle 0°, 90°, 180°, 270°). Two point-dose ionization chambers (Type 31013, PTW Freiburg GmbH,

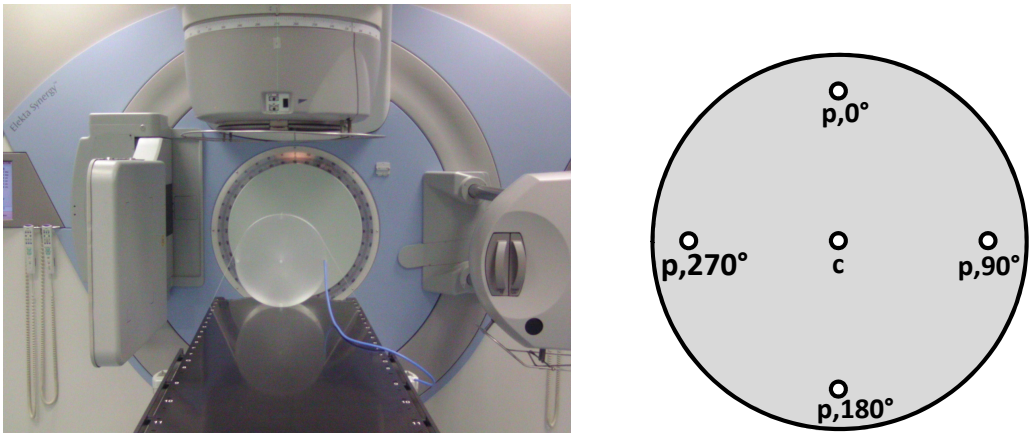

Figure 2.4: Setup of the CT dose body phantom, (a) phantom position at LINAC_1 (b) layout of measurement positions.

Freiburg, Germany) with individual calibration for kV and MV range were used for the CTDI measurements (air kerma calibration for kV range (section 2.3.1) and absorbed dose-to-water calibration for MV range (section 2.3.2)). An additional halved dummy plug was placed into the cavities sequentially together with the ionization chamber at axial midpoint of the phantom to prevent the air gap. The phantom was aligned centrally to the isocenter. The weighted CTDI ($CTDI_w$) was calculated as follows [80]:

$$CTDI_w = \frac{1}{3}CTDI_c + \frac{2}{3}CTDI_p\,, \tag{2.17}$$

with $CTDI_c$ central dose

and $CTDI_p = \frac{1}{4}\left(CTDI_{p,0°} + CTDI_{p,90°} + CTDI_{p,180°} + CTDI_{p,270°}\right)$ peripheral dose (averaged). (2.18)

2.4 Image Quality of kV-MV CBCT

A sufficient image quality is the prerequisite for precise image registration. In this section, a brief evaluation of image resolution (section 2.4.1) and geometrical accuracy (section 2.4.2) is provided.

Similar tests were already published previously with interim kV-MV CBCT data [5, 16, 99]. However, in this thesis, image quality of latest kV-MV CBCT is compared to clinical and non-clinical CBCT presets.

2.4.1 Spatial resolution - CatPhan phantom

Image quality is an important aspect of monthly quality assurance for clinical patient position verification systems, i.e. CBCT [12]. The most common image quality QA phantom is the CatPhan phantom (type CTP 503, The Phantom Laboratory, Salem, NY, USA) [2], shown in Figure 2.5a. The manufacturer of $LINAC_1$ and $LINAC_2$ provides a non-clinical preset for image quality assurance, which is not clinically enabled. This preset is using a high tube output, i.e. high mAs value, and thus high imaging dose which is not justifiable for clinical application. Furthermore, image reconstruction is performed with high resolution, leading to an image reconstruction time too long for clinical application. Thus, these preset settings are exclusively used to evaluate best achievable image quality in terms of spatial resolution, low contrast visibility, uniformity and geometrical linearity, but do not represent the clinical situation.

Spatial resolution is determined by scanning the high resolution module of the CatPhan phantom. In this module, 21 line pair (lp) inserts, with increasing resolution ranging from 1 to 21 lp/cm, are arranged on a circle. The high resolution is evaluated visually [2]. In the customer acceptance test booklet provided by the manufacturer [36], a minimum of 10 line pairs is the specification for the above-mentioned image quality assurance preset, corresponding to a visible rod gap of 0.5mm (Figure 2.5b). This however is by far not achievable with clinical presets, which have to balance between sufficient image quality and lowest reasonable imaging dose.

To put kV-MV CBCT spatial resolution into clinical context, a comparison had to be performed with a clinical preset, i.e. kV-Chest$_1$. The CatPhan phantom was therefore scanned with the spatial resolution module in isocenter position. By visual judgement, the highest number of visible line pair discrimination was determined.

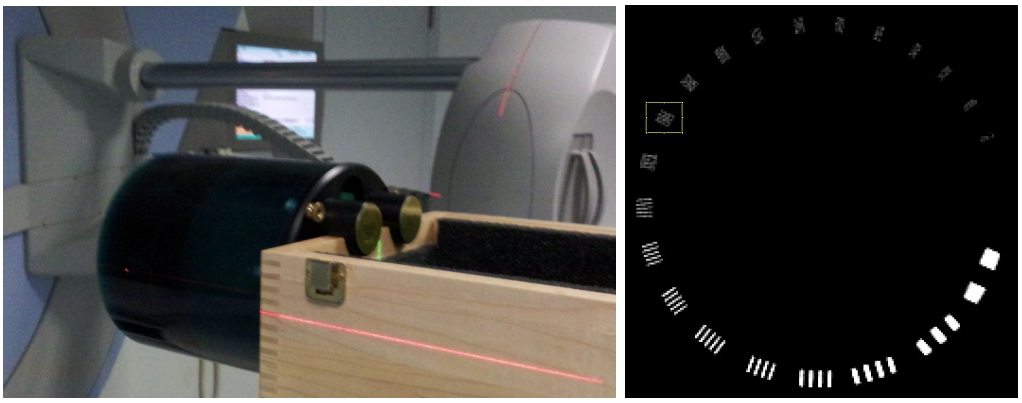

(a) **(b)**

Figure 2.5: Image Resolution: (a) setup of CatPhan phantom, (b) axial slice CBCT scan with the QA preset of high resolution module with 21 line pair per cm gauge (11 line pairs visible).

2.4.2 Geometrical evaluation - inhomogeneous thorax phantom

In line with the following section about image registration (section 2.5), four different custom-made tumor-mimicking shapes were placed in an inhomogeneous thorax phantom. These inlays were sequentially aligned to isocenter position. The tumor-shapes represented a ball, a cylinder with spikes and two star-shaped objects with large and small body. The design of the tumor-mimicking shapes and the phantom setup are shown in Figures 2.6a and 2.6b, respectively.

To determine geometrical accuracy of kV-MV CBCT, the diameter of each tumor-mimicking shape (both body and spikes) was determined with Matlab and ImageJ (http://imagej.nih.gov/ij, v1.48, National Institutes of Health, USA). To compare kV-MV CBCT with clinical and non-clinical CBCT imaging, geometrical accuracy was evaluated also for kV-Chest$_1$, kV$_{180}$ and MV$_{180}$.

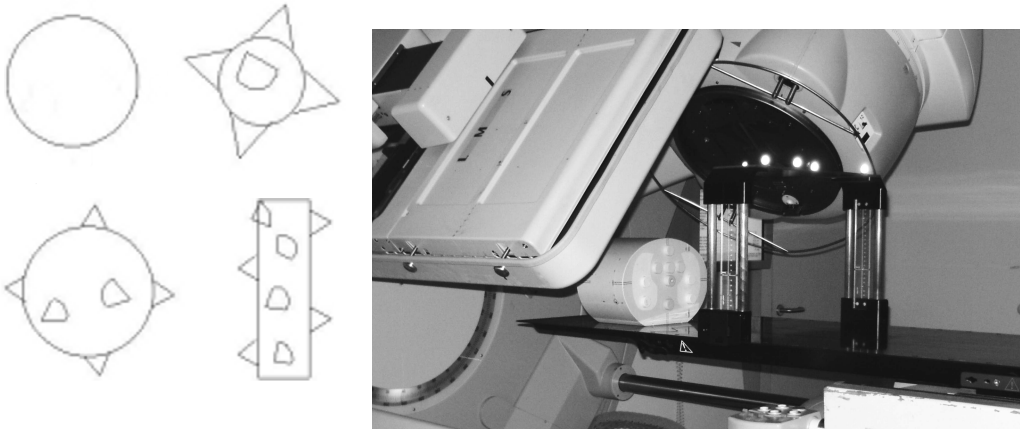

(a) **(b)**

Figure 2.6: Registration accuracy study: (a) shapes of four tumor-mimicking inlays, (b) experimental phantom setup with reference frame for optical tracking.

2.5 Registration Accuracy of kV-MV CBCT

The content of this section was recently accepted as a journal article in "Strahlentherapie und Radioonkologie" [4] [7]*. Some wording may be the same, some tables and figures are directly taken from there.*

In this section, image registration and positioning accuracy for kV-MV CBCT was evaluated and compared with the conventional, clinically established technique kV-Chest$_1$ CBCT, as well as fastest achievable mono-energetic imaging with kV$_{180}$ and MV$_{180}$ CBCT. The registration accuracy test was based on phantom studies, the planning CT (Brilliance Big Bore Oncology, Philips, Hamburg, Germany) was used as reference for registration. All measurements were performed on LINAC$_1$.

In the following subsections, the phantom setup, the realization of high-precision positioning accuracy, the different registration methods (including the development of an own automatic registration framework), the measurement workflow and the evaluation methods are described.

[4] The final publication is available at Springer via http://dx.doi.org/ [10.1007/s00066-016-0947-2].

2.5.1 Registration accuracy phantom setup

Four different custom-made tumor-mimicking shapes were placed in an inhomogeneous thorax phantom. The tumor-shapes represented a ball ($\phi = 15\,\text{mm}$), a cylinder ($\phi = 6\,\text{mm}$, length $= 20\,\text{mm}$) with spikes (3 mm) and two star-shaped objects with large ($\phi = 15\,\text{mm}$) and small ($\phi = 10\,\text{mm}$) body. The inlays were positioned in the lower left lung of the thorax phantom sequentially. The phantom setup was the same as for the geometrical accuracy test in section 2.4.2 (image quality), see Figure 2.6a. Each tumor-shape was marked at isocenter in the planning CT and set as reference CT in the XVI software registration tool.

In total, 10 different shifts were pre-selected randomly based on a Gaussian distribution around the isocenter position (positive on right hand side) and applied in right-left (RL), anterior-posterior (AP) and cranio-caudal (CC) directions. The standard deviation of the Gaussian was chosen to be 1cm in all room directions (Table 2.2).

Room direction	**Isocenter shift** [mm]									
	#1	#2	#3	#4	#5	#6	#7	#8	#9	#10
left → right	5.0	−5.7	−10.6	−12.9	−2.9	1.7	−2.7	−6.4	−4.8	−10.2
posterior → anterior	3.2	−3.5	−11.6	11.0	−6.4	17.7	−8.4	13.1	−4.2	−12.8
caudal → cranial	7.6	3.5	−8.6	9.6	3.9	11.8	−1.6	1.2	14.7	−12.7

Table 2.2: Gaussian distributed isocenter shifts (standard deviation 1 mm) for registration study.

2.5.2 Positioning Accuracy

Optical tracking was used to overcome the limitation of ±0.5 mm registration accuracy of the clinical treatment couch (Elekta Precise with couchtop iBeam evo). The software iGuide (v1.0, Medical Intelligence, Schwabmünchen, Germany), in combination with the corresponding reference frame and its reflective infrared markers detectable by an NDI Polaris camera (see Figure 2.6b), controlled the sub-mm shift of the couch position. The specification of the calibrated 3D tracking system is 0.35 mm RMS [101], however, in this measurement setup, iGuide and optical tracking were used in relative mode only. The frame was not calibrated to isocenter position,

its reflective infrared markers were merely used as a more accurate relative step width controller (0.1 mm step width) compared to standard in-room monitor (1 mm).

2.5.3 Registration Methods

To evaluate and compare the positioning accuracy of different CBCT imaging techniques, each dataset was registered with the corresponding planning CT. Registration was performed offline, since this study focused on the comparison of registration accuracy of differently acquired CBCT volumes, not the precision of couch movement. Thus, executing the registered shift back to the original phantom isocenter was not necessary. The individual matching results were compared to the a priori known and applied random isocenter shifts (see Table 2.2).

Three different registration methods were applied and evaluated, as described in the following.

(I) Manual registration in XVI software

Manual soft tissue matching is routinely used in our clinic and was applied by three experienced physicians to perform registrations. The order of the volumes was mixed when presented to the clinicians such that objectiveness was assured.

(II) Automatic registration in XVI software

Automatic registration provided in XVI software is based on a voxel greyscale intensity value algorithm [52]. An alignment box was assigned around the tumor only, obtaining objective evaluation of local tumor shape contrast and precise tumor registration. In the algorithm, only this alignment box was then taken into account for registration. Since the tumor alignment box was smaller than the distance of most applied isocenter shifts, gross phantom registration had to be performed prior to alignment box setting and following automatic tumor registration. The initial gross alignment was performed manually. The correction reference point was the isocenter position of the planning CT.

(III) Objective automatic registration with self-developed software (in-house)

Since automatic registration in XVI was depending on the initial manual setting of the alignment box, an objective automatic registration had to be developed. For this specific task, there was no software available. Therefore, a framework was developed for automatic registration with Matlab. The rigid intensity-based registration toolkit was used, the similarity metric was based on mutual information [31].
For a given isocenter shift, all CBCT datasets were cropped to the same region of interest (tumor inlays), similar to the alignment box in XVI. However, the Matlab framework achieved the same initial situation for the starting point of registration for all different imaging techniques on each phantom isocenter shift. Assuring this same region of interest was the prerequisite for proper objective comparison study between different imaging techniques. Thus, each phantom shift was determined by registering the CBCT volume center to the planning CT isocenter.

In the following subsections, the self-developed automatic registration framework is explained in detail, the main Matlab code is provided in Appendix A.2. Since the framework behaved in the same manner for all combinations of CBCT on planning CT registration, the different imaging techniques (kV-Chest$_1$, kV$_{180}$, MV$_{180}$ and kV-MV CBCT) are hereby entitled as CBCT or the moving volume. The fixed volume is the planning CT (pCT). To stay conform with the recently accepted publication [7], this self-developed framework is subsequently captioned as "automatic registration (in-house)".

Data handling in Matlab

The 3D volume data of the different imaging techniques had to be imported into Matlab and prepared for precise cropping to the alignment box around tumor only.

- The planning CTs of the four tumor-mimicking shapes were imported as DICOM-files. Since the field of view was adapted manually during the CT scan, the pixel size and number of slices varied for each 3D planning CT volume (pCT). The details of the geometric parameters are listed in Table 2.3. Before CT volume data acquisition, the inhomogeneous thorax phantom was pre-positioned such that each tumor-mimicking shape was roughly in the

center of the chosen field of view. After the CT scan, the precise isocenter was marked manually in the center of each tumor-mimicking shape, which could slightly differ from the center of the 3D volume data set. The isocenter coordinates were stored in the DICOM RTPlan-file of each dataset. Since the coordinate system of the planning CT differed from the Matlab matrix data handling, the isocenter coordinates had to be converted to Matlab-conform spatial system (world coordinates in mm). In Matlab, the coordinate system origin is in the upper left back of the 3D volume dataset. The planning CT isocenter coordinates were thus converted by subtracting the isocenter coordinates provided in DICOM RTPlan[5] from the upper left corner of the backmost slice[6]. Isocenter position was verified visually by comparing the zoomed marked position in Matlab with the zoomed position in planning CT software according to inlay-shape and grey-value pixel.

- The kV-Chest$_1$ CBCT volumes were also imported and sorted as DICOM-files. The center of each volume dataset was the center of rotation, i.e. the kV and MV isocenter coincidence at the linac. Thus the tumor-mimicking shape was off-centered for applied isocenter shifts.
- The volume data of kV$_{180}$, MV$_{180}$ and kV-MV were reconstructed by in-house developed reconstruction software [18], as mentioned in section 2.1. Each data set was stored as raw 3D volume and had to be imported and reordered in Matlab to be conform with the coordinate system of both planning CT and CBCT. Detailed volume data size is given in Table 2.3. Like for clinical kV-Chest$_1$ CBCT, the center of each 3D volume dataset was the center of gantry rotation, i.e. the machine isocenter.

To receive the isocenter shift vector in mm and to handle different spatial resolutions of CT and CBCT datasets, the intrinsic coordinates of each voxel were allocated to a world coordinate system with the function `imref3D` in Matlab.
For example, the planning CT of the ball-shaped tumor-inlay had an image size of $512 \times 512 \times 92$, with a pixel size (X- and Y-direction per Matlab definition) of 0.8809 mm and a slice thickness of 1 mm (Z-direction). The intrinsic limits in Matlab, i.e. the voxel corners in all extremes, were thus [0.5 512.5] in X- and

[5] `RTPlan.BeamSequence...ControlPointSequence.Item_1.IsocenterPosition`
[6] `info_pCT.ImagePositionPatient`

Y-direction, and [0.5 92.5] in Z-direction. The world coordinate limits however were [0.4404 451.4404] in X- and Y-direction, and [0.5 92.5] in Z-direction, thus respectively considering the pixel size and slice thickness.

	3D volume size	**pixel size**	**slice thickness**
pCT (Ball shape)	$512 \times 512 \times 92$	0.8809 mm	1 mm
pCT (Cylinder)	$512 \times 512 \times 98$	0.8574 mm	1 mm
pCT (Star10)	$512 \times 512 \times 87$	0.8514 mm	1 mm
pCT (Star15)	$512 \times 512 \times 114$	0.8652 mm	1 mm
kV-Chest$_1$ CBCT	$410 \times 410 \times 264$	1 mm	1 mm
kV$_{180}$, MV$_{180}$ and kV-MV CBCT	$512 \times 512 \times 512$	0.5 mm	0.5 mm

Table 2.3: Pixel sizes, slice thickness and 3D volume sizes for all imaging methods.

Application of rigid intensity-based registration toolkit

The goal of the developed framework for rigid translational intensitiy-based registration was to determine the isocenter-shift vector of CBCT to pCT, $T_{CBCT \rightarrow pCT}$, as illustrated in Figure 2.7. The developed framework, as applied to all 160 datasets, was covered by five steps:

1. Definition of alignment box around tumor-shape for both pCT and CBCT; determination of transformation vectors $t_{pCT,ab}$ and $t_{CBCT,ab}$
2. Registration of CBCT alignment box to pCT alignment box, determination of registration transformation vector (alignment box) $T_{CBCT,ab \rightarrow pCT,ab}$
3. Back-transformation of $T_{CBCT,ab \rightarrow pCT,ab}$ result from the alignment box to the full 3D volume of both pCT and CBCT, determination of registration transformation vector (full 3D volume) $T_{CBCT \rightarrow pCT}$
4. Calculation of final registered isocenter-shift from the center of CBCT volume to the isocenter position in pCT; transformation of isocenter-shift from Matlab to linac coordinate system
5. Visualization of registered pCT and CBCT volumes for qualitative evaluation

In the following, these steps are described in detail.

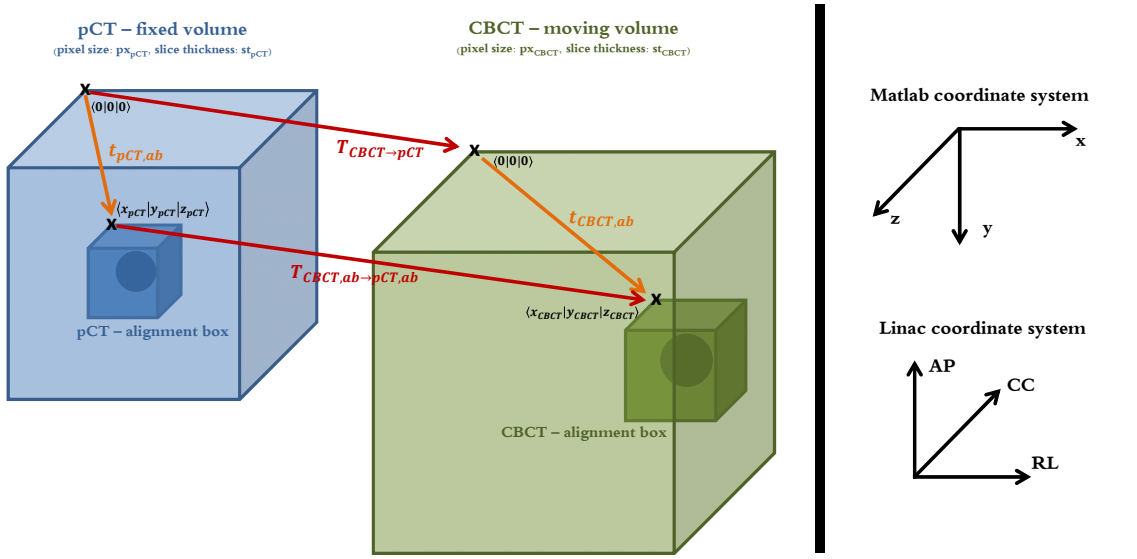

Figure 2.7: Illustration of registration transformation vector from CBCT to pCT for both full 3D volume and alignment box.

1. Alignment box: All datasets (pCT and CBCT) were cropped to an alignment box around the tumor-shapes only. The size of the box was $36 \times 36 \times 36$ pixels; in case of the cylinder-shaped tumor-inlay the z-direction (craniocaudal) was increased to 52 pixels to cover the whole inlay. The tumor-position in the pCT was given by the isocenter coordinates. The data voxels covering the alignment box were thus determined by definition of isocenter position being the center of alignment box pCT. Since the applied isocenter shifts were known, this a priori information and the knowledge of CBCT pixel size helped to assume the rough location of each tumor-shape in each CBCT dataset. This calculated voxel shift was set as the center of alignment box for CBCT. The transformation vectors from full 3D volume to alignment box for both fixed pCT ($t_{pCT,ab}$) and moving CBCT ($t_{CBCT,ab}$) in world coordinates were:

$$t_{pCT,ab} = \begin{pmatrix} (x_{pCT}-1)ps_{pCT} \\ (y_{pCT}-1)ps_{pCT} \\ (z_{pCT}-1)st_{pCT} \end{pmatrix}, t_{CBCT,ab} = \begin{pmatrix} (x_{CBCT}-1)ps_{CBCT} \\ (y_{CBCT}-1)ps_{CBCT} \\ (z_{CBCT}-1)st_{CBCT} \end{pmatrix} \tag{2.19}$$

with $(x_{pCT}|y_{pCT}|z_{pCT})$ and $(x_{CBCT}|y_{CBCT}|z_{CBCT})$ the coordinates of the upper left

back corner of the alignment box of both pCT and CBCT (see Figure 2.7), and ps_{pCT}, ps_{CBCT}, st_{pCT} and st_{CBCT} the pixel size and slice thickness of pCT and CBCT, respectively.

2. Rigid translational registration with Matlab toolkit: The intensity-based registration toolkit provided by Matlab was adapted to our demands. Rigid registration in translational directions was sufficient, since the treatment couch was unable to correct for rotational or deformed registration detection errors. The function `imregtform` determined the registration transformation matrix $T_{CBCT,ab \rightarrow pCT,ab}$ between the alignment boxes of fixed pCT volume and moving CBCT volume in world coordinates (considering different spatial resolutions). The voxels of the CBCT were mapped to the pCT volume, i.e. the registered CBCT volume adapted to the world coordinate system of pCT. The optimizer and metric were previously defined with the function `imregconfig`. The optimizers initial radius was set to 0.004, the maximum number of iterations was chosen to be 300. The measure of similarity (metric) was multi-modal Mutual Information [31], since the brightness ranges of the CT and CBCT were not the same. An illustration of the alignment boxes and the transformation vectors is given in Figure 2.7.

3. Back-transformation to full 3D volume after registration: The registration transformation vector $T_{CBCT \rightarrow pCT}$ of the full 3D volumes of pCT and CBCT was calculated as follows:

$$T_{CBCT \rightarrow pCT} = t_{pCT,ab} + T_{CBCT,ab \rightarrow pCT,ab} - t_{CBCT,ab} \tag{2.20}$$

Figure 2.7 demonstrates this relation between the different transformation vectors: The difference of both alignment box transformation vectors had to be added to the registration transformation vector between the two alignment boxes, determined by the provided Matlab toolkit.

4. Calculation of final registered isocenter-shift in linac coordinates: The applied isocenter shift between tumor in pCT and tumor in initial CBCT was desired to be validated by automatic registration. The function `transformPointsForward`

applied the registered translation vector $T_{CBCT \rightarrow pCT}$ on a point in the initial CBCT to determine where that point was found after registration in the coordinate system of the fixed pCT volume. The center coordinates of initial CBCT volume were required to be mapped as coordinates after CBCT registration in the coordinate system of pCT (world coordinates, pixel size, slice thickness and volume size of pCT). Figure 2.8 illustrates the center coordinates before and after registration. The resulting final isocenter shift was then the difference between the initial center of rotation and the isocenter coordinate of pCT. After conversion from Matlab to linac coordinate system, the isocenter shift determined by image registration should ideally be in accordance with the initially applied isocenter shift as listed in Table 2.2.

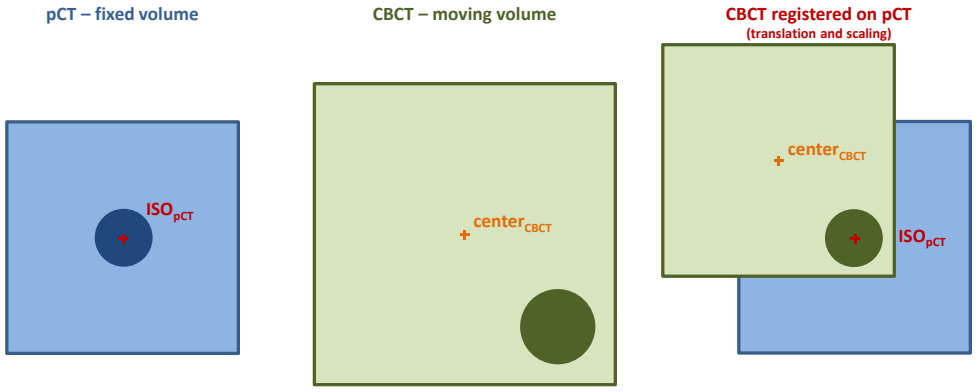

Figure 2.8: Illustration of point forward transformation to map the center of CBCT in the registered CBCT with the coordinate system of the planning CT.

5. Visualization of registered pCT and CBCT To visualize the registration result in both full 3D volume and alignment box, the transformation matrices $T_{CBCT \rightarrow pCT}$ and $T_{CBCT,ab \rightarrow pCT,ab}$, respectively, were applied linearly on the full and cropped CBCT (moving volume). This was achieved by the function `imwarp` considering the spatial information of the registered volume, which was scaled to the spatial information of the fixed pCT volume. The function `imshowpair` allowed overlapping visualization of single axial slices from both planning CT (green = fixed volume) and CBCT (magenta = moving volume) before and after registration was

possible.

Script for automatic registration of all acquired 3D volumes

A framework was developed for fully automatic registration with the Matlab toolkit for all acquired 3D CBCT volumes (kV-Chest$_1$, kV$_{180}$, MV$_{180}$ and kV-MV) for all four tumor-mimicking phantom shapes with according planning CT. This script directly wrote the resulting isocenter shifts (in consideration of differences in coordinate systems of linac and Matlab software) to an excel sheet, which was thereafter used for automatic evaluation (see section 2.5.5).

2.5.4 Measurement workflow of phantom shifts

For each tumor shape, the workflow was divided into two steps:

- **Isocenter verification:**
  The inhomogeneous thorax phantom was aligned to the markers using room lasers. A clinically approved kV-CBCT scan was performed and registered to the reference CT using XVI automatic matching (grey value method). Emerging phantom tilts were corrected and the scan was repeated until no rotational errors were detectable anymore. The remaining translational setup error was corrected using iGuide. The tumor was then in accurate isocenter position ($\pm 0.05\,$mm) and the couch vector was reset to zero.
- **Isocenter shift:**
  Based on this initial zero position, the 10 pre-defined translational shifts (Table 2.2) were applied sequentially. The iGuide software was used to monitor the relative shift of each phantom position and CBCT scans with kV$_{180}$, MV$_{180}$ and kV-MV imaging methods were acquired. The procedure was repeated for each tumor shape, including the initial isocenter verification. Thus, 4 times 30 datasets were collected.

To provide comparison with a clinically used preset, the panel position and the gantry speed were changed to kV-Chest$_1$ CBCT setup and the procedure was repeated for all tumor-mimicking shapes (4 times 10 shifts).

2.5.5 Evaluation methods

The detection error was the difference between registration result and original couch shift (Table 2.2). 36 datasets were generated, consisting of four imaging techniques, three registration methods and three translational shift directions. For automatic registrations, each dataset consisted of 40 detection error values (four tumor-shapes with 10 shifts each). Manual registration was performed by three physicians, resulting in 120 values each. Mean and standard deviation as well as maximum and minimum detection error were calculated.

Paired difference statistical test was performed between all imaging techniques. Furthermore, the same test was applied to evaluate whether there were significant differences between the three registration methods. In both cases, null hypothesis indicated zero mean of the difference between the paired samples. A significance level of 5% was chosen. To consider normal or non-normal distributed data sets for calculation of $p-$value, the *Wilcoxon Signed Rank Test* [100] was chosen instead of more common Student's t-test.

3 Results

Towards clinical implementation of novel combined kV-MV CBCT, the properties had to be distinguished and analyzed. For each aspect, comparison studies with clinically established CBCT methods were performed. In section 3.1, the results for the dosimetric aspects of the kV-MV approach are presented. The image quality is quantified in section 3.2, and the results of the registration accuracy study of kV-MV CBCT vs. other clinical CBCT methods is presented in section 3.3.

3.1 Dosimetric properties of kV-MV CBCT

The dose exposure of kV-MV CBCT was measured and compared to other clinical and non-clinical imaging methods. For proper dose determination and evaluation of different imaging modalities, such as kV-dose output at two different x-ray sources and MV-dose output, the two different ionization chambers for absorbed dose measurements were calibrated. Therefore, beam qualities of kV and MV energies were determined (section 3.1.1). To facilitate the comparison of dose exposure of different imaging modalities, the MV-dose was converted to kV-equivalent dose by considering the different relative biological effectiveness between kV and MV. A conservative ratio of 2 vs. 1 for kV vs. MV, respectively, was selected [26, 51], i.e. energy independent comparison was possible. To simulate a real patient, the dose exposures at different positions in an inhomogeneous thorax phantom were measured (section 3.1.2). Furthermore, the CT dose index was determined for future QA purposes (section 3.1.3).

3.1.1 kV and MV beam quality and dose calibration

Following the AAPM TG protocol 61 (kV-energy) [72] and the IAEA TRS 398 and AAPM TG protocol 51 (MV-energy) [3, 56], the beam qualities and corresponding calibration factors for dose measurements were determined for all presets applied in this study.

kV beam quality and calibration factors

To determine proper half-value-layers (HVL) for kV-Chest$_1$, kV-Chest$_2$ and kV contribution of kV-MV CBCT, our measured values for HVL (see Table A.1 in Appendix) were compared with six approaches (see details in section 2.3.1):

- Monoenergetic approach following Lambert-Beer-Law [49, 62]
- Quasi-monoenergetic approach: Two-Point-Interpolation method by Hill et al. [50]
- Polyenergetic approach by Bjärngard/Shackford [14]
- Polyenergetic approach by Yu et al. [106]
- Polyenergetic approach #1 by Kleinschmidt [65]
- Polyenergetic approach #2 by Kleinschmidt [65]

In Table 3.1 and Figure 3.1, the different calculation results of HVLs are listed and compared to our measured half-value-layers for all kV-presets. As can be seen in Figure 3.1, the approach from Bjärngard/Shackford [14] had the best fit to our measurement data. The goodness of the fit, represented by the R^2 value, ranged from $0.9988 - 0.9997$. Even though their study was performed on high-energy beams (MV-range), the principle of beam hardening stays the same.
Theoretically, the approach #2 from Klevenhagen [66] seemed to be convincing from the physics point of view, however the fit function did not match at all with our measurement data. More studies on the aspect of finding a proper, physically reasonable fit function would be an interesting research topic for the future.

Method:	**kV-Chest$_1$** [mm]	**kV-Chest$_2$** [mm]	**kV-MV (kV part)** [mm]
HVL measurement	7.15	7.65	5.64
interpolation (Hill et al.)	6.39	7.49	5.19
monoenergetic (Lambert-Beer)	7.03	7.61	5.67
polyenergetic (Bjärngard/ Shackford)	**7.01**	**7.63**	**5.57**
polyenergetic (Yu et al.)	7.03	7.64	5.58
polyenergetic (Kleinschmidt #1)	6.45	7.23	5.23
polyenergetic (Kleinschmidt #2)	7.08	7.65	5.65

Table 3.1: Half-Value-Layers of kV-Chest$_1$, kV-Chest$_2$ and kV contribution of kV-MV CBCT: measured and calculated values with different fit functions.

The final HVLs determined from the Bjärngard/Shackford fit function were 7.01 mmAl for kV-Chest$_1$, 7.63 mmAl for kV-Chest$_2$, and 5.57 mmAl for kV$_{180}$ and kV contribution kV-MV CBCT.

These fit function results (HVL_{BS}) not only match with our direct measurement results within 2% maximum difference, but the resulting HVLs were also consistent with common measurement values for comparable or the same kV settings.

Textbooks mention a typical range of $(1-8)$mmAl for diagnostic and superficial x-rays [49,62]. The AAPM TG61 report [72] gives a HVL range of $(0.15-6.83)$mmAl for 100 kVp and $(1.48-8.33)$mmAl for 120 kVp. Beam quality changes with age of the x-ray tube, since the target material roughens with time.
Similar measurements were presented by Song et al. [94]; they used a comparable setup and found HVLs of 6 mmAl for 100 kV and 7 mmAl for 120 kV, resulting in a 7% difference (kV$_{180}$ and kV contribution of kV-MV CBCT) and full agreement (kV-Chest$_1$) to our presets, respectively.
Hyer et al. [55] was in 5% difference agreement with $\mathrm{HVL_{Head}} = 5.9$ mmAl and our kV$_{180}$ CBCT preset. Their Chest-preset had a higher current than ours and thus their $\mathrm{HVL_{Chest}}$ was not comparable to both our kV-Chest presets.

The kV correction factors of the dosimetry formalism in equation 2.12, that were directly beam quality dependent, were extracted from the look-up-tables provided in AAPM TG report 61 [72].
The chamber response correction factor $P_{Q,cham}$ could not directly be selected because our ionization chamber was not listed. However, it is recommended [72] to choose a value from a similar, listed chamber. Thus, we chose the correction factors

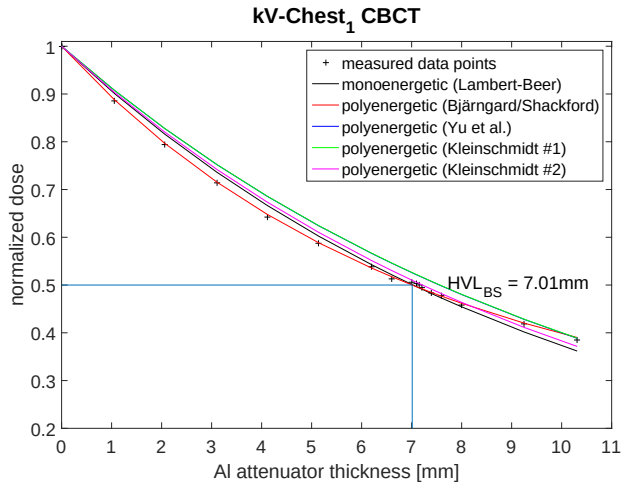

(a)

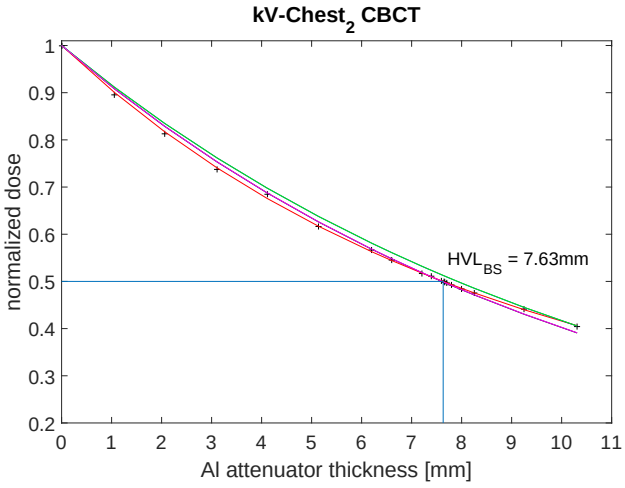

(b)

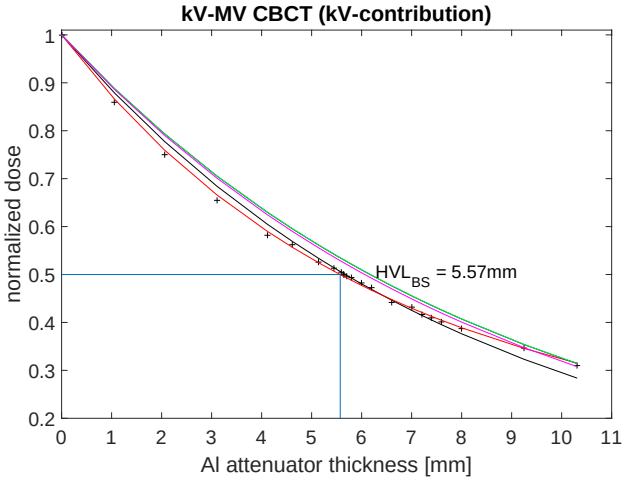

(c)

Figure 3.1: Determination of best fit for Half-Value-Layers of kV-Chest$_1$, kV-Chest$_2$ and kV contribution of kV-MV CBCT, which had the same settings as kV$_{180}$.

of Farmer chamber PTW Type 30001. With two-point-interpolation[1], the corresponding correction factors to our HVLs were extracted.
The sheath correction factor was $P_{sheath} = 1$, since our ionization chamber was waterproof, i.e. did not require an additional waterproof case. Furthermore, our measurements were not performed in water.
The conversion factor from air kerma to dose-to-water $\left[\left(\frac{\mu_{en}}{\rho}\right)^{water}_{air}\right]_{water}$ was directly taken from the look-up-table. The exact conversion factor for each HVL was determined by two-point-linear interpolation.

The final absolute dose correction factors for kV-energy range are listed in Table 3.2, separated for all kV-CBCT presets applied in this study.

	kV-Chest$_1$ CBCT	**kV-Chest$_2$ CBCT**	**kV-contribution of kV-MV, and kV$_{180}$ CBCT**
HVL	7.01 mmAl	7.63 mmAl	5.57 mmAl
$P_{Q,cham}$	1.022	1.023	1.019
P_{sheath}	1.000	1.000	1.000
$\left[\left(\frac{\mu_{en}}{\rho}\right)^{water}_{air}\right]_{water}$	1.0394	1.0417	1.0346
N_k	$8.757 \cdot 10^7$ Gy/C		

Table 3.2: Absolute dose correction factors for kV-energy range for all applied kV-imaging methods, based on AAPM TG report 61.

Other uncertainties primarily to the fact that not all phantoms consisted of water-equivalent materials were not considered. Following the AAPM TG report 61, the overall measurement uncertainty was 4.7%, including different density phantom material.

MV beam quality and calibration factors

Following the reference setup in IAEA TRS 398 [56], the beam quality index Q was determined by measuring the percentage depth dose curve of LINAC$_1$ and extracting the percentage dose values for measurement depths 20 cm and 10 cm:

$$Q = 1.2661 \cdot \frac{M_{20}}{M_{10}} - 0.0595 = 1.2661 \cdot \frac{40.0}{67.9} - 0.0595 = 0.6858 \tag{3.1}$$

[1] Two-point-interpolation mode to determine value y from corresponding value x with two neighbour points (x_1, y_1) and (x_2, y_2) : $y = y_1 + (y_2 - y1)\frac{x - x_1}{x_2 - x_1}$, with $x_1 < x < x_2$.

Figure 3.2 shows the percentage depth dose curve. The quality conversion factor k_Q was extracted from the corresponding look-up-tables for different ionization chambers and beam quality factors in IAEA TRS 398. Two-point-interpolation was applied to calculate the correct quality conversion factor. Table 3.3 lists the required calibration factor results.

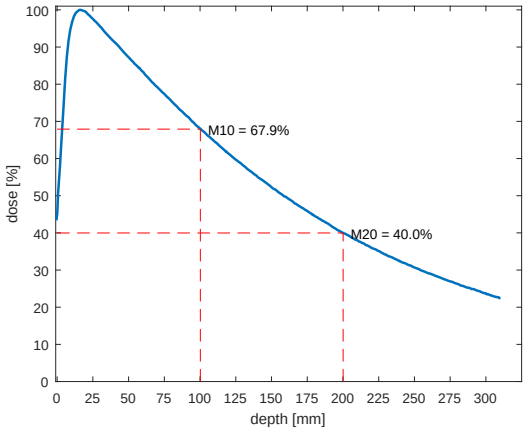

Figure 3.2: Percentage depth dose curve of 6MV linac (LINAC_1) for determination of beam quality correction factor.

Correction factors for MV energy range	
Q	0.6858
k_Q	0.9894
$N_{D,w}$	$1 \cdot 10^8\,\text{Gy/C}$

Table 3.3: Absolute dose correction factors for MV-energy range for all applied MV-imaging methods, based on IAEA TRS 398.

Dose calibration was thus provided for the MV contribution of kV-MV CBCT and the MV_{180} CBCT preset.

3.1.2 Inhomogeneous thorax phantom - patient simulation

The dose exposure to an inhomogeneous thorax phantom was measured for different imaging methods. To simulate a patient case, a target volume was defined in the lower left lung of the phantom. This tumor-position was aligned to the isocenter. Other representative dose measures were performed in the organs at risk, such as the left and right lung, the spinal cord, the body center, and the upper periphery to evaluate skin dose. Figure 3.3a shows the phantom and the evaluated positions close-up. Column 3 in Table 3.4 shows the corrected absolute dose output for the various locations (serially numbered) and imaging methods. The dose measurements of kV-MV CBCT were performed separately, because the dose responses of kV and MV behaved differently. Furthermore, the single dose contributions could be distinguished

and the different relative biological effectiveness could be considered, enabling proper dose comparison in kV range. For a complete overview, the kV and MV contributions to the kV-MV dose output are listed in columns 6 and 4, respectively. The MV dose measurement results of MV_{180} CBCT and the MV contribution of kV-MV CBCT were converted to kV-equivalent dose by halving the MV dose value[2] according to the $RBE = {}^{MV}/_{kV} = 2$. This kV-equivalent MV dose output is listed in column 5 of Table 3.4. The final absorbed dose of kV-MV CBCT in column 3 is the sum of the kV contribution and the kV-equivalent MV contribution; the unit is thus [GE].

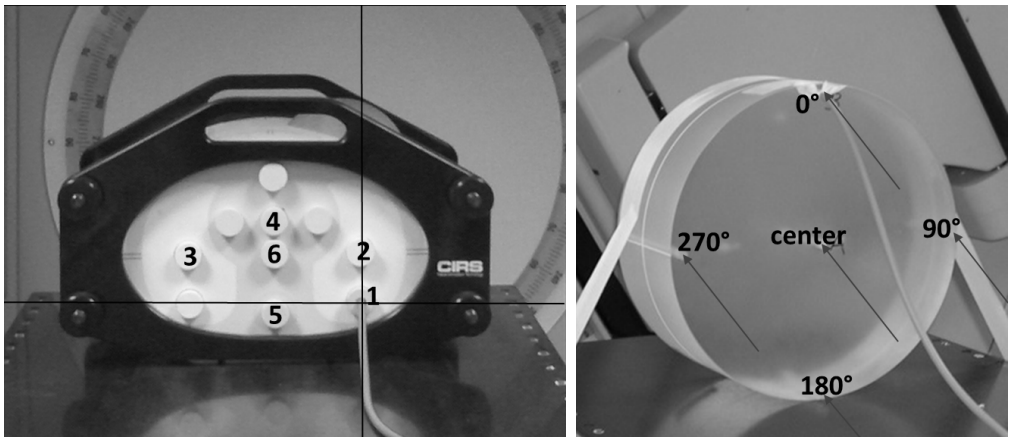

(a) **(b)**

Figure 3.3: Setup of (a) inhomogeneous thorax phantom, (b) CT dose phantom for dosimetry study.

Dose comparison of kV-MV imaging vs. conventional CBCT

Table 3.5 gives an overview of the ratios between kV-$Chest_1$ and the other imaging techniques with kV-$Chest_1$ set as fixed reference value. Table 3.6 demonstrates the ratios if kV-$Chest_2$ is the reference dose output.

Among each other, the two clinical presets, kV-$Chest_1$ and novel kV-$Chest_2$ differ mainly in the applied nominal tube current (mA) and pulse duration (ms), i.e. 1 mAs and 0.4 mAs, respectively. Furthermore, the bow-tie filter in kV-$Chest_2$ CBCT also reduces imaging dose [73]. The nominal doses provided by the manufacturer are 16 mGy and 5 mGy, respectively. The kV-$Chest_1$ preset resulted in an absolute dose

[2] The unit of kV-equivalent MV dose is Gray-equivalent [GE].

Position	CBCT	Final absorbed dose	MV part	MV part (kV-equivalent)	kV part
1: tumor-lower left lung	$kV\text{-}Chest_1$	31.26 mGy			
	$kV\text{-}Chest_2$	9.10 mGy			
	kV_{180}	0.62 mGy			
	MV_{180}	40.85 mGE	81.70 mGy	40.85 mGE	
	kV-MV	20.51 mGE	40.26 mGy	20.13 mGE	0.38 mGy
2: left lung	$kV\text{-}Chest_1$	32.00 mGy			
	$kV\text{-}Chest_2$	9.13 mGy			
	kV_{180}	0.47 mGy			
	MV_{180}	41.17 mGE	82.34 mGy	41.17 mGE	
	kV-MV	22.88 mGE	45.10 mGy	22.55 mGE	0.33 mGy
3: right lung	$kV\text{-}Chest_1$	22.85 mGy			
	$kV\text{-}Chest_2$	5.22 mGy			
	kV_{180}	0.27 mGy			
	MV_{180}	14.06 mGE	28.12 mGy	14.06 mGE	
	kV-MV	6.60 mGE	13.02 mGy	6.51 mGE	0.09 mGy
4: upper periphery	$kV\text{-}Chest_1$	23.06 mGy			
	$kV\text{-}Chest_2$	6.21 mGy			
	kV_{180}	0.25 mGy			
	MV_{180}	34.35 mGE	68.71 mGy	34.35 mGE	
	kV-MV	19.10 mGE	37.95 mGy	18.98 mGE	0.13 mGy
5: spinal cord	$kV\text{-}Chest_1$	16.45 mGy			
	$kV\text{-}Chest_2$	4.62 mGy			
	kV_{180}	0.36 mGy			
	MV_{180}	33.74 mGE	67.49 mGy	33.74 mGE	
	kV-MV	15.12 mGE	29.82 mGy	14.91 mGE	0.20 mGy
6: body center	$kV\text{-}Chest_1$	21.54 mGy			
	$kV\text{-}Chest_2$	5.96 mGy			
	kV_{180}	0.30 mGy			
	MV_{180}	33.05 mGE	66.10 mGy	33.05 mGE	
	kV-MV	17.57 mGE	34.83 mGy	17.41 mGE	0.16 mGy

Table 3.4: Determination of absorbed dose for different imaging techniques in the inhomogeneous thorax phantom (GE: Gray-equivalent with $RBE = 2$ for kV-dose distribution).

of 31.26 mGy in the tumor and 22.85 mGy in the contralateral lung. For kV-Chest$_2$, these dose values were reduced by a factor of 3-4, resulting in 9.10 mGy for the tumor region and 5.22 mGy for the organ at risk. Dose output was slightly inhomogeneously distributed around the phantom due to the fact that the phantom was positioned off-centered. The smallest dose was detected in the body center.

The kV$_{180}$ CBCT had remarkably lower dose output; measured doses were maximum $2-8\%$ of the corresponding dose values in kV-Chest$_1$ and kV-Chest$_2$. Dose output was so negligibly small compared to the others, that the asymmetric dose distribution was barely noticed.

Absorbed doses of MV$_{180}$ were maximum twice as large as the widely-used kV-Chest$_1$ CBCT preset. Due to the asymmetric dose distribution and the gantry angle moving from $-20°$ to $+170°$, the maximum dose occured in the left lung with 41.17 mGE. The tumor dose was 40.85 mGE. The smallest dose was measured in the contralateral lung: With 14.06 mGE this dose was 40% lower than in case of the clinical preset. The largest difference to the corresponding value of the clinical preset kV-Chest$_1$ was in the body center. This can be explained by the shifted dose maximum of the MV beam compared to the kV beam. Natural implications are the increasing doses with a ratio of 2.7 and 7.3% compared to the latest available kV-Chest$_1$ CBCT.

Novel kV-MV CBCT dose outputs lie in between the dose outputs of both clinical presets. Maximum dose of kV-MV CBCT was 22.88 mGE at the left lung position. Minimum dose of 6.60 mGE was exposed to the contralateral lung. This was due to asymmetric dose distribution, organs at risk could be spared. At the tumor position, dose output of the kV-MV approach was 20.5 mGE, i.e. it was 35% smaller than the kV-Chest$_1$ output and 2.2 times higher than the kV-Chest$_2$ output. The largest difference of 3.3 times the dose output of the kV-Chest$_2$ CBCT appeared at the position of body center. Compared to the kV-Chest$_1$ CBCT, however, kV-MV dose output was still 8% lower.

Comparison of MV dose measured vs. calculated (TPS)

To demonstrate the asymmetric dose distribution of kV-MV CBCT, the MV contribution was simulated in the Oncentra treatment planning system. The axial dose distribution of 4 MU equally distributed over a 100° is shown in Figure 3.4. The

Position	kV-Chest$_1$	kV-Chest$_2$		kV$_{180}$		MV$_{180}$		kV-MV	
	abs. dose	abs. dose	*ratio*	abs. dose	*ratio*	abs. dose	*ratio*	abs. dose	*ratio*
1	31.26 mGy	9.10 mGy	*0.29*	0.62 mGy	*0.02*	40.85 mGE	*1.31*	20.51 mGE	*0.66*
2	32.00 mGy	9.13 mGy	*0.29*	0.47 mGy	*0.01*	41.17 mGE	*1.29*	22.88 mGE	*0.72*
3	22.85 mGy	5.22 mGy	*0.23*	0.27 mGy	*0.01*	14.06 mGE	*0.62*	6.60 mGE	*0.29*
4	23.06 mGy	6.21 mGy	*0.27*	0.25 mGy	*0.01*	34.35 mGE	*1.49*	19.10 mGE	*0.83*
5	16.45 mGy	4.62 mGy	*0.28*	0.36 mGy	*0.02*	33.74 mGE	*2.05*	15.12 mGE	*0.92*
6	21.54 mGy	5.96 mGy	*0.28*	0.30 mGy	*0.01*	33.05 mGE	*1.53*	17.57 mGE	*0.82*

Table 3.5: Reference dose output kV-Chest$_1$: ratio between other imaging methods and reference (D/D_{ref}).

Position	kV-Chest$_2$	kV-Chest$_1$		kV$_{180}$		MV$_{180}$		kV-MV	
	abs. dose	abs. dose	*ratio*	abs. dose	*ratio*	abs. dose	*ratio*	abs. dose	*ratio*
1	9.10 mGy	31.26 mGy	*3.44*	0.62 mGy	*0.07*	40.85 mGE	*4.49*	20.51 mGE	*2.25*
2	9.13 mGy	32.00 mGy	*3.50*	0.47 mGy	*0.05*	41.17 mGE	*4.51*	22.88 mGE	*2.51*
3	5.22 mGy	22.85 mGy	*4.38*	0.27 mGy	*0.05*	14.06 mGE	*2.69*	6.60 mGE	*1.26*
4	6.21 mGy	23.06 mGy	*3.71*	0.25 mGy	*0.04*	34.35 mGE	*5.53*	19.10 mGE	*3.08*
5	4.62 mGy	16.45 mGy	*3.56*	0.36 mGy	*0.08*	33.74 mGE	*7.30*	15.12 mGE	*3.27*
6	5.96 mGy	21.54 mGy	*3.61*	0.30 mGy	*0.05*	33.05 mGE	*5.55*	17.57 mGE	*2.95*

Table 3.6: Reference dose output kV-Chest$_2$: ratio between other imaging methods and reference (D/D_{ref}).

measured and calculated MV dose outputs are listed in Table 3.7. In this comparison RBE is not considered, i.e. the originally measured absorbed dose is shown. The percentaged difference between measured and calculated MV dose values with maximum difference of 2.8% underline a proper MV dose output also in low-dose mode.

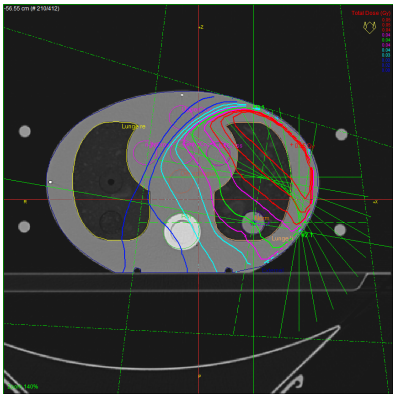

Figure 3.4: Simulation of MV-contribution of kV-MV CBCT in Treatment Planning System (Oncentra Masterplan): 4 MU delivered on a 100° gantry arc.

Position	kV-MV: MV part measured dose	kV-MV: MV part calculated dose	percentaged difference [%]
1	40.40 mGy	40.26 mGy	*0.35*
2	44.90 mGy	45.10 mGy	*0.45*
3	13.40 mGy	13.02 mGy	*2.84*
4	37.30 mGy	37.95 mGy	*1.74*
5	30.00 mGy	29.82 mGy	*0.60*
6	34.30 mGy	34.83 mGy	*1.55*

Table 3.7: MV dose output comparison between measured absolute dose [Gy] and dose calculated in a TPS (Oncentra Masterplan) by percentaged difference calculation: $diff = (D_{calc} - D_{meas})/D_{meas} \times 100$ [%].

3.1.3 CTDI quality assurance

As a standard dose value for future QA of kV-MV CBCT, the CT dose index was measured. For comparison, the CTDI was also measured for the other imaging methods, the clinical presets kV-Chest$_1$ and kV-Chest$_2$ should result in a weighted $CTDI_w$ with close agreement to the nominal dose value provided by the manufacturer (see Table 2.1).

To determine the weighted CT dose index for all imaging methods, the ionization chamber was placed at axial midpoint into the central and four periphery cavities sequentially. Figure 3.3b shows the measurement points close-up. The $CTDI_w$ was calculated following equation 2.17. The resulting dose values for each of the five measurement points as well as the final weighted CTDI are listed in Table 3.8. The MV contribution of kV-MV CBCT and MV$_{180}$ dose measurement results were converted to kV-equivalent dose by taking half of the MV dose value, similar to the previous phantom dose study 3.1.2.

CBCT	$\mathbf{CTDI_c}$	$\mathbf{CTDI_{p,0°}}$	$\mathbf{CTDI_{p,90°}}$	$\mathbf{CTDI_{p,180°}}$	$\mathbf{CTDI_{p,270°}}$	$\mathbf{CTDI_w}$
kV-Chest$_1$	9.75 mGy	22.86 mGy	20.64 mGy	20.86 mGy	28.71 mGy	**18.77** mGy
kV-Chest$_2$	3.42 mGy	6.41 mGy	6.00 mGy	5.53 mGy	6.74 mGy	**5.25** mGy
kV$_{180}$	0.17 mGy	0.05 mGy	0.58 mGy	0.78 mGy	0.46 mGy	**0.37** mGy
MV$_{180}$	29.40 mGE	29.50 mGE	24.63 mGE	28.97 mGE	9.16 mGE	**23.06** mGE
kV-MV	14.70 mGE	19.83 mGE	16.72 mGE	5.66 mGE	5.74 mGE	**11.99** mGE

Table 3.8: Determination of weighted CT Dose Index for different presets (GE: Gray-equivalent with $RBE = 2$ for kV-dose distribution).

Dose comparison of kV-MV imaging vs. conventional CBCT

Table 3.9 shows the ratios between the reference CBCT kV-Chest$_1$ and the other imaging techniques. In Table 3.10, the ratios between imaging techniques are taken considering kV-Chest$_2$ the reference CBCT.

As pointed out in section 3.1.2, among each other, the clinical presets kV-Chest$_1$ and kV-Chest$_2$ differ in tube current per pulse duration (mAs) about a factor of 3.2, which transmits to the different dose output. This difference is also seen in the comparison of $CTDI_w$: The measured weighted CT dose index for kV-Chest$_1$ is 18.77 mGy, and 5.25 mGy for kV-Chest$_2$.

With a $CTDI_w = 0.37\,\text{mGy}$, the kV_{180} has a very small average dose output with a minimum reduction of 99% and 86% compared to kV-Chest_1 and kV-Chest_2, respectively.

For MV_{180}, the $CTDI_w = 23.06\,\text{mGE}$ was 4.4 times larger than the weighted CT dose index for kV-Chest_2, but only 1.2 times larger than the $CTDI_w$ for kV-Chest_1.

The kV-MV weighted CT dose index was in between both clinical presets, with $CTDI_w = 11.99\,\text{mGE}$.

Position	kV-Chest$_1$	kV-Chest$_2$		kV$_{180}$		MV$_{180}$		kV-MV	
	abs. dose	abs. dose	*ratio*	abs. dose	*ratio*	abs. dose	*ratio*	abs. dose	*ratio*
CTDI$_c$	9.75 mGy	3.42 mGy	*0.35*	0.17 mGy	*0.02*	29.40 mGE	*3.02*	14.70 mGE	*1.51*
CTDI$_{p,0°}$	22.86 mGy	6.41 mGy	*0.28*	0.05 mGy	*0.00*	29.50 mGE	*1.29*	19.83 mGE	*0.87*
CTDI$_{p,90°}$	20.64 mGy	6.00 mGy	*0.29*	0.58 mGy	*0.03*	24.63 mGE	*1.19*	16.72 mGE	*0.81*
CTDI$_{p,180°}$	20.86 mGy	5.53 mGy	*0.27*	0.78 mGy	*0.04*	28.97 mGE	*1.39*	5.66 mGE	*0.27*
CTDI$_{p,270°}$	28.71 mGy	6.74 mGy	*0.23*	0.46 mGy	*0.02*	9.16 mGE	*0.32*	5.74 mGE	*0.20*
CTDI$_w$	18.77 mGy	5.25 mGy	*0.28*	0.37 mGy	*0.02*	23.06 mGE	*1.23*	11.99 mGE	*0.64*

Table 3.9: Reference dose output kV-Chest_1 for CTDI determination: ratio between other imaging methods and reference (D/D_{ref}).

Position	kV-Chest$_2$	kV-Chest$_1$		kV$_{180}$		MV$_{180}$		kV-MV	
	abs. dose	abs. dose	*ratio*	abs. dose	*ratio*	abs. dose	*ratio*	abs. dose	*ratio*
CTDI$_c$	3.42 mGy	9.75 mGy	*2.85*	0.17 mGy	*0.05*	29.40 mGE	*8.60*	14.70 mGE	*4.30*
CTDI$_{p,0°}$	6.41 mGy	22.86 mGy	*3.57*	0.05 mGy	*0.01*	29.50 mGE	*4.60*	19.83 mGE	*3.09*
CTDI$_{p,90°}$	6.00 mGy	20.64 mGy	*3.44*	0.58 mGy	*0.10*	24.63 mGE	*4.11*	16.72 mGE	*2.79*
CTDI$_{p,180°}$	5.53 mGy	20.86 mGy	*3.77*	0.78 mGy	*0.14*	28.97 mGE	*5.24*	5.66 mGE	*1.02*
CTDI$_{p,270°}$	6.74 mGy	28.71 mGy	*4.26*	0.46 mGy	*0.07*	9.16 mGE	*1.36*	5.74 mGE	*0.85*
CTDI$_w$	5.25 mGy	18.77 mGy	*3.58*	0.37 mGy	*0.07*	23.06 mGE	*4.39*	11.99 mGE	*2.28*

Table 3.10: Reference dose output kV-Chest_2 for CTDI determination: ratio between other imaging methods and reference (D/D_{ref}).

3.2 Image Quality of kV-MV CBCT

Sufficient image quality is essential for successful image guidance in radiotherapy. In this study, spatial resolution (section 3.2.1) and geometrical accuracy (section 3.2.2) were evaluated for kV-MV CBCT and compared with clinical and non-clinical CBCT alternatives.

3.2.1 CatPhan - spatial resolution

The CatPhan phantom [2] is the most widely-used image quality assurance phantom for CBCT. The high resolution module was scanned by kV-MV CBCT and clinical kV-Chest$_1$ CBCT, to evaluate clinical feasibility of kV-MV compared to a clinically established imaging method. Figures 3.5a and 3.5b show the weighted central phantom slices of the spatial resolution module, highlighting the highest number of line pair discrimination for kV-Chest$_1$ and kV-MV CBCT, respectively. For both kV-MV and kV-Chest$_1$, the line pairs in the third insert were still resolvable. Figures 3.5c and 3.5d display a line profile through the third line pair for kV-Chest$_1$ and kV-MV CBCT, respectively.

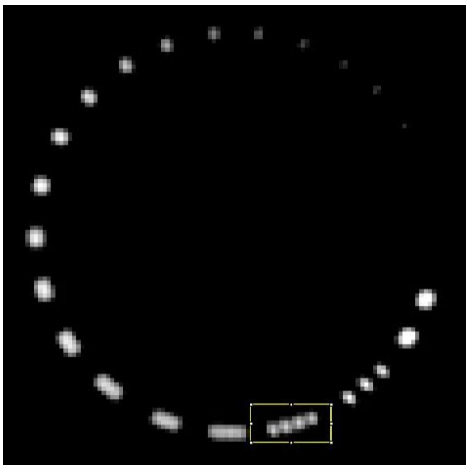

(a) CatPhan phantom scan in spatial resolution module with kV-Chest$_1$ CBCT.

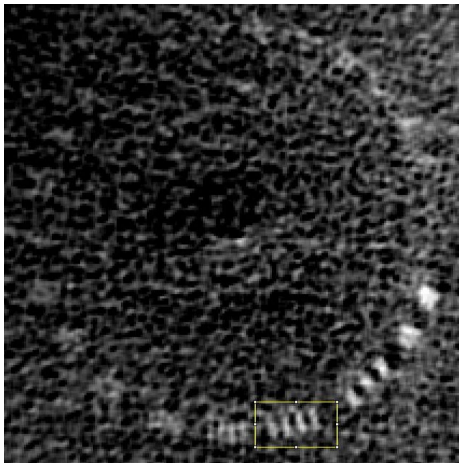

(b) CatPhan phantom scan in spatial resolution module with kV-MV CBCT.

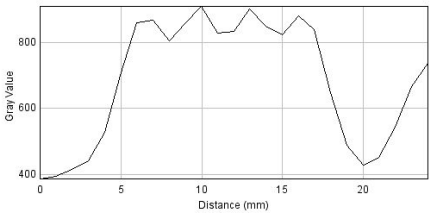

(c) Profile through third line pair for spatial resolution analysis with kV-Chest$_1$ CBCT.

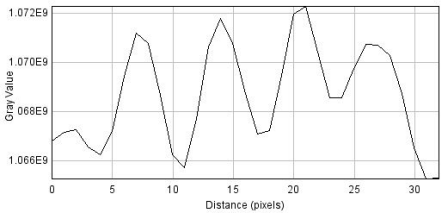

(d) Profile through third line pair for spatial resolution analysis with kV-MV CBCT.

Figure 3.5: Evaluation of spatial resolution with the CatPhan phantom for kV-Chest$_1$ and kV-MV CBCT.

3.2.2 Inhomogeneous thorax phantom - tumor-shape diameter

Geometrical accuracy of kV-MV CBCT was evaluated by determining the diameters of the four different tumor-mimicking shapes inserted in the inhomogeneous thorax phantom. For comparison, geometrical accuracy was also determined for kV-Chest$_1$, kV$_{180}$ and MV$_{180}$. The diameters of the different tumor-inlays were measured by manually drawing random line profiles through the tumor-mimicking shapes in each acquired CBCT volume in Matlab and ImageJ, for both body and spikes. Each diameter was measured three times to determine statistical deviation. Table 3.11 shows the results of diameter determination. Figures 3.6a to 3.6d show the diameter measurement of each tumor-shaped inlay scanned with kV-MV CBCT.

		body diameter [mm]	**spikes diameter [mm]**
Ball	**nominal size**	**15.0**	
	kV-MV	15.5 ± 0.8	
	kV-Chest$_1$	15.3 ± 0.8	
	kV$_{180}$	15.5 ± 0.4	
	MV$_{180}$	14.7 ± 0.6	
Cylinder	**nominal size**	**6.0**	**3.0**
	kV-MV	7.0 ± 0.4	3.3 ± 0.6
	kV-Chest$_1$	6.7 ± 0.5	3.7 ± 0.5
	kV$_{180}$	7.2 ± 0.2	3.0 ± 0.4
	MV$_{180}$	8.0 ± 0.7	4.0 ± 0.4
Star10	**nominal size**	**10.0**	**5.0**
	kV-MV	10.2 ± 0.6	5.3 ± 1.0
	kV-Chest$_1$	10.7 ± 0.9	5.3 ± 0.5
	kV$_{180}$	10.2 ± 0.6	4.8 ± 0.2
	MV$_{180}$	10.2 ± 0.6	5.8 ± 1.0
Star15	**nominal size**	**15.0**	**3.0**
	kV-MV	14.8 ± 0.2	3.3 ± 0.5
	kV-Chest$_1$	15.3 ± 0.5	3.7 ± 0.5
	kV$_{180}$	15.8 ± 0.6	3.0 ± 0.4
	MV$_{180}$	16.5 ± 0.4	3.8 ± 0.9
mean difference	kV-MV	-0.4 ± 0.7	-0.3 ± 0.7
	kV-Chest$_1$	-0.5 ± 0.6	-0.6 ± 0.5
	kV$_{180}$	-0.7 ± 0.6	0.1 ± 0.4
	MV$_{180}$	-0.8 ± 1.1	-0.9 ± 0.8

Table 3.11: Geometrical accuracy determination of kV-MV CBCT by diameter measurement of four different tumor-mimicking inlays with kV-MV CBCT and other clinical and non-clinical CBCT presets.

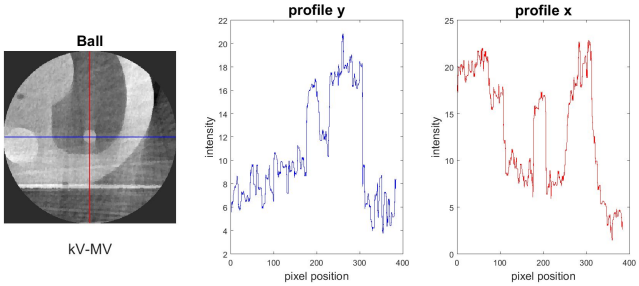

(a) Ball-shaped tumor-mimicking inlay.

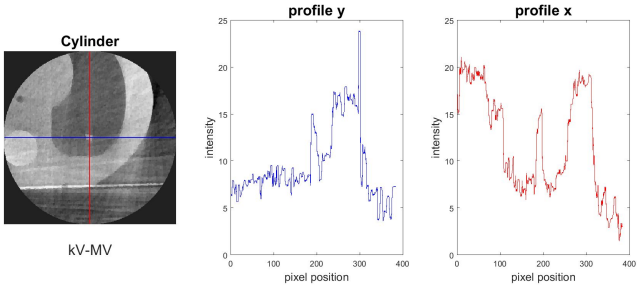

(b) Cylinder-shaped tumor-mimicking inlay.

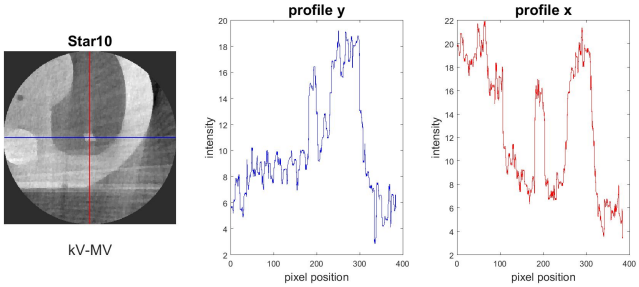

(c) Small star-shaped tumor-mimicking inlay.

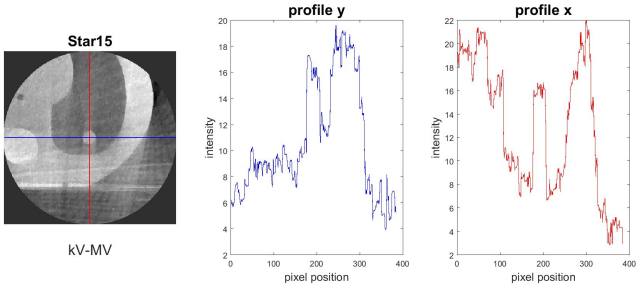

(d) Large star-shaped tumor-mimicking inlay.

Figure 3.6: Geometrical accuracy determination of kV-MV CBCT by profile analysis through differently-shaped tumor-mimicking inlays.

3.3 Registration Accuracy of kV-MV CBCT

Registration accuracy of kV-MV was evaluated and compared to conventional, clinically established CBCT methods. Therefore, the inhomogeneous thorax phantom (static position) was scanned with four imaging techniques (clinical kV-Chest$_1$, non-clinical kV$_{180}$ and MV$_{180}$, as well as kV-MV), for four tumor-mimicking shapes with 10 isocenter shifts each (conducted by the same experimenter), resulting in a total of 160 datasets. To save measurement time, kV$_{180}$, MV$_{180}$ and kV-MV CBCT were acquired simultaneously. The corresponding projections were each reconstructed with our in-house developed FDK reconstruction software [18]. To reduce the influence of MV cross-scatter expected on the kV-detector, a filter was applied on the reconstructed 3D volume data sets. Tests of different filters, including common median filter, showed that a 3-dimensional *Kuwahara filter* [69] was the most suitable, since it reduced noise but preserved edges.

3.3.1 Qualitative evaluation of registration accuracy

Figures 3.7a, 3.7b, 3.8a and 3.8b show the CBCT scans of each tumor shape for different imaging techniques in a representative axial slice. In line 1, the full phantom reconstruction is shown and in line 2, the full phantom CBCT is overlaid with the planning CT after successful registration of shift 1 with self-developed registration method (in-house). Line 3 and 4 display the enlarged tumor regions of line 1 and 2.

3.3.2 Quantitative evaluation of registration accuracy

The Box-and-Whisker-diagrams in Figure 3.9 give an overview of detection error distributions, separated for different imaging techniques, registration methods and translational directions. The results of the three registration methods followed the same trend. Both automatic registration results validated the objective performance of manual registration by the clinical experts.

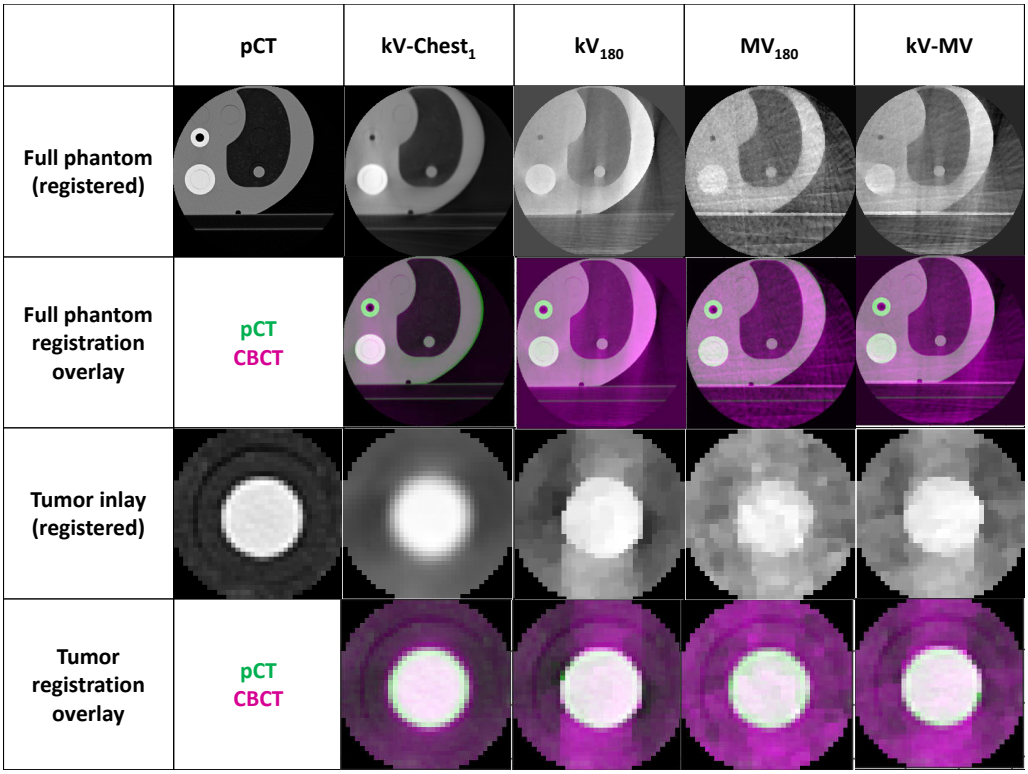

(a) Ball-shaped tumor-inlay.

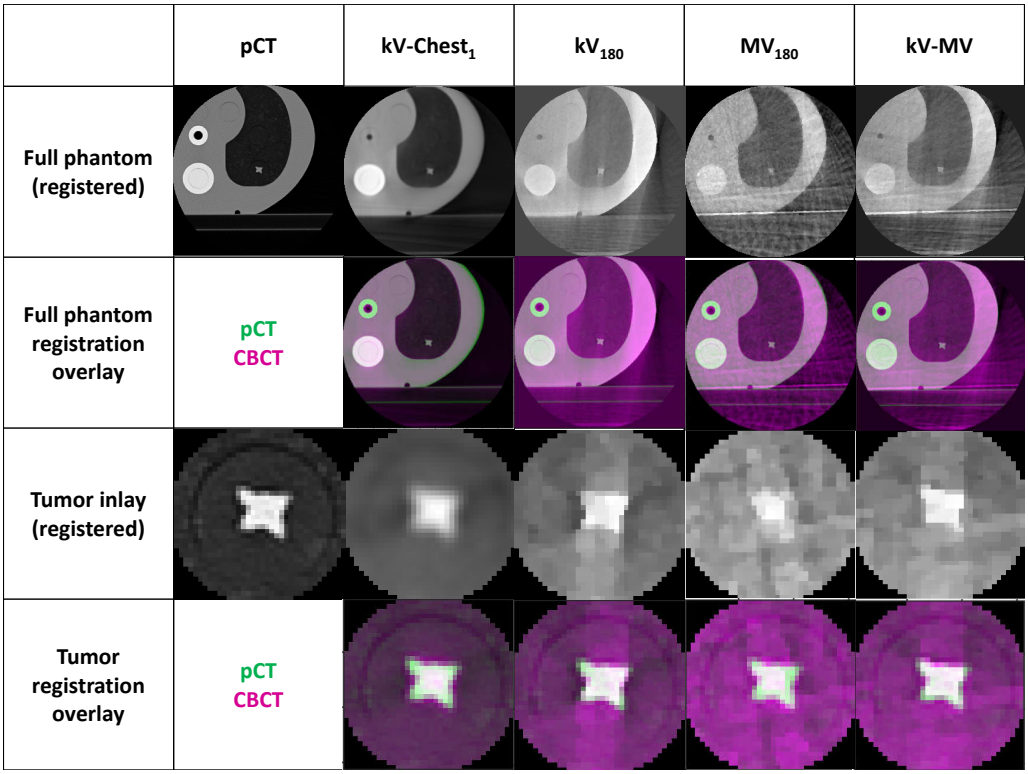

(b) Cylinder-shaped tumor-inlay.

Figure 3.7: Registration results (automatic in-house method) for all imaging techniques; kV_{180}, MV_{180} and kV-MV CBCT projection data were acquired simultaneously.

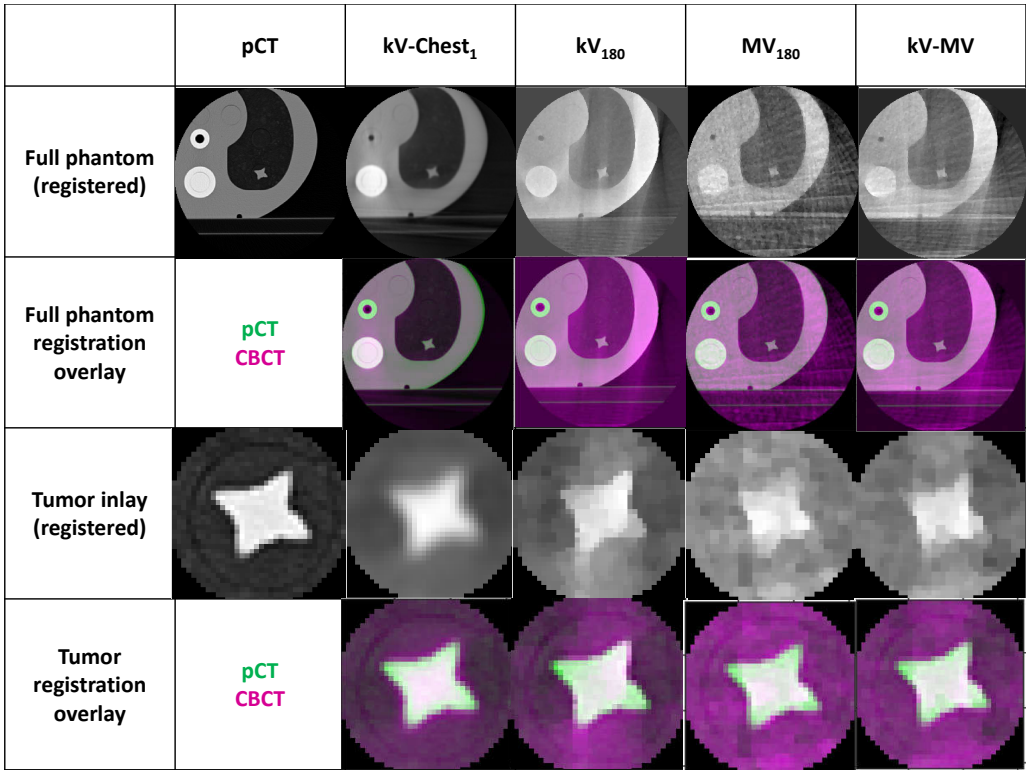

(a) Small star-shaped tumor-inlay.

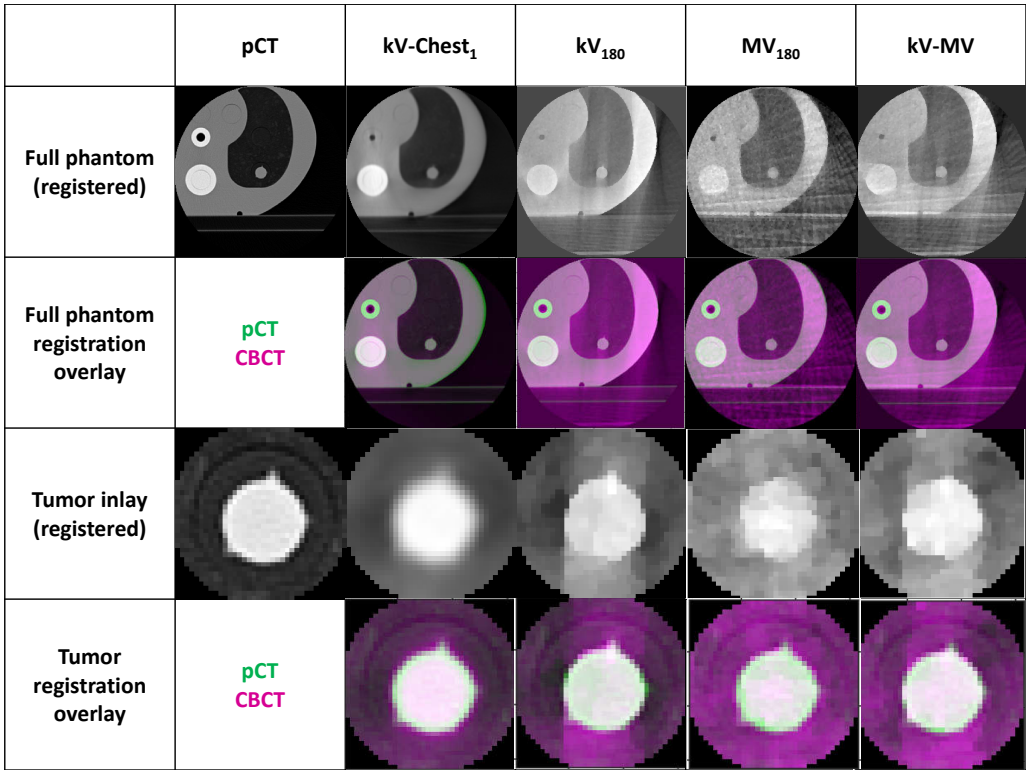

(b) Large star-shaped tumor-inlay.

Figure 3.8: Registration results (automatic in-house method) for all imaging techniques; kV_{180}, MV_{180} and kV-MV CBCT projection data were acquired simultaneously.

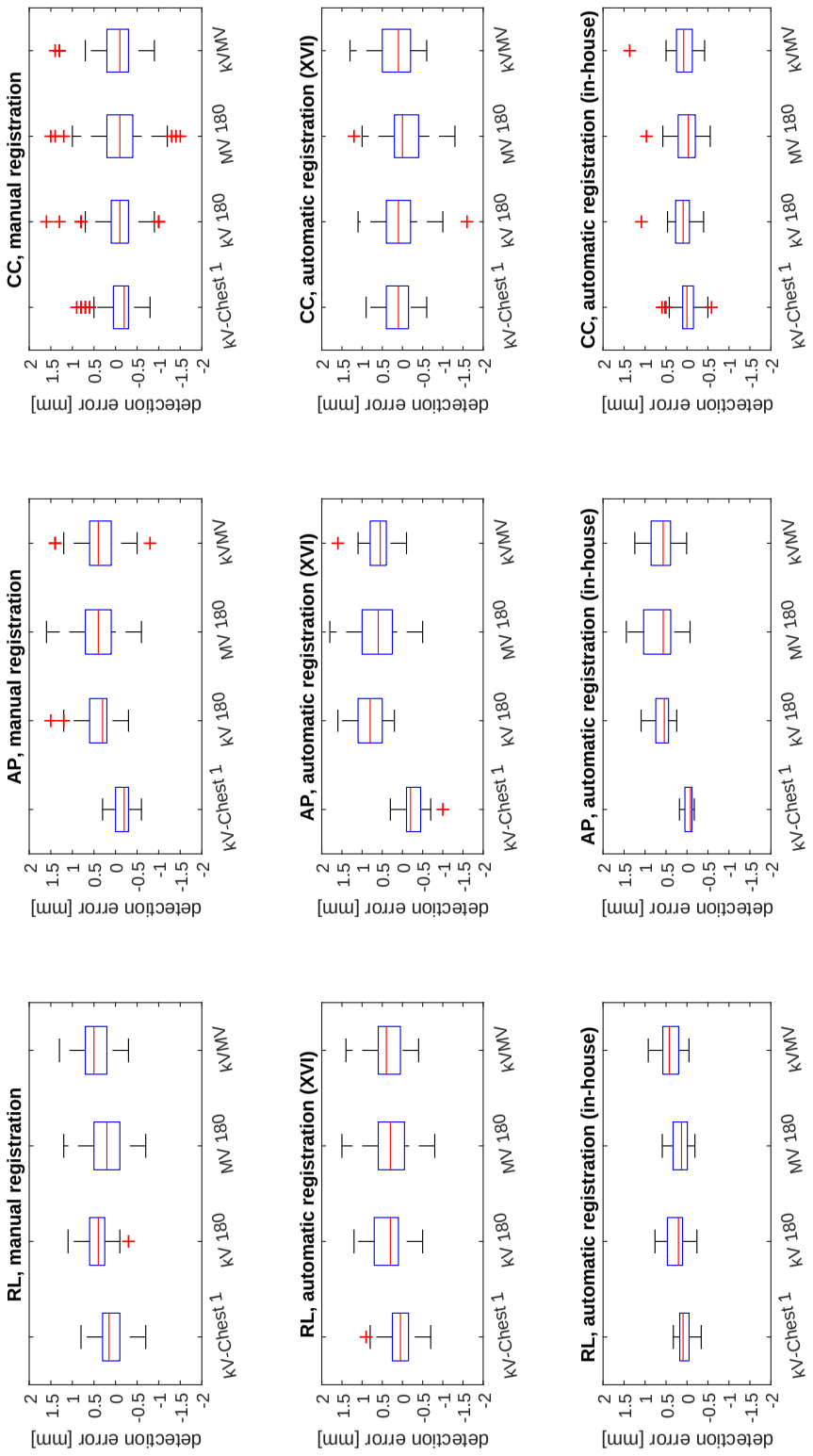

Figure 3.9: Registration of all inlays in RL, AP and CC direction for different imaging techniques and registration methods (line 1: manual registration, line 2: automatic registration (XVI), line 3: automatic registration (in-house)).

Table 3.12 shows the corresponding mean detection errors (± standard deviation) as well as the maximum and minimum values. There were only minor deviations (maximum difference 0.1 mm) between mean and median of each dataset.

mean ± standard deviation detection error					
CBCT		**kV-Chest$_1$**	**kV$_{180}$**	**MV$_{180}$**	**kV-MV**
manual registration	**RL [mm]**	0.1 ± 0.3	0.4 ± 0.3	0.2 ± 0.4	0.5 ± 0.3
	AP [mm]	-0.2 ± 0.2	0.4 ± 0.4	0.4 ± 0.5	0.4 ± 0.4
	CC [mm]	-0.1 ± 0.3	-0.1 ± 0.4	-0.1 ± 0.5	0.0 ± 0.4
automatic registration (XVI)	**RL [mm]**	0.0 ± 0.4	0.4 ± 0.4	0.3 ± 0.5	0.4 ± 0.4
	AP [mm]	-0.2 ± 0.3	0.8 ± 0.4	0.6 ± 0.5	0.6 ± 0.3
	CC [mm]	0.1 ± 0.4	0.1 ± 0.5	-0.1 ± 0.5	0.2 ± 0.5
automatic registration (in-house)	**RL [mm]**	0.1 ± 0.2	0.3 ± 0.2	0.2 ± 0.2	0.4 ± 0.2
	AP [mm]	0.0 ± 0.1	0.6 ± 0.2	0.7 ± 0.4	0.6 ± 0.3
	CC [mm]	0.0 ± 0.3	0.1 ± 0.3	0.0 ± 0.3	0.1 ± 0.3
maximum / minimum detection error					
CBCT		**kV-Chest$_1$**	**kV$_{180}$**	**MV$_{180}$**	**kV-MV**
manual registration	**RL [mm]**	$0.8/-0.7$	$1.1/-0.3$	$1.2/-0.7$	$1.3/-0.3$
	AP [mm]	$0.3/-0.6$	$1.5/-0.3$	$1.6/-0.6$	$1.4/-0.4$
	CC [mm]	$0.9/-0.8$	$1.6/-1.0$	$1.5/-1.5$	$1.4/-0.9$
automatic registration (XVI)	**RL [mm]**	$0.9/-0.7$	$1.2/-0.5$	$1.5/-0.8$	$1.4/-0.4$
	AP [mm]	$0.3/-1.0$	$1.6/\ \ 0.2$	$1.8/-0.5$	$1.6/-0.1$
	CC [mm]	$0.9/-0.6$	$1.1/-1.6$	$1.2/-1.3$	$1.3/-0.6$
automatic registration (in-house)	**RL [mm]**	$0.3/-0.3$	$0.8/-0.2$	$0.6/-0.2$	$0.9/\ \ 0.0$
	AP [mm]	$0.2/-0.2$	$1.1/\ \ 0.2$	$1.4/-0.1$	$1.2/\ \ 0.0$
	CC [mm]	$0.6/-0.6$	$1.1/-0.4$	$1.0/-0.6$	$1.4/-0.4$

Table 3.12: Detection errors for different imaging techniques and registration methods, representing the average of four tumor-inlays and 10 isocenter shifts as well as corresponding maximum and minimum detection errors.

Averaged over all registration methods, kV-MV CBCT detection errors were (0.4 ± 0.3) mm in RL, (0.5 ± 0.3) mm in AP and (0.1 ± 0.4) mm in CC direction. Maximum detection errors were 1.4 mm (RL and CC) and 1.6 mm (AP), whereas maximum RL and AP offset were detected with automatic registration method (XVI), maximum CC error with automatic registration (in-house). In comparison, clinical kV-Chest$_1$ CBCT detection errors were (0.1 ± 0.3) mm in RL, (-0.1 ± 0.2) mm in AP and (0.0 ± 0.1) mm in CC direction, with maximum detection errors of 0.9 mm in RL and CC direction, and 0.3 mm in AP.

Overall maximum detection errors were distinguished in automatic registration (XVI) method of MV$_{180}$ CBCT for RL (1.5 mm) and AP (1.8 mm) direction. In CC direction, MV$_{180}$ CBCT closely followed the largest offset of kV$_{180}$ CBCT with 1.2 mm.

3.3.3 Significance-Test between different imaging techniques and registration methods

With the *Kolmogorov-Smirnov test* [75] provided in Matlab, all measurement datasets were tested negatively for normal distribution. Thus, the choice of *paired difference test* from *Wilcoxon* [100] was justified.

As shown in Table 3.13, the paired difference test between kV-MV and kV-Chest$_1$ CBCT confirmed a significant offset in RL and AP direction ($p < 0.01$), since kV-MV had a detection error bias of up to ± 0.5 mm. In CC direction, differences were not significant ($p = 0.33 - 0.81$). Comparison between kV-MV and kV$_{180}$ as well as MV$_{180}$ showed mostly no significant differences, since all three imaging techniques suffered from image degradation for similar reasons.

		kV-Chest$_1$ vs. kV-MV	**kV$_{180}$ vs. kV-MV**	**MV$_{180}$ vs. kV-MV**
manual registration	**RL**	**< 0.001**	**< 0.001**	**< 0.001**
	AP	**< 0.001**	0.783	0.451
	CC	0.809	0.551	0.277
automatic registration (XVI)	**RL**	**0.004**	0.806	0.240
	AP	**< 0.001**	**0.006**	0.868
	CC	0.805	0.554	**0.004**
automatic registration (in-house)	**RL**	**< 0.001**	**< 0.001**	**< 0.001**
	AP	**< 0.001**	0.767	0.183
	CC	0.333	0.485	**0.002**

Table 3.13: P-values determined with paired difference test between kV-MV and other imaging techniques

The second paired difference test (Table 3.14) showed significant advantage of manual vs. both automatic registration methods ($p < 0.05$) for the major imaging techniques kV-MV and kV-Chest$_1$ CBCT. This is because manual registration detection error results were closest to zero, followed by in-house registration. For automatic registration (XVI), detection errors were spread out widest.

direction	***CBCT***	**manual vs. automatic (XVI) registration**	**manual vs. automatic (in-house) registration**	**automatic registration: XVI vs. in-house**
RL	kV – Chest$_1$	**0.023**	**< 0.001**	0.840
	kV – MV	**0.036**	**0.001**	0.872
AP	kV – Chest$_1$	0.198	**< 0.001**	**< 0.001**
	kV – MV	**0.001**	**< 0.001**	0.747
CC	kV – Chest$_1$	**0.003**	0.076	**0.014**
	kV – MV	**0.005**	**0.003**	0.216

Table 3.14: P-values determined with paired difference test between all three registration methods for clincal kV-Chest$_1$ and novel kV-MV CBCT

4 Discussion and Conclusion

In-house developed ultrafast combined kV-MV CBCT was recently successfully established and the workflow is fully automated [15, 17]. Enabling image times of only 15 s is a very promising alternative for DIBH- patients suffering from lung cancer [23].

Clinical CBCT acquisition takes at least 30 s, since 180° gantry rotation is a minimum requirement for sufficient image registration, and the gantry speed is limited to 1 rpm by law. In 2014, Zhong et al. [107] implemented and evaluated single-breath-hold CBCT and evaluated it based on patient studies. In their study, however, the single-breath-hold time was limited to minimum 40 s. Following McNair et al. [77], imaging times of 30 s or more limit the applicability of imaging within single breath-hold to a small percentage of patients. Their recommended achievable breath-hold time for patients with non-small cell lung cancer was 15 s. Thus, for most patients, imaging with the fastest achievable imaging technique requires minimum one imaging interruption for free breathing. Total imaging time is increased to minimum 40 s.

A possible improvement from 30 s to 15 s makes thus a significant difference for a fair percentage of the lung cancer population. With a fast imaging technique of data acquisition within single-breath-hold, not only the patient comfort could be improved and the treatment delivery chain accelerated, but also potential image quality degradation and repositioning inaccuracies due to residual or intrafractional breathing motion could be prevented. It is therefore aspired to implement combined kV-MV CBCT into clinical routine.

For legal approval however, clinical feasibility of kV-MV CBCT has to be investigated. The aim of this thesis was to develop concepts to evaluate the properties of kV-MV CBCT, to accomplish the phantom measurements and to evaluate and compare the results with conventional, clinical and non-clinical imaging techniques. This

thesis focused on the following clinically required qualities of image guidance systems: (1) dosimetry, (2) image quality and (3) registration accuracy. In the following subsections, the accomplished results are discussed for each kV-MV CBCT property.

4.1 Dosimetric properties of kV-MV CBCT

The major concern of the novel approach of kV-MV CBCT is the dose exposure to the patient. Most commonly, image guidance is performed with kV-CBCT. The MV-contribution of kV-MV CBCT could thus be a critical dosimetric issue towards clinical implementation. Dosimetric properties of kV-MV CBCT were evaluated and compared with other clinical (kV-Chest$_1$, kV-Chest$_2$) and non-clinical (kV$_{180}$, MV$_{180}$) imaging techniques.

4.1.1 Optimal dose calibration

For proper and reliable dosimetry, the ionization chambers had to be calibrated. Two point-dose ionization chambers of the same type were applied, one was calibrated on air kerma (kV-range), the other one on absorbed dose-to-water (MV-range), to perform appropriate dosimetry for kV and MV contributions in the measurement studies. Beam qualities of kV and MV energies were determined. Half value layer measurements as specification of kV beam quality were performed for all kVp and mAs combinations applied in this study. Extensive research was performed to find an appropriate fit for measurement values, considering the beam hardening effect. The method of Bjärngard/Shackford [14] resulted in a proper fit to our HVL measurement data and thus their mathematical approach was used to calculate the HVL for our imaging techniques with kV contribution. The resulting HVLs were in accordance with literature. MV beam quality index was determined by measuring a percentage depth dose curve with a water tank. In the treatment planning system of our clinic, a quality index of $Q = 0.68$ is used in case of the 6MV linac output. LINAC$_1$ was calibrated accordingly. Our measurement of Q showed a deviation of less than 1%.

To compare both kV and MV dose output with each other, MV dose was converted to kV-equivalent dose. Following recommendations in literature, as discussed in section

2.3.3, a conservative relative biological effective conversion ratio of 2 vs. 1 was chosen for kV vs. MV dose, respectively. Thus, the dose output of the MV contribution of kV-MV CBCT and MV_{180} CBCT was halved. To distinguish between measured MV dose and kV-equivalent MV dose, the unit of kV-equivalent MV dose was adapted to Gray-equivalent [GE].

4.1.2 Dose exposure of kV-MV CBCT

The dose exposure of kV-MV CBCT was evaluated with regard to two different aspects. First, dose measurements were performed in an inhomogeneous thorax phantom (CIRS) to simulate a patient case. Dose output was measured in six representative body sites, such as the target location in the lower left lung, both lungs, spinal cord, body center and upper periphery. Second, a CT Dose Index (CTDI) was determined as standard dose value for future quality assurance.

In the inhomogeneous thorax phantom, kV-MV CBCT dose as the sum of kV contribution and kV-equivalent MV contribution, varied from $6.60 - 22.88\,\mathrm{mGE}$. The difference in dose values is due to the asymmetric dose distribution arising from the limited gantry angle rotation of combined 90° kV and 90° MV beam. The maximum dose was measured at the left lung, which was at the location where the kV and MV contributions overlapped (90° gantry angle position). Due to the asymmetric dose distribution, healthy tissue could be spared; the minimum dose was measured in the contralateral lung.

The determined weighted CT dose index was $11.99\,\mathrm{mGE}$ for kV-MV CBCT. In this homogeneous phantom, the asymmetric dose property of kV-MV is clearly demonstrated: highest dose output is detected at $0 - 90°$, this is where the MV-contribution was highest. The lowest dose output was measured in the contralateral cavities, at $180 - 270°$ gantry angles. The central cavity showed a rather large measure. This is because MV beams travel farther than kV beams.

4.1.3 Comparison of all applied imaging techniques, including kV-MV

For both phantom studies, the novel kV-MV CBCT dose output was compared with two clinically established CBCTs, kV-Chest$_1$ and kV-Chest$_2$. To allow comparison to fastest-achievable conventional monoenergetic CBCT, the dose output of kV$_{180}$ and MV$_{180}$ CBCT was also measured.

Averaged over all measurement points, the ratio between the widely-used kV-Chest$_1$ and the latest available kV-Chest$_2$ CBCT was 3.6, i.e. both thorax phantom and CTDI measurements are in agreement with the nominal dose ratio of 3.2 provided by the manufacturer. The measured $CTDI_w$ of the kV-Chest$_1$ preset was 18.77 mGy, thus approximately 15% higher than the nominal dose of 16 mGy. Following the manufacturer, a dose deviation of ±35% is still within the limits [37]. The deviation to the nominal dose value of kV-Chest$_1$ could be related to the advanced age of the x-ray tube of LINAC$_1$ (installation: 2010).

The dose output of kV$_{180}$ was significantly smaller ($92-98\%$) than both clinical presets. This remarkable dose reduction is due to the bisection of angle rotation, the reduced kVp (100 kVp vs. 120 kVp of clinical presets) as well as the immense reduction of mAs (see details in Table 2.1).

A major concern in dosimetry is MV CBCT. With the development of combined kV-MV CBCT, also low-dose MV$_{180}$ CBCT could have potential for future clinical application due to metal artifact reduction, and was thus included in this comparison study. In our dosimetry studies, maximum kV-equivalent MV dose output was 41.17 mGE. This was maximum twice as large as the widely-used clinical kV-Chest$_1$ preset. Remarkable, however, was the dose reduction in the contralateral lung compared to kV-Chest$_1$. This could be explained by the asymmetric arrangement of the phantom relative to the isocenter, i.e. the contralateral lung was only irradiated indirectly by the MV beam. Especially for MV$_{180}$ CBCT an enlarged central body dose was observed compared to kV-Chest$_1$ and kV-Chest$_2$.

The kV-MV CBCT dose output and clinical kV-Chest$_1$ were in a comparable range (66% to 92%) in most positions. Special attention has to be given to the healthy right lung, where the dose was 2/3 lower than the clinical preset. Thus, the healthy

tissue could be even spared, although this was not expected in advance. Compared to latest available kV-Chest$_2$, the kV-MV CBCT dose is maximum 3.3 times higher. This dose value of 15.12 mGE occured at the body center and is close to what was measured for the kV-Chest$_1$ preset (16.45 mGy). The minimum kV-MV dose was measured in the contralateral lung where the dose was almost the same as for the kV-Chest$_2$ preset. In case of the kV-Chest$_1$ preset, the dose was even more than 3 times higher compared to the dose of the kV-MV approach.

4.1.4 Imaging dose in the clinical context

In the last decade, many studies on kV dosimetry with CBCT in particular were published [12, 80]. Most of them performed dose measurements with the clinical presets provided by the manufacturers. They either measured the CTDI [4, 94], or tried to estimate imaging dose to the patient either by phantom measurements [32, 59] or Monte Carlo simulations [33, 63].

The clinical CBCT presets kV-Chest$_1$ and kV-Chest$_2$ are in close agreement with literature and so is consequently kV-MV CBCT.

Another yet theoretical approach to combine kV and MV imaging was performed by Liu et al in 2015 [71]. Their approach is promising regarding MV to kV grey value conversion for acceptable image quality. Their high imaging doses of $50-200$ cGy, however, make a clinical implementation impossible at this stage of research.

In rare cases, MV CBCT is applied in clinical routine. Pouliot et al. [85] published a dosimetry study performed on a Siemens Primus linac with integrated MV CBCT. They reduced the dose pulse rate to 0.01 MU/°, however their dose measure over a 180° gantry arc was still $50-150$ mGy and thus had to be considered in the total dose to the patient by adding the dose to the treatment plan.
In 2015, Liu et al. [71] published a paper about MV-CT installed on a Hi-Art Tomotherapy unit. After detuning the incident electron beam from 6MV to 3.5MV in imaging mode, the weighted CT dose index was in the range of 20 mGy.

The low-dose MV CBCT approach provided by our development of combined kV-MV CBCT could be an alternative in case of metal body components close to the target location. MV dose could reduce occuring metal artifacts [87].

Considering the build-up effect in case of high energies which leads to reduced dose on the surface for MV energy, combined kV-MV imaging could also reduce dose exposure to sensitive patient skin.

The last but yet most important aspect of the dosimetric properties of kV-MV CBCT is, that determined imaging doses of approximately 22 mGE remain negligibly small compared to the prescribed dose of the treatment plan. Especially for hypofractionated SABR, fractional doses of $5-20$ Gy are common in clinical routine.

4.2 Image Quality of kV-MV CBCT

The essential prerequisite for successful image registration for patient positioning prior to radiation treatment is sufficient image quality. To investigate clinical feasibility of novel kV-MV CBCT, the spatial resolution and geometrical accuracy was evaluated and compared to the clinically established kV-Chest$_1$ CBCT.

4.2.1 Spatial resolution

The spatial resolution of novel kV-MV CBCT is in agreement with the clinically established kV-Chest$_1$ CBCT. By visual judgment, both imaging methods showed clear discrimination up to the third line pair. Since the gap between the single rods was 1.67mm, the peak to peak spatial resolution of both kV-MV and kV-Chest$_1$ resulted in 3.34mm.

Other studies published on spatial resolution of CBCT presets [105] are not comparable to our investigation, since they analyze the spatial resolution of presets especially generated for quality assurance, and not clinical presets. Thus, our novel kV-MV CBCT approach could only be compared to the direct alternative clinical kV-Chest$_1$ preset.

4.2.2 Geometrical accuracy

Geometrical accuracy of kV-MV CBCT was determined and compared with clinical and non-clinical CBCT methods by measuring the diameter of four different tumor-

mimicking shapes in the inhomogeneous thorax phantom. Manual evaluation by linear profiles resulted in a mean deviation of (-0.4 ± 0.7)mm for the body and (-0.3 ± 0.7)mm for the spikes between nominal size provided by the manufacturer and kV-MV CBCT, whereas the mean deviation for kV-Chest$_1$ was (-0.5 ± 0.6)mm (body) and (-0.6 ± 0.5)mm (spikes). The maximum deviation for the body was 1.5mm and 2.0mm for kV-MV CBCT and kV-Chest$_1$, respectively.
The non-clinical CBCT presets, kV$_{180}$ and MV$_{180}$, had a larger mean deviation of (-0.7 ± 0.6)mm (body), (0.1 ± 0.4)mm (spikes) and (-0.8 ± 1.1)mm (body), (-0.9 ± 0.8)mm (spikes), respectively. This is due to the degraded image quality, further discussed in section 4.3.3 in the registration accuracy study. For kV$_{180}$, a projection-overlap artifact of reduced edge sharpness was detected in anterior-posterior direction due to the additional cone-angle. MV$_{180}$ suffered from aliasing artifacts due to strong undersampling, as well as poor MV soft-tissue contrast [87]. MV-cross-scatter in kV-MV CBCT however did not lead to image quality degradation in terms of inaccurate geometry, as was also evaluated in 2007 by Nakagawa et al. [81].

Overall, kV-MV CBCT is conform with the image quality of the clinical kV-Chest$_1$ in high contrast areas as it is the case for a lung tumor. It can thus be concluded that kV-MV CBCT has sufficient image quality to be implemented into clinical routine.

4.3 Registration Accuracy of kV-MV CBCT

The registration accuracy of our in-house developed combined kV-MV CBCT imaging technique, allowing image acquisition within one breath-hold, was determined. To guarantee accurate patient imaging and repositioning under clinical conditions, kV-MV CBCT was compared to a conventional, clinically established technique (kV-Chest$_1$) as well as non-clinical fastest-achievable monoenergetic CBCTs (kV$_{180}$ and low-dose MV$_{180}$) in a pre-clinical study.

In this study, static phantom measurements were performed; in-between breathing phases and potential repositioning inaccuracies were not considered.

4.3.1 Optimal registration method

An advantage of manual registration over automatic approaches is to overcome possible mismatching or trapping in local minima during the automatic matching process. To also provide objective validation of manual matches by three clinical experts, two automatic registration methods were additionally applied: (1) with XVI CBCT software and (2) with self-developed rigid registration framework in Matlab (called "in-house" in this study).
In contrast to the automatic registration (XVI) method, the self-developed automatic registration method provided objective comparison between the different imaging techniques. While XVI requires manual setting of an alignment box for each registration, the self-developed framework enabled automatic registration of all datasets without manual interaction. Furthermore, the self-developed framework assured the same alignment box per isocenter shift for all imaging methods, which is a prerequisite for proper objective comparison.
All three methods resulted in mean displacement errors between $(0.0 - 0.8)\,\mathrm{mm}$, which is the currently achievable precision with volume imaging in clinical routine. Both automatic registration methods showed significant differences when compared to manual registration. The largest registration errors and biggest standard deviations were observed with automatic registration (XVI) across all imaging paradigms, including the clinical kV-setup. This can be attributed to high sensitivity of image-based registration to image artifacts, and confirms manufacturer recommendations of interactive (manual) verification of automatic registration results. The absolute maximum error in all matching attempts was 1.6 mm for manual matching, thus fulfilling the clinical requirements without exception.

4.3.2 Estimation of measurement setup error

Similar registration accuracy studies to assess different clinically used imaging modalities were performed by Yan et al. [103], Ballhausen et al. [10] and Meyer et al. [78]. Each study used a different approach to handle setup error as well as the clinical couch uncertainty of $\pm 0.5\,\mathrm{mm}$:

- Yan et al. evaluated the mechanical accuracy of the Varian OBI CBCT system.

They aligned a rigid pelvis anthropomorphic phantom on the couch with the help of fiducial markers and room lasers. The initial scan in isocenter was registered automatically and the random setup error was recorded. Pseudo-random known isocenter shifts were applied and CBCT scans were repeated. The detected isocenter offsets were corrected for setup error by subtraction of the previously determined random setup error, and the resulting corrected detector offsets were compared with actually applied couch offset. Mostly, registration was performed with automatic registration code provided by the manufacturer. In cases where visual examination was not sufficient, manual registration was performed. Outliers were excluded from the study since there was no clear trend observable. However, they did not handle the fact of limited mechanical resolution of 1 mm for the treatment couch. Thus, the actual manually simulated shift had an inaccuracy of ±0.5 mm. Results (mean ± standard deviation), including couch uncertainty, were (0.3 ± 0.6)mm in RL, (0.3 ± 0.6)mm in CC and (0.4 ± 0.6)mm in AP direction. Thus, they could conclude to identify the target within 1 mm [103].

- Ballhausen et al. performed a comparison study between the different positioning modalities of skin markers, ultrasound system and kV-CBCT. In their study, controlled phantom displacement was achieved by aligning the phantom with laser markers and mm−scales attached to the phantom. Different isocenter shifts were performed, image volumes were acquired and displacement errors were calculated with automatic image registration. To account for setup errors, a consensus value was calculated from all collected displacement errors for each modality, and the final displacement errors were compared relatively to this consensus value. Overall, the displacement offsets were below 1 mm [10].
- Meyer et al. presented a registration accuracy study with the Hexapod robotic treatment table (Medical Intelligence, Medizintechnik GmbH, Schwabmünchen, Germany). The movement of the Hexapod couch was computer-controlled (iGuide), accurate positioning was ensured by means of an optical tracking system (Polaris, NDI, Waterloo, Ontario, Canada), consisting of optical sensors on a rigidly attached couch bridge and an infrared tracking camera. The accuracy of the optical tracking system was 0.35 mm. In their study, only one CBCT scan was performed in isocenter position; the isocenter shifts were

> conducted in the treatment planning software on the planning CT dataset. This procedure ensured the isocenter shifts to be independent of the measurement system and any setup errors. All displacement errors were compared relative to the first registration in isocenter position. Registration was performed with the automatic registration algorithm provided by the manufacturer. Results of mean offset varied between $(0.2-0.3)$mm in all three translational directions, maximum absolute error was 0.6 mm [78].

Similar to the study in this thesis, they all concluded registration accuracy to be below 1 mm under clinical conditions with current imaging tools. Here, the couch isocenter offsets were realized using precise optical tracking (step width: 0.1 mm). The initial isocenter position was ensured with an accuracy of 0.05 mm. Each couch shift relative to this zero position could be defined as reference for latter detection error calculation.

4.3.3 Registration accuracy for combined kV-MV CBCT

The mean displacement errors of kV-MV CBCT for manual registration were (0.5 ± 0.3)mm in RL, (0.4 ± 0.4)mm in AP and (0.0 ± 0.4)mm in CC direction; outliers were included. The results differed only slightly among the imaging techniques. As expected, the kV-Chest$_1$ preset had the smallest mean error and standard deviation. The kV$_{180}$, MV$_{180}$ and kV-MV CBCT registration results were in the same range (mean value between $0.0-0.8$ mm). The largest detection errors occured for MV$_{180}$ CBCT, as expected due to poorest image quality compared to the others. For all imaging techniques, the mechanical registration offsets were, nevertheless - apart from very few outliers - below 1 mm, being within the manufacturer's specified accuracy range for standard clinical CBCT. Figures 3.7a, 3.7b, 3.8a and 3.8b demonstrate that image quality is sufficient even for undersampled image information in the MV contribution of kV-MV CBCT and in MV$_{180}$ CBCT; the tumor shape is clearly visible for all imaging techniques, the registration lies within $1/2$ pixel accuracy.

More specific evaluation is discussed in the following:

Interpretation of registration detection errors

As expected, clinical kV-Chest$_1$ CBCT results showed smallest detection errors with lowest fluctuations in all directions. The image quality was highest compared with other imaging techniques in this study due to the larger number of projections collected over a full 360° gantry arc.

For kV$_{180}$, MV$_{180}$ and kV-MV CBCT, the mean detection errors in CC direction were also close to zero (on average (0.0 ± 0.4) mm, maximum detection error 1.6 mm). However, for RL and AP direction, the mean was non-zero. This small but noticable bias of up to +0.5 mm in transverse slice could be explained by degraded image quality due to the following reasons:

- MV-cross-scatter was encountered on the kV-detector in all three imaging techniques due to simultaneous image acquisition.
- kV$_{180}$: Overlapping projections due to the additional cone-angle lead to a slight stripe artifact in AP-direction and reduced edge sharpness of the tumor-shape in transverse slices (Figures 3.7a, 3.7b, 3.8a and 3.8b).
- MV$_{180}$: Aliasing artifacts occured due to strong undersampling, as well as poor MV soft-tissue contrast [87].
- kV-MV: The MV contribution was undersampled and had worse soft-tissue CNR than kV contribution. However, the MV contribution still had strong impact on edge contours of the high contrast areas [79, 85], and thus the lung tumor shape was clearly apparent in kV-MV CBCT (Figures 3.7a, 3.7b, 3.8a and 3.8b).

Evaluation of detection error outliers

Outliers in CC direction for manual and automatic (in-house) registration in simultaneously acquired kV$_{180}$, MV$_{180}$ and kV-MV CBCT (Figure 3.9) occured in case of the second isocenter shift applied on the small star-shaped tumor inlay. Since the following consecutive shifts showed smaller detection errors, a positioning error of the experimenter is unlikely. The detection error rather attributed to the interplay of degraded image quality, as well as error-prone software interpolation for challenging

star-shaped tumor-inlay of diameter 10 mm; in planning CT the slice-to-slice variation is large due to a slice thickness of 1 mm. As a matter of fact, the marginal volume sizes of all four tumor-mimicking shapes induce most challenging test paradigms for registration accuracy. Outliers in kV-Chest$_1$ for manual registration in CC direction attribute to erroneous matching by the same physician. Even though these detection errors only range from $0.6-0.9$ mm, they are considered as outliers, because other detection errors in this larger number of measurement values are close to zero. Settings for Box-and-Whisker-diagrams were the same, disregarding the different number of measurement values for manual or automatic registration. In total, outliers of manual registration amount to 4% of all 480 measurement values, whereas 2.5% of all outliers were > 1 mm.

Overall systematic and stochastic error evaluation

Overall, the systematic error was reduced to < 0.05 mm by mechanical stability and geometrical accuracy of iGuide, which was stable over the whole measurement time. The stochastic mean error was between $0-0.5$ mm also due to limited dataset resolution. Pixel size and slice thickness differed for all 3D volume datasets. For the four planning CTs, the slice thickness was 1 mm and the pixel size varied between 0.8516 and 0.8809 mm, depending on field of view. For kV-Chest$_1$ CBCT, the pixel size and slice thickness were 1 mm; and 0.5 mm for kV$_{180}$, MV$_{180}$ and kV-MV CBCT. Thus, the registration offset of only one pixel could potentially result in an offset of 0.5 mm. Since the currently achievable precision in clinical routine is ± 1 mm, systematic and stochastic errors in this study are within the given limit.

4.3.4 Additional benefits of image acquisition in one breath-hold

To image lung tumors in breath-hold, the factor of tumor repositioning between two breath-hold phases had to be considered for overall imaging accuracy. Koshani et al [67] evaluated the short- and long-term reproducibility of intrathoracic tumor position using ABC within a patient study. Results of intra-fractional reproducibility as a measure for the movement between two breath-hold phases was (0.2 ± 0.7)mm in RL, (0.0 ± 1.5)mm in AP and (0.3 ± 1.4)mm in CC direction, maximum displacements

were 1.7 mm, 3.1 mm and 4.2 mm, respectively.
Avoiding these additional defective fluctuations between breath-hold phases in combination with shorter total imaging time and increased patient compliance further increases overall treatment precision.

4.3.5 Conclusion for kV-MV registration accuracy

This study showed that there is no degradation of registration accuracy with kV-MV CBCT compared to the other techniques including clinical standard kV-CBCT.

All other techniques, however, require at least a scan angle of 180°, corresponding to at least 30 s scan time. To prevent respiratory motion, the data acquisition process needs to be interrupted. To allow the patient to breathe, effective imaging times of $40-200$ s have to be accepted. Furthermore, this may lead to reduced image quality due to intra-fractional repositioning errors.

4.4 Final Conclusions

Combined ultrafast kV-MV cone-beam computed tomography (CBCT) is a promising approach to accelerate imaging for patients with lung tumors treated with deep inspiration breath-hold (DIBH). During a single breath-hold phase of 15 s, a combined 90°+90° kV-MV CBCT can be acquired, reducing motion artifacts to a minimum and increasing patient comfort in comparison to repeated breath-hold imaging techniques. Combined kV-MV CBCT development was recently finalized within our research group.

To judge clinical feasibility, kV-MV CBCT has to be compared to clinically established repeated breath-hold based imaging methods serving the same purpose in clinical routine. Since imaging times of these clinical presets are $3-4$ min including breath-hold interruptions, two additional monoenergetic (kV and MV) fastest achievable imaging methods (imaging times of $30-40$ s) were defined and compared with.

The aim of this thesis was to develop the concepts of testing the clinically-relevant properties of kV-MV CBCT: (I) dose exposure, (II) image quality and (III) registration accuracy. These tests were accomplished for kV-MV CBCT and other conventional

CBCT methods, followed by detailed evaluation and comparison. In particular, the three characteristic studies were performed as follows:

- ***(I) Dosimetric properties:*** For a reliable measurement of the absorbed dose in the imaging process, accurate dose calibration was performed for kV and MV energy. Extensive research was done to determine beam quality for both energy ranges. For direct comparison of MV to kV dose output, the MV dose was converted into kV-equivalent dose by considering the changes in relative biological effectiveness between kV and MV energies. Two dosimetry studies were performed: (1) patient simulation based on an inhomogeneous thorax phantom with measurements in various representative locations, and (2) determination of CT dose index (CTDI) for future quality assurance purposes. Results show comparable results of 20.5 mGE (Gray-equivalent) with the widely-used clinical imaging technique in the target region, whereas kV-MV spared healthy tissue and reduced dose to 6.6 mGE (30%) due to asymmetric dose distribution. Compared to the latest available clinical preset (9.1 mGy target dose), the kV-MV approach was maximum 3 times larger, however still minimum 8 times faster which justifies application of kV-MV for hypofractionated DIBH. CTDI result for kV-MV lied in between both clinical presets with a weighted CTDI of 12 mGE.
- ***(II) Image Quality:*** Comparison tests on image resolution and geometrical accuracy were performed. Image resolution was determined with a CatPhan phantom commonly used for quality assurance of CBCT. The geometrical accuracy was investigated on differently shaped tumor-mimicking inlays in an inhomogeneous thorax phantom. Compared with the other clinical and non-clinical imaging methods, image quality and image constancy were sufficient particularly for high contrast objects such as lung tumors.
- ***(III) Registration accuracy:*** Precise patient positioning before treatment is the quintessence for implementation of a novel imaging technique such as kV-MV CBCT. Therefore, a detailed phantom registration study was performed with different tumor-mimicking shapes in an inhomogeneous thorax phantom. 10 random pre-selected isocenter shifts were applied and served as gold standard for latter detection error evaluation. High precision phantom positioning (0.05 mm accuracy) could be achieved by optical tracking, practically eliminating residual

setup error. Registration was performed with three methods: (1) manual, (2) automatic software provided by manufacturer, and (3) self-developed automatic registration framework. Self-developed automatic registration enabled proper, objective evaluation by automatic determination of identical region of interest around the tumor-shapes for all imaging techniques. Mean displacement errors were (0.5 ± 0.3)mm in right-left, (0.4 ± 0.4)mm in anterior-posterior and (0.0 ± 0.4)mm in craniocaudal direction for kV-MV CBCT and manual registration. Manual registration emerged to be the most accurate method with smallest detection error variability and maximum errors of no more than 1.4 mm for kV-MV. Both automatic registration methods validated objectively the performance of the clinical experts.

In summary, the comparison studies conceptualized and accomplished in this thesis demonstrated that kV-MV CBCT is feasible for imminent clinical implementation: dosimetric properties were in agreement with common clinically established imaging techniques, whereas exposure to healthy tissue was reduced. Image quality and geometrical accuracy was sufficient particularly for high contrast areas, and registration accuracy was maintained below 1 mm. All requirements for successful implementation of single-breath-hold kV-MV CBCT into clinical routine are thus fulfilled.

The combination of single-breath-hold ultrafast kV-MV CBCT imaging (~ 15 s), target re-positioning (~ 2 min) and fast deep-inspiration breath-hold flattening-filter-free SABR ($\sim 2-4$ min) would reduce the total treatment time to $10-15$ min. With this combination of fast imaging and fast treatment, patient on-couch time would be tremendously reduced, improving the patient comfort and compliance. Treatment precision would be enhanced by reducing the number of necessary breath-hold phases to a minimum.

With the constant optimization regarding technical aspects of detector panel readout and scatter correction algorithms, improvements in image quality and thus possible reduction of MV dose output could be feasible in the near future. Furthermore, enhanced image quality could allow application to other tumor sites such as liver tumors.

Combined kV-MV CBCT is a promising new imaging technique which could soon be applied to the first lung cancer patients, with high potential in bringing the whole treatment delivery of image guided DIBH FFF-SABR to the currently fastest achievable level.

Bibliography

[1] *ICRU report 62: Prescribing, recording, and reporting photon beam therapy (supplement to ICRU report 50).* Bethesda, MD, 1999.

[2] *CatPhan 500 and 600 Manual.* Salem, NY, USA, 2009.

[3] Peter R. Almond, Peter J. Biggs, B. M. Coursey, W. F. Hanson, M. Saiful Huq, Ravinder Nath, and D. W. O. Rogers. AAPM's TG-51 protocol for clinical reference dosimetry of high-energy photon and electron beams. *Med. Phys.*, 26(9):1847–1870, 1999.

[4] A Amer, T Marchant, J Sykes, J Czaika, and C Moore. Imaging doses from the Elekta Synergy X-ray cone beam CT system. *Br. J. Radiol.*, 954(80):476–82, 2007.

[5] A. Arns, M. Blessing, D. Stsepankou, F. Lohr, F. Wenz, and H. Wertz. Dose Exposure and Geometric Accuracy of Ultrafast Kilovoltage-Megavoltage (kV-MV) Cone Beam CT for Image Guided Radiation Therapy of Lung Cancer. *Int. J. Radiat. Oncol.*, 84(3):S744, 2012.

[6] A. Arns, M. Blessing, D. Stsepankou, F. Lohr, F. Wenz, and H. Wertz. Matching Accuracy of Ultrafast Kilovoltage-Megavoltage (kV-MV) Cone Beam CT for Image Guided Radiation Therapy. *Int. J. Radiat. Oncol.*, 90(1S):S829, 2014.

[7] Anna Arns, Manuel Blessing, Jens Fleckenstein, Dzmitry Stsepankou, Judit Boda-Heggemann, Anna Simeonova-Chergou, Juergen Hesser, Frank Lohr, Frederik Wenz, and Hansjoerg Wertz. Towards clinical implementation of ultrafast combined kV-MV CBCT for IGRT of lung cancer: evaluation of registration accuracy based on phantom study. *Strahlentherapie und Onkol.*, (accepted).

[8] Anna Arns, Manuel Blessing, Dzmitry Stsepankou, Frank Lohr, Frederik Wenz, and Hansjoerg Wertz. Untersuchung der Strahlenbelastung durch kombinierte kV-MV CBCT- Bildgebung für die klinische Einführung in die bildgestützte Strahlentherapie. *DGMP Abstr. Bookl.*, page 206, 2013.

[9] Anna Maria Arns. *Modern Methods of Tomography.* Diploma thesis, Heidelberg University, 2009.

[10] Hendrik Ballhausen, Sheila Hieber, Minglun Li, Katia Parodi, Claus Belka, and Michael Reiner. Linearity of patient positioning detection. *Strahlentherapie und Onkol.*, 191(5):442–447, 2015.

[11] Stanley H. Benedict, Kamil M. Yenice, David Followill, James M. Galvin, William Hinson, Brian Kavanagh, Paul Keall, Michael Lovelock, Sanford Meeks, Lech Papiez, Thomas Purdie, Ramaswamy Sadagopan, Michael C. Schell, Bill Salter, David J. Schlesinger, Almon S. Shiu, Timothy Solberg, Danny Y. Song, Volker Stieber, Robert Timmerman, Wolfgang A. Tomé, Dirk Verellen, Lu Wang, and Fang-Fang Yin. Stereotactic body radiation therapy: The report of AAPM Task Group 101. *Med. Phys.*, 37(8):4078–4101, 2010.

[12] Jean-Pierre Bissonnette, Peter A. Balter, Lei Dong, Katja M. Langen, D. Michael Lovelock, Douglas J. Moseley, Jean Pouliot, Jan-Jakob Sonke, and Sua Yoo. Quality assurance for image-guided radiation therapy utilizing CT-based technologies : A report of the AAPM TG-179. *Med. Phys.*, 39(4):1946–1963, 2012.

[13] Jean-Pierre Bissonnette, Kevin N Franks, Thomas G Purdie, Douglas J Moseley, Jan-Jakob Sonke, David A Jaffray, Laura A Dawson, and Andrea Bezjak. Quantifying interfraction and intrafraction tumor motion in lung stereotactic body radiotherapy using respiration-correlated cone beam computed tomography. *Int. J. Radiat. Oncol. Biol. Phys.*, 75(3):688–95, nov 2009.

[14] Bengt E. Bjaerngard and Hobart Shackford. Attenuation in high-energy x-ray beams. *Med. Phys.*, 21(7):1069, 1994.

[15] M. Blessing, A. Arns, H. Wertz, D. Stsepankou, J. Boda-Heggemann, F. Lohr, J. Hesser, and F. Wenz. Image Guided Radiation Therapy Using Ultrafast kV-MV CBCT: End-to-End Test Results of the Finalized Implementation. *Int. J. Radiat. Oncol.*, 90(1):S828–S829, 2014.

[16] Manuel Blessing. *Synchronized and simultaneous kilovoltage-megavoltage cone-beam CT imaging under breathhold and phenomenological beam modeling for scatter prediction and correction.* PhD thesis, Heidelberg University, 2014.

[17] Manuel Blessing, Anna Arns, Hansjoerg Wertz, Dzmitry Stsepankou, Judit Boda-Heggemann, Juergen Hesser, Frederik Wenz, and Frank Lohr. Finalized implementation of ultrafast kilovoltage-megavoltage CBCT for Image Guided Radiotherapy of lung cancer: system description and real-time results. (submitted).

[18] Manuel Blessing, Dzmitry Stsepankou, Hansjoerg Wertz, Anna Arns, Frank Lohr, Jürgen Hesser, and Frederik Wenz. Breath-hold target localization with simultaneous kilovoltage/megavoltage cone-beam computed tomography and fast reconstruction. *Int. J. Radiat. Oncol. Biol. Phys.*, 78(4):1219–26, Nov 2010.

[19] J. Boda-Heggemann, A. Jahnke, L. Jahnke, A. Simeonova, S.K. Mai, H. Wertz, A. Zimmermann, S. von Swietochowski, F. Wenz, and F. Lohr. Breath-Hold Cone Beam CT (CBCT): Improved Image Quality With "Stop-and-Go" Breath Hold-Only Acquisition Versus Repetitive Breath Hold During Continuous Rotation. *Int. J. Radiat. Oncol.*, 90(1):S826, 2014.

[20] J. Boda-Heggemann, F. Lohr, H. Wertz, I. Löb, B. Küpper, a. Kavanagh, V.N. Hansen, M. Brada, F. Wenz, and H. McNair. Repeat ABC-breath Hold Imaging with Cone-beam CT. *Int. J. Radiat. Oncol.*, 78(3):S736, Nov 2010.

[21] Judit Boda-Heggemann, Jens Fleckenstein, Frank Lohr, Hansjörg Wertz, Mohammed Nachit, Manuel Blessing, Dzimitry Stsepankou, Iris Löb, Beate Küpper, Anthony Kavanagh, Vibeke N. Hansen, Michael Brada, Frederik Wenz, and Helen McNair. Multiple breath-hold CBCT for online image guided radiotherapy of lung tumors: Simulation with a dynamic phantom and first patient data. *Radiother. Oncol.*, 98(3):309–316, 2011.

[22] Judit Boda-Heggemann, Anian Frauenfeld, Christel Weiss, Anna Simeonova, Christian Neumaier, Kerstin Siebenlist, Ulrike Attenberger, Claus Peter Heußel, Frank Schneider, Frederik Wenz, and Frank Lohr. Clinical outcome of hypofractionated breath-hold image-guided SABR of primary lung tumors and lung metastases. *Radiat. Oncol.*, 9:10, Jan 2014.

[23] Judit Boda-Heggemann, Antje-Christin Knopf, Anna Simeonova, Hansjoerg Wertz, Florian Stieler, Anika Jahnke, Lennart Jahnke, Lena Vogel, Anna Arns, Manuel Blessing, Jens Fleckenstein, Frederik Wenz, and Frank Lohr. DBIH (Deep Inspiratory Breath Hold)- based radiotherapy - a clinical review. *Int. J. Radiat. Oncol. Biol. Phys.*, (in press), 2015.

[24] Judit Boda-Heggemann, Frank Lohr, Frederik Wenz, Michael Flentje, and Matthias Guckenberger. kV cone-beam CT-based IGRT: a clinical review. *Strahlenther. Onkol.*, 187(5):284–91, May 2011.

[25] Judit Boda-Heggemann, Sabine Mai, Jens Fleckenstein, Kerstin Siebenlist, Anna Simeonova, Michael Ehmann, Volker Steil, Frederik Wenz, Frank Lohr, and Florian Stieler. Flattening-filter-free intensity modulated breath-hold image-guided SABR (Stereotactic ABlative Radiotherapy) can be applied in a 15-min treatment slot. *Radiother. Oncol.*, 109(3):505–509, 2013.

[26] Carmia Borek, Eric J. Hall, and Marco Zaider. X rays may be twice as potent as γ rays for malignant transformation at low doses. *Nat.*, 301(5896):156–158, 1983.

[27] Almudena Cascales, Florent Martinetti, Deborah Belemsagha, and Cecile Le Pechoux. Challenges in the treatment of early non-small cell lung cancer: what is the standard, what are the challenges and what is the future for radiotherapy? *Transl. lung cancer Res.*, 3(4):195–204, 2014.

[28] Harry C Y Cheng, Vincent W C Wu, Eva S F Liu, and Dora L W Kwong. Evaluation of radiation dose and image quality for the Varian cone beam computed tomography system. *Int. J. Radiat. Oncol. Biol. Phys.*, 80(1):291–300, May 2011.

[29] Alexander Chi, Nam Phong Nguyen, and Ritsuko Komaki. The Potential Role of Respiratory Motion Management and Image Guidance in the Reduction of Severe Toxicities Following Stereotactic Ablative Radiation Therapy for Patients with Centrally Located Early Stage Non-Small Cell Lung Cancer or Lung Metastases. *Front. Oncol.*, 4(June):1–12, 2014.

[30] Byungchul Cho, Per R Poulsen, Alex Sloutsky, Amit Sawant, and Paul J Keall. First demonstration of combined kV/MV image-guided real-time dynamic multileaf-collimator target tracking. *Int. J. Radiat. Oncol. Biol. Phys.*, 74(3):859–67, Jul 2009.

[31] W. Eubank D. Mattes, D.R. Haynor, H. Vesselle, T. Lewellen. Non-rigid multimodality image registration. In *Med. Imaging 2001 Image Process. SPIE Publ.*, pages 1609–1620, 2001.

[32] George X. Ding and Charles W. Coffey. Dosimetric evaluation of the One-Dose MOSFET for measuring kilovoltage imaging dose from image-guided radiotherapy procedures. *Med. Phys.*, 37(9):4880, 2010.

[33] George X. Ding, Dennis M. Duggan, and Charles W. Coffey. Accurate patient dosimetry of kilovoltage cone-beam CT in radiation therapy. *Med. Phys.*, 35(3):1135, 2008.

[34] Robert L. Dixon. A new look at CT dose measurement: Beyond CTDI. *Med. Phys.*, 30(6):1272, 2003.

[35] Elekta. *Clinical User Manual XVI 4.0*. 2008.

[36] Elekta. *XVI r4.2 Elekta Synergy Customer Acceptance Tests*. 2009.

[37] Elekta. *Clinical User Manual XVI 5.0*. 2014.

[38] Elekta. *White Paper: Optimizing Image Quality in XVI VolumeView*. 2015.

[39] Rebecca Fahrig, Robert Dixon, Thomas Payne, Richard L. Morin, Arundhuti Ganguly, and Norbert Strobel. Dose and image quality for a cone-beam C-arm CT system. *Med. Phys.*, 33(12):4541, 2006.

[40] L. a. Feldkamp, L. C. Davis, and J. W. Kress. Practical cone-beam algorithm. *J. Opt. Soc. Am. A*, 1(6):612, 1984.

[41] Christina Fitzmaurice, Daniel Dicker, Amanda Pain, and Others. The Global Burden of Cancer 2013. *JAMA Oncol.*, 1(4):505, 2015.

[42] Dietmar Georg, Tommy Knöös, and Brendan McClean. Current status and future perspective of flattening filter free photon beams. *Med. Phys.*, 38(3):1280, 2011.

[43] Christy Goldsmith and Andrew Gaya. Stereotactic ablative body radiotherapy (SABR) for primary and secondary lung tumours. *Cancer Imaging*, 12(2):351–360, 2012.

[44] S Green and B Jones. Second cancer risk, 2005.

[45] H Guan, F F Yin, Y Zhu, and J H Kim. Adaptive portal CT reconstruction: a simulation study. *Med. Phys.*, 27(10):2209–14, 2000.

[46] Matthias Guckenberger, Thomas Krieger, Anne Richter, Kurt Baier, Juergen Wilbert, Reinhart A. Sweeney, and Michael Flentje. Potential of image-guidance, gating and real-time tracking to improve accuracy in pulmonary stereotactic body radiotherapy. *Radiother. Oncol.*, 91(3):288–295, 2009.

[47] Matthias Guckenberger, Juergen Wilbert, Thomas Krieger, Anne Richter, Kurt Baier, Juergen Meyer, and Michael Flentje. Four-Dimensional Treatment Planning for Stereotactic Body Radiotherapy. *Int. J. Radiat. Oncol. Biol. Phys.*, 69(1):276–285, 2007.

[48] R M Harrison. Second cancers following radiotherapy: A suggested common dosimetry framework for therapeutic and concomitant exposures. *Br. J. Radiol.*, 77(924):986–990, 2004.

[49] William R. Hendee, Geoffrey S. Ibbott, and Eric G. Hendee. *Radiation Therapy Physics*. John Wiley & Sons, 3rd edition, 2005.

[50] A. L. Hill. Half value layer measurements to facilitate patient dose assessment for newer CT scanners using published normalized dose data. *Br. J. Radiol.*, 72(Aug):792–798, 1999.

[51] M A Hill. The variation in biological effectiveness of X-rays and gamma rays with energy. *Radiat. Prot. Dosimetry*, 112(4):471–81, Jan 2004.

[52] D H Hristov and B G Fallone. A grey-level image alignment algorithm for registration of portal images and digitally reconstructed radiographs. *Med. Phys.*, 23(1):75–84, 1996.

[53] Nezahat Hunter and Colin R Muirhead. Review of relative biological effectiveness dependence on linear energy transfer for low-LET radiations. *J. Radiol. Prot.*, 29(1):5–21, Mar 2009.

[54] Daniel E. Hyer and David E. Hintenlang. Estimation of organ doses from kilovoltage cone-beam CT imaging used during radiotherapy patient position verification. *Med. Phys.*, 37(9):4620, 2010.

[55] DE Hyer, CF Serago, and Siyong Kim. An organ and effective dose study of XVI and OBI cone-beam CT systems. *J. Appl. Clin. Med. Phys.*, 11(2):181–197, 2010.

[56] International Atomic Energy Agency (IAEA). *Absorbed Dose Determination in External Beam Radiotherapy: An International Code of Practice for Dosimetry Based on Standards of Absorbed Dose to Water, Technical Reports Series No. 398*. Vienna, 2000.

[57] ICRP. 1990 Recommendation of the International Commission of Radiological Protection. *ICRP Publ. 60. Ann. ICRP*, 21(1-3), 1991.

[58] ICRP. 2007 Recommendation of the International Commission of Radiological Protection. *ICRP Publ. 103. Annu. ICRP*, 37, 2007.

[59] Mohammad K. Islam, Thomas G. Purdie, Bernhard D. Norrlinger, Hamideh Alasti, Douglas J. Moseley, Michael B. Sharpe, Jeffrey H. Siewerdsen, and David A. Jaffray. Patient dose from kilovoltage cone beam computed tomography imaging in radiation therapy. *Med. Phys.*, 33(6):1573, 2006.

[60] DA Jaffray and JH Siewerdsen. Flat-panel cone-beam computed tomography for image-guided radiation therapy. *Int. J. Radiat. Oncol. Biol. Phys.*, 53(5):1337–1349, 2002.

[61] Paul J Keall, Gig S Mageras, James M Balter, Richard S Emery, Kenneth M Forster, Steve B Jiang, Jeffrey M Kapatoes, Daniel A Low, Martin J Murphy, Brad R Murray, Chester R Ramsey, Marcel B Van Herk, S Sastry Vedam, John W Wong, and Ellen Yorke. The management of respiratory motion in radiation oncology report of AAPM Task Group 76. *Med. Phys.*, 33(10):3874–3900, 2006.

[62] Faiz M. Khan. *The Physics of Radiation Therapy*. Lippincott Williams & Wilkins, a Wolters Kluwer business, 4th edition, 2010.

[63] Sangroh Kim, Sua Yoo, Fang-Fang Yin, Ehsan Samei, and Terry Yoshizumi. Kilovoltage cone-beam CT: Comparative dose and image quality evaluations in partial and full-angle scan protocols. *Med. Phys.*, 37(7):3648, 2010.

[64] C Kirkby, E Ghasroddashti, Y Poirier, M Tambasco, and R D Stewart. RBE of kV CBCT radiation determined by Monte Carlo DNA damage simulations. *Phys. Med. Biol.*, 58(16):5693–704, 2013.

[65] C Kleinschmidt. Analytical considerations of beam hardening in medical accelerator photon spectra. *Med. Phys.*, 26(9):1995–1999, 1999.

[66] S C Klevenhagen, R J Aukett, R M Harrison, C Moretti, A E Nahum, and K E Rosser. The IPEMB code of practice for the determination of absorbed dose for x-rays below 300 kV generating potential (0.035 mm Al - 4 mm Cu HVL ; 10 - 300 kV generating potential). *Phys. Med. Biol.*, 41:2605–2625, 1996.

[67] Rojano Koshani, James M. Balter, James A. Hayman, George T. Henning, and Marcel van Herk. Short-term and long-term reproducibility of lung tumor

position using active breathing control (ABC). *Int. J. Radiat. Oncol. Biol. Phys.*, 65(5):1553–1559, 2006.

[68] R L Kruger, C H McCollough, and F E Zink. Measurement of half-value layer in x-ray CT: a comparison of two noninvasive techniques. *Med. Phys.*, 27(8):1915–1919, 2000.

[69] M. Kuwahara, K Hachimura, S. Eiho, and M. Kinoshita. Processing of RI-angiocardiographic images. In K. PrestonJr. and M. Onoe, editors, *Digit. Process. Biomed. Images*, pages 187–202. New York: Plenum, 1976.

[70] Tianfang Li, Lei Xing, Peter Munro, Christopher McGuinness, Ming Chao, Yong Yang, Bill Loo, and Albert Koong. Four-dimensional cone-beam computed tomography using an on-board imager. *Med. Phys.*, 33(10):3825, 2006.

[71] Minglu Liu, Yunlai Wang, and Xiongfei Liao. Computed Tomography Dose Index Measurement Voltage Helical CT For Hi-ART Megavoltage Helical CT. *Radiat. Prot. Dosimetry*, December 8:1–5, 2015.

[72] C.-M. Ma, C. W. Coffey, L. a. DeWerd, C. Liu, R. Nath, S. M. Seltzer, and J. P. Seuntjens. AAPM protocol for 40-300 kV x-ray beam dosimetry in radiotherapy and radiobiology. *Med. Phys.*, 28(6):868, 2001.

[73] N Mail, D J Moseley, J H Siewerdsen, and D A Jaffray. The influence of bowtie filtration on cone-beam CT image quality. *Med. Phys.*, 36:22–32, 2009.

[74] V. Marchand, S. Zefkili, J. Desrousseaux, L. Simon, C. Dauphinot, and P. Giraud. Dosimetric comparison of free-breathing and deep inspiration breath-hold radiotherapy for lung cancer. *Strahlentherapie und Onkol.*, 188(7):582–591, 2012.

[75] Frank J. Massey. The Kolmogorov-Smirnov Test for Goodness of Fit. *J. Am. Stat. Assoc.*, 46(253):68–78, 1951.

[76] J. R. McClelland, D. J. Hawkes, T. Schaeffter, and A. P. King. Respiratory motion models: A review. *Med. Image Anal.*, 17(1):19–42, 2013.

[77] Helen A. McNair, Juliet Brock, J. R N Symonds-Tayler, Sue Ashley, Sally Eagle, Philip M. Evans, Anthony Kavanagh, Niki Panakis, and Michael Brada. Feasibility of the use of the Active Breathing Coordinator (ABC) in patients receiving radical radiotherapy for non-small cell lung cancer (NSCLC). *Radiother. Oncol.*, 93(3):424–429, 2009.

[78] Jürgen Meyer, Jürgen Wilbert, Kurt Baier, Matthias Guckenberger, Anne Richter, Otto Sauer, and Michael Flentje. Positioning accuracy of cone-beam computed tomography in combination with a HexaPOD robot treatment table. *Int. J. Radiat. Oncol. Biol. Phys.*, 67(4):1220–8, Mar 2007.

[79] Olivier Morin, Amy Gillis, Josephine Chen, Michèle Aubin, M Kara Bucci, Mack Roach, and Jean Pouliot. Megavoltage cone-beam CT: system description and clinical applications. *Med. Dosim.*, 31(1):51–61, Jan 2006.

[80] Martin J. Murphy, James Balter, Stephen Balter, Jose A. BenComo, Indra J. Das, Steve B. Jiang, C.-M. Ma, Gustavo H. Olivera, Raymond F. Rodebaugh, Kenneth J. Ruchala, Hiroki Shirato, and Fang-Fang Yin. The management of imaging dose during image-guided radiotherapy: Report of the AAPM Task Group 75. *Med. Phys.*, 34(10):4041, 2007.

[81] Keiichi Nakagawa, Hideomi Yamashita, Kenshiro Shiraishi, Hiroshi Igaki, Atsuro Terahara, Naoki Nakamura, Kuni Ohtomo, Shigeki Saegusa, Takashi Shiraki, Takashi Oritate, and Kiyoshi Yoda. Verification of in-treatment tumor position using kilovoltage cone-beam computed tomography: a preliminary study. *Int. J. Radiat. Oncol. Biol. Phys.*, 69(4):970–3, Nov 2007.

[82] Pierina Navarria, Anna Maria Ascolese, Pietro Mancosu, Filippo Alongi, Elena Clerici, Angelo Tozzi, Cristina Iftode, Giacomo Reggiori, Stefano Tomatis, Maurizio Infante, Marco Alloisio, Alberto Testori, Antonella Fogliata, Luca Cozzi, Emanuela Morenghi, and Marta Scorsetti. Volumetric modulated arc therapy with flattening filter free (FFF) beams for stereotactic body radiation therapy (SBRT) in patients with medically inoperable early stage non small cell lung cancer (NSCLC). *Radiother. Oncol.*, 107(3):414–418, 2013.

[83] Hooshang Nikjoo and Lennart Lindborg. RBE of low energy electrons and photons. *Phys. Med. Biol.*, 55(10):R65–109, May 2010.

[84] E. B. Podgorsak and Kristofer Kainz. *Radiation Oncology Physics: A Handbook for Teachers and Students*, volume 33. 2006.

[85] Jean Pouliot, Ali Bani-Hashemi, Michelle Svatos, Farhad Ghelmansarai, Matthias Mitschke, Michele Aubin, Ping Xia, Olivier Morin, Kara Bucci, Mack Roach, Paco Hernandez, Zirao Zheng, Dimitre Hristov, and Lynn Verhey. Low-dose megavoltage cone-beam CT for radiation therapy. *Int. J. Radiat. Oncol.*, 61(2):552–560, Feb 2005.

[86] PTW Freiburg. *Ionizing Radiation Detectors: Including Codes of Practice.* 2013.

[87] R. Schulze, U. Heil, D. Groß, D. D. Bruellmann, E. Dranischnikow, U. Schwanecke, and E. Schoemer. Artefacts in CBCT: A review. *Dentomaxillofacial Radiol.*, 40(5):265–273, 2011.

[88] Yvette Seppenwoolde, Hiroki Shirato, Kei Kitamura, Shinichi Shimizu, Marcel Van Herk, Joos V. Lebesque, and Kazuo Miyasaka. Precise and real-time measurement of 3D tumor motion in lung due to breathing and heartbeat, measured during radiotherapy. *Int. J. Radiat. Oncol. Biol. Phys.*, 53(4):822–834, 2002.

[89] Thomas B. Shope. A method for describing the doses delivered by transmission x-ray computed tomography. *Med. Phys.*, 8(4):488, 1981.

[90] Rebecca L. Siegel, Kimberly D. Miller, and Ahmedin Jemal. Cancer statistics , 2015 . *CA Cancer J Clin*, 65(1):21254, 2015.

[91] Anna O Simeonova, Katharina Fleckenstein, Hansjörg Wertz, Anian Frauenfeld, Judit Boda-Heggemann, Frank Lohr, and Frederik Wenz. Are three doses of stereotactic ablative radiotherapy (SABR) more effective than 30 doses of conventional radiotherapy? *Transl. Lung Cancer Res.*, 1(1):45–53, 2012.

[92] A.O. Simeonova, A. Jahnke, L. Jahnke, K. Siebenlist, F. Stieler, S. Mai, J. Boda-Heggemann, F. Wenz, and F. Lohr. Automatically Gated CBCT-Controlled Fast Breath-Hold SBRT Is Dosimetrically Robust and Facilitates Precision Treatments for Patients With Lung Cancer. *Int. J. Radiat. Oncol.*, 90(1):S891, 2014.

[93] James W. Snider, Eric K. Oermann, Viola Chen, Jennifer Rabin, Simeng Suy, Xia Yu, Saloomeh Vahdat, Sean P. Collins, Filip Banovac, Eric Anderson, and Brian T. Collins. CyberKnife with Tumor Tracking: An Effective Treatment for High-Risk Surgical Patients with Single Peripheral Lung Metastases. *Front. Oncol.*, 2(June):1–5, 2012.

[94] William Y. Song, Srijit Kamath, Shuichi Ozawa, Shlomi Al Ani, Alexei Chvetsov, Niranjan Bhandare, Jatinder R. Palta, Chihray Liu, and Jonathan G. Li. A dose comparison study between XVI and OBI CBCT systems. *Med. Phys.*, 35(2):480, 2008.

[95] Jan-Jakob Sonke, Lambert Zijp, Peter Remeijer, and Marcel van Herk. Respiratory correlated cone beam CT. *Med. Phys.*, 32(4):1176, 2005.

[96] Robert D. Timmerman, Brian D. Kavanagh, L. Chinsoo Cho, Lech Papiez, and Lei Xing. Stereotactic body radiation therapy in multiple organ sites, 2007.

[97] Dale Trout and John P Kelley. Beam Quality Measurements in Diagnostic Roentgenology. *Am. J. Roentgenol.*, 112:622–627, 1971.

[98] L K Wagner, B R Archer, and F Cerra. On the measurement of half-value layer in film-screen mammography. *Med. Phys.*, 17(6):989–997, 1990.

[99] Hansjoerg Wertz, Dzmitry Stsepankou, Manuel Blessing, Michael Rossi, Chris Knox, Kevin Brown, Uwe Gros, Judit Boda-Heggemann, Cornelia Walter, Juergen Hesser, Frank Lohr, and Frederik Wenz. Fast kilovoltage/megavoltage (kVMV) breathhold cone-beam CT for image-guided radiotherapy of lung cancer. *Phys. Med. Biol.*, 55(15):4203–17, Aug 2010.

[100] F Wilcoxon. Individual comparisons of grouped data by ranking methods. *J. Econ. Entomol.*, 39(6):269, 1946.

[101] Andrew D. Wiles, David G. Thompson, and Donald D. Frantz. Accuracy assessment and interpretation for optical tracking systems. *Med. Imaging 2004 Vis. Image-guided Preced. Display. Proc. SPIE*, 5367:421–432, 2004.

[102] John W. Wong, Michael B. Sharpe, David A. Jaffray, Vijay R. Kini, John M. Robertson, Jannifer S. Stromberg, and Alavro A. Martinez. The use of active breathing control (ABC) to reduce margin for breathing motion. *Int. J. Radiat. Oncol. Biol. Phys.*, 44(4):911–919, 1999.

[103] Hui Yan, Liwei Zhang, and Fang-Fang Yin. A phantom study on target localization accuracy using cone-beam computed tomography. *Clin. Med. Oncol.*, 2(919):501–510, 2008.

[104] Fang-Fang Yin, Huaiqun Guan, and Wenkai Lu. A technique for on-board CT reconstruction using both kilovoltage and megavoltage beam projections for 3D treatment verification. *Med. Phys.*, 32(9):2819–2826, 2005.

[105] Sua Yoo, Gwe-Ya Kim, Rabih Hammoud, Eric Elder, Todd Pawlicki, Huaiqun Guan, Timothy Fox, Gary Luxton, Fang-Fang Yin, and Peter Munro. A quality assurance program for the on-board imager. *Med. Phys.*, 33(11):4431, 2006.

[106] M K Yu, R S Sloboda, and B Murray. Linear accelerator photon beam quality at off-axis points. *Med. Phys.*, 24(2):233–239, 1997.

[107] Renming Zhong, Jin Wang, Lin Zhou, Feng Xu, Li Liu, Jidan Zhou, Xiaoqin Jiang, Nianyong Chen, Sen Bai, and You Lu. Implementation of single-breath-hold cone beam CT guided hypofraction radiotherapy for lung cancer. *Radiat. Oncol.*, 9(1):77, 2014.

A Appendix

A.1 Measurements of Half-Value-Layers for kV-energy beam quality determination

Al [mm]	**kV-Chest$_1$**		**kV-Chest$_2$**		**kV-contribution of kV-MV**	
	total dose [mGy]	normalized	total dose [mGy]	normalized	total dose [mGy]	normalized
0	1.764		6.508		1.171	
0	1.766		6.499		1.173	
0	1.774		6.562		1.181	
0	1.782		6.552		1.190	
mean	**1.772**	**1.000**	**6.530**	**1.000**	**1.1788**	**1.000**
1.06	1.586	0.895	5.780	0.885	1.013	0.859
2.06	1.440	0.813	5.189	0.795	0.885	0.751
3.11	1.306	0.737	4.666	0.715	0.772	0.655
4.11	1.213	0.685	4.198	0.643	0.686	0.582
4.62					0.663	0.563
5.14	1.093	0.617	3.839	0.588	0.620	0.526
5.45					0.605	0.513
5.60					0.595	0.505
5.64					**0.589**	**0.500**
5.65					0.589	0.499
5.70					0.586	0.497
5.80					0.581	0.493
6.00					0.568	0.482
6.20	1.003	0.566	3.511	0.538	0.557	0.473
6.60	0.965	0.545	3.351	0.513	0.521	0.442
7.00			3.299	0.505	0.509	0.431
7.10			3.285	0.503		
7.15			**3.267**	**0.500**		
7.20	0.916	0.517	3.226	0.494	0.491	0.416
7.40	0.905	0.511	3.160	0.484	0.482	0.409
7.60	0.888	0.501	3.119	0.478	0.473	0.402
7.65	**0.885**	**0.499**				
7.66	0.882	0.498				
7.70	0.880	0.497				
7.80	0.872	0.492				
8.00	0.858	0.484	2.990	0.458	0.456	0.387
8.26	0.842	0.476				
9.25	0.783	0.442	2.735	0.419	0.408	0.346
10.31	0.716	0.404	2.517	0.385	0.365	0.310

Table A.1: Measurement data of Half-Value-Layer for kV-Chest$_1$, kV-Chest$_2$ and kV contribution of kV-MV CBCT.

A.2 Matlab Code: (III) Objective automatic registration with self-developed software (in-house)

```
%%%%%%%%%%%%%%%%%%%%%%%%%%%%%%%%%%%%%%%%%%%%%%%%%%%%%%%%%%%%%%%%%%%%%%%%%%%%%%%
%% Automatic Registration (in-house) %%%%%%%%%%%%%%%%%%%%%%%%%%%%%%%%%%%%%%%%%%%
%%%%%%%%%%%%%%%%%%%%%%%%%%%%%%%%%%%%%%%%%%%%%%%%%%%%%%%%%%%%%%%%%%%%%%%%%%%%%%%
%% AUTHOR: Anna Arns (anna.arns@umm.de) - July 2015
%%
% input data:
% Vol_pCT = Vol_fixed ; PixelSize: ps_fixed ; SliceThickness: st_fixed ;
%                       ISO_fixed
% Vol_CBCT = Vol_moving  ; PixelSize: ps_CBCT ; SliceThickness: st_CBCT
%

%% DATA to be evaluated
Phantoms = {'Ball' , 'Cylinder' , 'Star10' , 'Star15' };
Method = {'kV-MV' , 'kV-180' , 'MV-180', 'kV_Chest'};
% for shifts 1-10
% alignment box: 18 pixel from center in all 3 directions
ab = 18;
%...
%.... loop for data (not included in this code)
%...

%% load fixed data
[Vol_fixed, ps_fixed, st_fixed, ISO_fixed] = ...
                                    MyF_load_Vol_fixed(datapath_fixed);

%% load moving data
switch Method
    case 'kV-MV'
        [Vol_moving, ps_moving, st_moving] = ...
                                        MyF_load_kVMV(datapath_moving);
    case 'kV-180'
        [Vol_moving, ps_moving, st_moving] = ...
                                        MyF_load_kV180(datapath_moving);
    case 'MV-180'
        [Vol_moving, ps_moving, st_moving] = ...
                                        MyF_load_MV180(datapath_moving);
    case 'kV-Chest'
        [Vol_moving, ps_moving, st_moving] = ...
                                        MyF_load_kV_Chest(datapath_moving);
end

%% 1. generate alignment box
```

```
% fixed volume: (ISO_fixed is given in world coordinates - intrinsic
%                 coordinates are required)
col_fixed   = [(round(ISO_fixed(1)/ps_fixed)-ab+1):...
                                          (round(ISO_fixed(1)/ps_fixed)+ab)];
row_fixed   = [(round(ISO_fixed(2)/ps_fixed)-ab+1):...
                                          (round(ISO_fixed(2)/ps_fixed)+ab)];
slice_fixed = [(round(ISO_fixed(3)/st_fixed)-ab+1):...
                                          (round(ISO_fixed(3)/st_fixed)+ab)];
Vol_fixed_ab   = Vol_fixed(row_fixed, col_fixed, slice_fixed);
trafo_fixed_ab = [(col_fixed(1)-1)*ps_fixed, ...
                  (row_fixed(1)-1)*ps_fixed, ...
                  (slice_fixed(1)-1)*st_fixed];

% moving volume: (center values of rough tumor-shape position assumed by
%             a priori isocenter shift information (for in total 10 shifts))
col_moving   = [(cen_col_moving-ab+1):(cen_col_moving+ab)];
row_moving   = [(cen_row_moving-ab+1):(cen_row_moving+ab)];
slice_moving = [(cen_slice_moving-ab+1):(cen_slice_moving+ab)];
Vol_moving_ab   = Vol_moving(row_moving, col_moving, slice_moving);
trafo_moving_ab = [(col_moving(1)-1)*ps_moving,...
                   (row_moving(1)-1)*ps_moving, ...
                   (slice_moving(1)-1)*st_moving];

disp('Alignment box set for fixed and moving volume.');

%% convert from intrinsic to world coordinate system
% full volumes
R_fixed = imref3d([length(Vol_fixed(:,1,1)), length(Vol_fixed(1,:,1)), ...
             length(Vol_fixed(1,1,:))], ps_fixed, ps_fixed, st_fixed);
R_moving = imref3d([length(Vol_moving(:,1,1)), length(Vol_moving(1,:,1)), ...
             length(Vol_moving(1,1,:))], ps_moving, ps_moving, st_moving);
% alignment box volumes
R_fixed_ab = imref3d([length(Vol_fixed_ab(:,1,1)), length(Vol_fixed_ab(1,:,1)), ...
             length(Vol_fixed_ab(1,1,:))], ps_fixed, ps_fixed, st_fixed);
R_moving_ab = imref3d([length(Vol_moving_ab(:,1,1)), length(Vol_moving_ab(1,:,1)), ...
             length(Vol_moving_ab(1,1,:))], ps_moving, ps_moving, st_moving);


%% 2. Rigid translational registration with Matlab toolkit:
% measure of similarity: multimodal Mutual Information
% (since both fixed and moving volumes differ in intensity)
[optimizer,metric]=imregconfig('multimodal');
optimizer.MaximumIterations = 300;
optimizer.InitialRadius = 0.004;
% registration on alignment box volumes!
t_matrix = imregtform(Vol_moving_ab,R_moving_ab,Vol_fixed_ab, R_fixed_ab, ...
                                              'translation',optimizer,metric);


%% 3. Back-transformation to full 3D volume after registration
```

```
% full 3D volume transformation vectors in world coordinates
t_matrix.T(4,1) = trafo_fixed_ab(1) + t_matrix_ab.T(4,1) - trafo_moving_ab(1);
t_matrix.T(4,2) = trafo_fixed_ab(2) + t_matrix_ab.T(4,2) - trafo_moving_ab(2);
t_matrix.T(4,3) = trafo_fixed_ab(3) + t_matrix_ab.T(4,3) - trafo_moving_ab(3);


%% 4. Calculation of final registered isocenter-shift in linac coordinates:
% calculate center points of unregistered full 3D volume moving
centerXWorld_V_moving = mean(R_moving.XWorldLimits);
centerYWorld_V_moving = mean(R_moving.YWorldLimits);
centerZWorld_V_moving = mean(R_moving.ZWorldLimits);
% map center coordinates as coordinates after registration in coordinate
% system of fixed volume
[xWorld_V_moving,yWorld_V_moving,zWorld_V_moving] = ...
    transformPointsForward(t_matrix,...
       centerXWorld_V_moving,centerYWorld_V_moving,centerZWorld_V_moving);

% calculate final isocenter shift in LINAC world coordinate system
Linac_shift_RL_moving =       xWorld_V_moving - ISO_fixed(1);
Linac_shift_AP_moving = (-1)*(yWorld_V_moving - ISO_fixed(2));
Linac_shift_CC_moving = (-1)*(zWorld_V_moving - ISO_fixed(3));


%% 5. Visualization of registered fixed (pCT) and moving (CBCT) volume

% determine full 3D registered moving volume
[Vol_reg,R_reg] = imwarp(Vol_moving,R_moving,t_matrix,...
                                        'linear','OutputView',R_fixed);
% determine alignment box registered moving volume
[Vol_reg_ab,R_reg_ab] = imwarp(Vol_moving_ab,R_moving_ab,t_matrix_ab,...
                                     'linear','OutputView',R_fixed_cb);

% choose significant slice to show or run a loop
i=50; j=18;

% convert from intrinsic to world coordinate system for full 3D volume
R_fixed_2d  = imref2d([length(Vol_fixed(:,1,i)),...
                           length(Vol_fixed(1,:,i))],ps_fixed,ps_fixed);
R_moving_2d = imref2d([length(Vol_moving(:,1,i)),...
                         length(Vol_moving(1,:,i))],ps_moving,ps_moving);
R_reg_2d    = imref2d([length(Vol_reg(:,1,i)),...
                          length(Vol_reg(1,:,i))], ps_fixed,ps_fixed);
% ... and alignment box
R_fixed_2d_ab  = imref2d([length(Vol_fixed_ab(:,1,j)),...
                         length(Vol_fixed_ab(1,:,j))],ps_fixed,ps_fixed);
R_moving_2d_ab = imref2d([length(Vol_moving_ab(:,1,j)),...
                       length(Vol_moving_ab(1,:,j))],ps_moving,ps_moving);
R_reg_2d_ab    = imref2d([length(Vol_reg_ab(:,1,j)),...
                         length(Vol_reg_ab(1,:,j))], ps_fixed,ps_fixed);

```

```
143 % visualize "before" and "after" registration for full 3D volume
144 figure; imshowpair(Vol_moving(:,:,i),R_moving_2d,Vol_fixed(:,:,i),R_fixed_2d);
145                     title('Unregistered axial slice, full 3D volume');
146 figure; imshowpair(Vol_reg(:,:,i),R_reg_2d,Vol_fixed(:,:,i),R_fixed_2d);
147                     title('Registered axial slice, full 3D volume');
148 % ... and alignment box
149 figure; imshowpair(Vol_moving_ab(:,:,j),R_moving_2d_ab,...
150                                         Vol_fixed_ab(:,:,j),R_fixed_2d_ab);
151                     title('Unregistered axial slice, alignment box');
152 figure; imshowpair(Vol_reg_ab(:,:,j),R_reg_2d_ab,...
153                                         Vol_fixed_ab(:,:,j),R_fixed_2d_ab);
154                     title('Registered axial slice, alignment box');
155
156 %%%%%%%%%%%%%%%%%%%%%%%%%%%%%%%%%%%%%%%%%%%%%%%%%%%%%%%%%%%%%%%%%%%%%%%%%%%%
```

Acknowledgements

It has been a long journey from the first attempt to the finalized automated kV-MV CBCT imaging method, and so was the journey of my PhD thesis. Our research team had to walk down a long way on a difficult road with many barriers to pass, we suffered from setbacks, but never gave up. Thanks to the immense support and belief in this project by so many people, we finally succeeded and I was able to accomplish my measurements on the final version of kV-MV CBCT and complete my PhD thesis.

My PhD thesis would not have been completed without the tremendous support and encouragement of so many people. I wish to express my deepest gratitude to

- my thesis supervisor Prof. Dr. Frederik Wenz, for giving me the opportunity to not only be part of this great project, but to also allow me to expand my professional skills as a Medical Physics Expert in the Radiation Oncology Department, University Medical Center Mannheim, and to gain experience in coordinating courses of study at the Medical Faculty Mannheim, University of Heidelberg. Thanks for allowing me to present my work at conferences both at home and abroad.
- Prof. Dr. Frank Lohr, for his immense contribution of the kV-MV project, and especially for his tireless belief and his constant motivation to proceed with the project. His joyful anticipation to the first patient scanned with kV-MV was infectious and helped me finish my PhD thesis.
- Prof. Dr. Gerhard Glatting and Prof. Dr. Lothar Schad for the thesis examination. Besides my scientific work, it was a pleasure for me to work with them during my time as study coordinator.
- Prof. Dr. Jürgen Hesser, for the constant availability for scientific support, especially in the concept development for accurate measurement execution and guidance in statistical evaluation methods.
- Uwe Gros and Bernd Raczuhn from Elekta AB, for sharing their knowledge in linac and CBCT systems and for answering the emergency phone also after 11pm and not being mad at me for too long. Thanks for the substantial explanations, for their enormous patience when we wanted to calibrate our linac most accurate, and for the fun times in between.

- my colleagues in the kV-MV research group:
  - PD Dr. Hansjörg Wertz, for his encouragement and constant support as the project leader and my direct supervisor, for passing his knowledge about the linac and the CBCT system, the QA procedures and acceptance, in showing me how to insist on calibration in "half digits" accuracy and for a ride home when our measurements took until sunrise.
  - Dzmitry Stsepankou, without his remarkable fundamental work (reconstruction algorithm, synchronization hardware), the kV-MV project would not have been possible.
  - Dr. Manuel Blessing, for the most important support on my PhD thesis. For his outstanding guidance, the endless (night) hours we spent together fighting for a successful kV-MV measurement, for always finding chocolate in the most hidden places of the department at night, for being such a great and constant team-mate in discussion, measurement, evaluation and proof-read. Thanks for being my motivator when I had doubts, for making me not ever give up. Thanks for constantly pulling me back on track and for being such a great and patient friend.
- Dr. Jens Fleckenstein, for the fruitful discussions on Matlab programming and kV dosimetry, for proof-reading this thesis, for being a good friend and for always making me laugh with a good story.
- Dr. Flavia Molina, my office mate and precious friend, for being my anchor during all those years. Thanks for being like a sister to me.
- my physics colleagues Markus Petersheim, Stefan Kegel, Dr. Obioma Nwankwo and Dr. Ramesh Boggula, and my colleague Linda Krämer, for making work a place filled with dear friends. Thanks for the countless work- and non-work-related discussions and a lot of comfort, fun and laughter.
- my other colleagues of the physics team and especially the head of the physics group, Volker Steil, for making work a happy and valuable place. For a good and fruitful team work and for fun times especially in the lunch breaks.
- my siblings, Daniel and Sylvia, and my oldest and dearest friends from home, Linda and Theresia, for constantly being at my side, giving me power and strength. And also to Danthai Thongphiew, for joining my life for a long time, for encouraging me to finish my PhD for whatever it takes.
- and last but not least my parents, for their unconditional love and trust. For encouraging me to go my own way, for their support and patience, but not least for being my safe harbor where I can always dock if I need solid ground in my life.